



XXII Graduate Course in Physics
University of Pisa

Experimental Issues
of the Search for $\mu \rightarrow e + \gamma$ decay
in the MEG experiment
at Paul Scherrer Institut

Candidate

Dott. Giovanni Gallucci

Supervisor

Dott. Alessandro Baldini

Contents

1	Theory and Phenomenology	9
1.1	Muon decay in the Standard Model and beyond	9
1.2	The Standard Model and the leptonic flavour conservation	9
1.2.1	Muon decay in the Standard Model	11
1.2.2	Neutrino mass and mixing	12
1.2.3	Muon decay with massive neutrino	13
1.2.4	Beyond the Standard Model: SUSY-GUT theories	14
1.3	Search for the $\mu \rightarrow e + \gamma$ decay	17
1.3.1	State of research of the decay	17
1.3.2	Event signature	18
1.3.3	MEG sensitivity	20
2	The MEG experiment	23
2.1	Beam and target	23
2.2	The positron detector	27
2.2.1	COBRA magnet	28
2.2.2	Drift chambers	30
2.2.3	The Timing Counter	32
2.3	The photon detector	34
2.4	Trigger and DAQ system	37
2.4.1	The trigger system	37
2.4.2	The DAQ system	38
2.5	MEG experiment software	38
2.5.1	The MonteCarlo GEM	38
2.5.2	The data analysis structure: ROME	40

3	The Liquid Xenon Calorimeter	43
3.1	Liquid Xenon as scintillation medium	43
3.1.1	Emission mechanisms and light yield	44
3.1.2	Attenuation of scintillation light and impurities	46
3.2	Calorimeter cryogenic equipment and purification system	48
3.3	PMTs	53
3.3.1	PMTs in high background condition	54
4	The Liquid Xenon detector calibration methods	59
4.1	LXe optical proprieties and PMTs characteristics	59
4.1.1	LED and PMTs gains	59
4.1.2	α -sources	60
4.2	Calibration 4.4 MeV γ s from AmBe source	63
4.3	Calibration with Nickel 9 MeV line	65
4.4	Calibrations with Cockroft-Walton accelerator	69
4.5	Calibrations with Charge Exchange Process	71
4.5.1	Kinematics of the reaction	71
4.5.2	Liquid hydrogen target	74
4.5.3	The NaI and preshower detector	75
5	Photon Reconstruction algorithms	77
5.1	Reconstruction general remarks	77
5.2	Photomultiplier waveform analysis	79
5.3	Energy reconstruction	79
5.4	Position reconstruction	82
5.5	Time reconstruction	85
5.5.1	XECPMTWeightedAverageTime	86
5.5.2	XECTimeFit	89
5.6	Pileup rejection	90
5.7	Cosmic ray rejection	92
6	Performances of the LXe Calorimeter in 2008 MEG run	95
6.1	Calibrations of PMTs characteristics during 2008 run	95
6.1.1	Gain shift	95
6.1.2	Quantum efficiency	99

6.2	Uniformity of the calorimeter	100
6.3	The energy scale: purification and light yield	101
6.4	Energy linearity and resolution	105
6.4.1	γ from Lithium	107
6.4.2	54.9 MeV photons from π^0 decay	108
6.5	Background spectrum	110
6.6	Position resolution	111
6.7	Timing resolution	112
6.8	Photon detection efficiency	113
6.9	Conclusion	114
7	Other detector performances and efficiencies in MEG 2008 run	117
7.1	Timing Counter: positron time resolution	117
7.2	Drift chamber: positron energy and angular resolutions	118
7.3	Relative angles $\theta_{e\gamma}$ $\phi_{e\gamma}$	120
7.4	Relative time $t_{e\gamma}$	120
7.4.1	Dalitz process	120
7.4.2	Radiative decay peak	121
7.5	MEG detectors efficiencies	121
7.5.1	Positron detection efficiency	122
7.5.2	Trigger efficiency	126
8	Final analysis of 2008 MEG run	129
8.1	Data samples and selections	129
8.2	Likelihood analysis	130
8.2.1	Signal PDF	131
8.2.2	Radiative decay PDF	132
8.2.3	Accidental background PDF	133
8.3	Likelihood fit results	134
8.4	Confidence interval	134
8.5	Normalization	137
8.6	Result and 2008 sensitivity	140

9	First results from 2009 run	141
9.1	Liquid xenon purification	142
9.2	Performances of detectors	142
9.3	Preliminary result of 2009 data analysis	145
	Bibliografy	153

Introduction

The Standard Model (SM) of electroweak interactions assumes complete conservation of the lepton flavor. Even introducing corrections due to neutrinos masses, the SM predicts an unmeasurable branching ratio for this decay ($\approx 10^{-55}$). Supersymmetric grand unification models (SUSY-GUT), in which the SM is incorporated as a low energy subgroup, provide estimates of $\mu \rightarrow e\gamma$ decay just below the current experimental limit ($< 1.2 \times 10^{-11}$): searching for lepton flavor violation in this channel will therefore lead to the first observation of physics beyond the standard model, or set strong constraints on those theories.

The MEG experiment at PSI searches for the $\mu \rightarrow e\gamma$ decay with a sensitivity around 10^{-13} , thus improving the present best experimental limit of roughly two orders of magnitude. The experiment is in operation since 2007, while physics data taking started officially in 2008 and will last until 2012.

The first chapter of this thesis begins by showing a short summary of theoretical motivations supporting the search of $\mu \rightarrow e\gamma$ (principles of SM and SUSY-GUT models). After a historical introduction to the $\mu \rightarrow e\gamma$ decay searches, the event signature, backgrounds and experimental sensitivity are discussed.

In the second chapter we describe the MEG apparatus: the beam line setup, the magnetic spectrometer, the data acquisition system and the analysis software.

In the third, fourth and fifth chapters we discuss in detail the innovative liquid xenon photon detector, its calibration methods and reconstruction algorithms.

The performances of the calorimeter and the other MEG detectors during 2008 MEG run are presented in chapters 6 and 7.

Chapter 8 shows the physics analysis procedure and the final result from 2008 data.

Finally in chapter 9 a short look at preliminary 2009 MEG run results are shown.

Chapter 1

Theory and Phenomenology

1.1 Muon decay in the Standard Model and beyond

In the Standard Model of electroweak and strong interactions(SM), presently the most successful theory in explaining and predicting the elementary particle phenomenology [1], [2], lepton flavor symmetry is preserved and the rare decay $\mu \rightarrow e + \gamma$ is forbidden. If present neutrino masses, and mixing, are considered and inserted in the SM, the probability of this decay is, still, negligible.

Since several new physics models predict $\mu \rightarrow e\gamma$ to have a measurable rate, this decay plays an unique role for investigating physics beyond the Standard Model(SM). In this chapter, we will review the main SM characteristics , together with its pitfalls, and we will discuss some of its proposed extensions.

1.2 The Standard Model and the leptonic flavour conservation

The SM is a theory that describes the elementary particles of which the matter is composed and their interactions (strong, weak and electromagnetic). It is based on the gauge symmetry group $SU(3)_C \times SU(2)_L \times U(1)_Y$ of color, weak isospin and hypercharge invariance, spontaneously broken at the Fermi scale $M_F \approx 100$ GeV. The model accommodates three generations of fermion matter fields (quarks and leptons), vector bosons to mediate interactions and a scalar field (Higgs boson) to generate the particle masses. These particles and the Higgs boson are introduced as elementary fields. Both quarks and leptons are spin- $\frac{1}{2}$ particles and are grouped in three different flavor families but sensitive to different interactions. Bosons (also called Gauge bosons) have integral spin and are the interaction mediators. The leptonic group is composed

of 12 particles (electron, muon, tau, related neutrinos and related anti-particles) grouped in three flavor families (electronic, muonic and tauonic flavors). Flavor can be equal to +1, in case of particles, and to -1, in case of anti-particles. In the SM both family flavor and leptonic number are conserved. We define H , q_{ij} e l_{ij} , the fields related to Higgs boson, quarks and leptons, where $i = 1, 2, 3$ are the three flavor families and $j = R, L$ are the right-handed and left-handed chiral projections (chiral projectors are $P_R \equiv (1 + \gamma_5)/2$ and $P_L \equiv (1 - \gamma_5)/2$):

$$H = \begin{pmatrix} \phi_i \\ \phi_+ \end{pmatrix}_L \quad q_{iL} = \begin{pmatrix} u_i \\ d_i \end{pmatrix}_L \quad l_{iL} = \begin{pmatrix} \nu_i \\ e_i \end{pmatrix}_L \quad q_{iR} = \begin{pmatrix} u_i \\ d_i \end{pmatrix}_R \quad l_{iR} = \begin{pmatrix} e_i \end{pmatrix}_R \quad (1.1)$$

Then we define G_μ , A_μ e B_μ the bosonic fields related to $SU(3)_C$, $SU(2)_L$ and $U(1)_Y$ respectively, and λ_a (a=1,8 Gell-Mann matrices) and τ_a (a=1,3 Pauli matrices) $SU(3)$ and $SU(2)$ group generators. Now we can write the SM Lagrangian as sum of three different parts [40]:

$$L_{MS} = L_{Gauge} + L_{Higgs} + L_{Yukawa} \quad (1.2)$$

The first part, or gauge lagrangian, describes bosonic and fermionic free fields, their interactions and their coupling with Higgs field:

$$L_{Gauge} = \sum_{SU(3)_C, SU(2)_L, U(1)_Y} F_{\mu\nu}^a F^{a\mu\nu} + \sum_{q,l} i\bar{\psi}_{ij}\gamma^\mu D_\mu\psi_{ij} + |D_\mu H|^2 \quad (1.3)$$

where $F_{\mu\nu}^a$ is a G gauge field tensor (f_{abc} structure group constants, c coupling constant, g_s for strong interaction, g for weak interaction and g' for electromagnetic interaction, and Q_Y ipercharge):

$$F_{\mu\nu}^a = \partial_\mu G_\nu^a - \partial_\nu G_\mu^a - cf_{abc}G_\mu^b G_\nu^c \quad (1.4)$$

$$D_\mu = \partial_\mu + ig_s \frac{\lambda^a}{2} G_\mu^a + ig \frac{\tau^a}{2} A_\mu^a + ig' Q_Y B_\mu \quad (1.5)$$

The second part, the Higgs lagrangian, describes the Higgs potential:

$$L_{Higgs} = -(-\mu^2 |H|^2 + \lambda |H|^4) \quad (1.6)$$

with μ e λ parameters of theory. This part introduces a spontaneous symmetry breaking in the lagrangian: W^\pm, Z^0 and the Higgs boson become massive while photons and gluons remain massless. Masses depend on an internal theory parameter (v vacuum expectation value (VEV)):

$$m_W = \frac{gv}{2} \quad m_Z = \sqrt{g^2 + g'^2}v/2 \quad \frac{m_W}{m_Z} = \frac{g}{\sqrt{g^2 + g'^2}} \quad m_H = \sqrt{2\lambda}v \quad (1.7)$$

The last part, Yukawa's lagrangian, provide mass to fermionic particles:

$$L_{Yukawa} = -(\bar{e}_{iR}(m_e)_{ij}e_{jL} + \bar{d}_{iR}(m_d)_{ij}d_{iL} + \bar{u}_{iR}(m_u)_{ij}u_{iL}) + H.C. \quad (1.8)$$

We can write the masses as function of the Yukawa's coupling constants y_X :

$$(m_X)_{ij} = -(y_X)_{ij} \frac{v}{\sqrt{2}} \quad (1.9)$$

with $X=e,u,d$. In general the weak interaction eigenstates for quarks are different from mass ones: this generates a flavor mixing. Mixing is introduced in the SM with the following unitary mixing matrix (Cabibbo-Kobayashi-Maskawa matrix):

$$\begin{pmatrix} \acute{d} \\ \acute{s} \\ \acute{b} \end{pmatrix} = \begin{pmatrix} V_{ud}, V_{us}, V_{ub} \\ V_{cd}, V_{cs}, V_{cb} \\ V_{td}, V_{ts}, V_{tb} \end{pmatrix} \begin{pmatrix} d \\ s \\ b \end{pmatrix} \quad (1.10)$$

Since neutrinos are massless, there is not a correspondent leptonic mixing. The weak interaction lagrangian has two different forms for quarks and leptons:

$$L = -\frac{g}{\sqrt{2}}[\bar{u}_{iL}\gamma^\mu(V_{CKM})_{ij}d_{jL}W_\mu^+ + \bar{d}_{iL}\gamma^\mu(V_{CKM})_{ij}^*u_{jL}W_\mu^-] \quad (1.11)$$

$$L = -\frac{g}{\sqrt{2}}[\bar{\nu}_{iL}\gamma^\mu e_{jL}W_\mu^+ + \bar{e}_{iL}\gamma^\mu \nu_{jL}W_\mu^-] \quad (1.12)$$

This lagrangian shows that leptonic flavor is conserved and the $\mu \rightarrow e + \gamma$ decay is forbidden.

1.2.1 Muon decay in the Standard Model

The muon, like the other leptons, interacts through the mediation of the fields A_μ, W_μ^\pm and Z_0 . Introducing the coupling with the Higgs boson, it is possible to write the Lagrangian:

$$\begin{aligned} L = & e\bar{\mu}\gamma^\mu \mu A_\mu - \frac{g}{\sqrt{2}}[\bar{\nu}_{\mu L}\gamma^\mu \mu_L W_\mu^+ + \bar{\mu}_L\gamma^\mu \nu_{\mu L}W_\mu^-] - \sqrt{g^2 + g'^2} \times \\ & \times [\bar{\mu}_L\gamma^\mu \left(-\frac{1}{2} + \sin^2(\theta_W)\right)\mu_R + \bar{\mu}_R\gamma^\mu \sin^2(\theta_W)\mu_L]Z_\mu^0 - \frac{m_\mu}{v}\bar{\mu}\mu H \end{aligned} \quad (1.13)$$

where θ_W is the Weinberg angle, e is the electron charge and they are related to theory constants by:

$$\sin \theta_W = \frac{g'}{\sqrt{g^2 + g'^2}} \quad e = g \sin \theta_W \quad (1.14)$$

The muon is not a stable particle and decays with a lifetime $\tau = 2.19703 \pm 0.00004 \mu\text{sec}$ [3]. The decay is associated with the second term of 1.13, vertex in which the muon is associated

with a muon neutrino and a virtual W. The Lagrangian for the decay of the muon or the Fermi Lagrangian is:

$$L_{Fermi} = -\frac{G_F}{\sqrt{2}}[\bar{\mu}\gamma^\mu(1-\gamma^5)\nu_\mu\bar{e}\gamma^\mu(1-\gamma^5)\nu_e + \bar{\nu}_e\gamma^\mu(1-\gamma^5)e\bar{\mu}\gamma^\mu(1-\gamma^5)\nu_\mu] \quad (1.15)$$

where G_F is the Fermi couplig, connected to the weak interaction constant by the following relation:

$$G_F = \frac{g^2}{4\sqrt{2}m_W^2}. \quad (1.16)$$

with m_W , mass of W boson There are a second $[\mu^\pm \rightarrow e^\pm + \nu_e(\bar{\nu}_e) + \bar{\nu}_\mu(\nu_\mu) + \gamma]$ and a third $[\mu^\pm \rightarrow e^\pm + \nu_e(\bar{\nu}_e) + \bar{\nu}_\mu(\nu_\mu) + e_+ + e_-]$ channel decay with much lower probability , $1.4 \pm 0.4\%$ for γ -energy ≤ 10 MeV [4] and $3.4 \pm 0.4 \times 10^{-5}\%$ [5] , respectively.

1.2.2 Neutrino mass and mixing

In the SM, lepton flavor conservation is accidentally due to neutrinos having zero masses. There are strong experimental evidences that the atmospheric neutrino anomaly and the solar neutrino deficit are due to the phenomenon of neutrino oscillation, which requires massive neutrinos ([6], [7], [8], [9], [10], [11], [12], [13], [14], [15], [16], [17]). Indeed, assuming for simplicity only two neutrino flavors (ν_e, ν_μ), we can write them as linear composition of the mass eigenstates (ν_1, ν_2):

$$\begin{pmatrix} \nu_e \\ \nu_\mu \end{pmatrix} = \begin{pmatrix} \cos\theta & \sin\theta \\ -\sin\theta & \cos\theta \end{pmatrix} \quad (1.17)$$

If a ν_e is produced, it evolves according to the mass eigenstates and the probability to observe a ν_μ becomes an oscillating function of the initial energy and distance from the source:

$$P(\nu_e \rightarrow \nu_\mu) = \sin^2 2\theta \sin^2 \left(1.27 \frac{\Delta m^2 (eV^2) L(m)}{E(MeV)} \right) \quad (1.18)$$

with θ mixing angle, and Δm^2 the square mass difference. This phenomena is called "neutrino oscillation". Neutrino oscillations experiments are sensitive only to mass differences: some experimental upper limits for neutrino masses are available, $2 \text{ eV}/c^2$ for ν_e , $190 \text{ KeV}/c^2$ for ν_μ and $18.2 \text{ MeV}/c^2$ for ν_τ ([18], [19], [20], [21]). These masses are very small to compared to those of the charged leptons. Theoretically it is possible to give rise to neutrino mass terms inserting in the Lagrangian the field for the right-handed neutrino, ν_R . We can introduce in the Lagrangian the Yukawa coupling of the right-handed neutrino:

$$L_Y^\nu = \bar{L}_L^i \lambda_n^{ij} \phi^\dagger \nu_R \quad (1.19)$$

which becomes, after spontaneous symmetry breaking, the following mass term for neutrino:

$$L_Y^m = v \bar{\nu}_L^i \lambda_n^{ij} \phi^\dagger \nu_R \quad (1.20)$$

Diagonalizing it we obtain the neutrino mass eigenstates. The introduction of right-handed neutrinos makes the oscillation phenomena possible but does not explain the lightness of its masses. One of possible hypotheses is the see-saw model [28]. Neutrino is electrically neutral so there is the possibility that it is its own anti-particle (Majorana's particle): neutrinos and antineutrinos are just opposite chiral states of the same particle. In this case we can write in the Lagrangian additional mass terms of the form

$$m_L \nu_L \nu_L^c + M_R \nu_R \nu_R^c \quad (1.21)$$

The right handed neutrinos are completely neutral under SM gauge group: they can acquire Majorana masses M_R which are unrelated to the electro-weak symmetry breaking. Assuming for simplicity only one neutrino generation, the complete mass term becomes:

$$m_D \bar{\nu}_L \nu_R + M_R \bar{\nu}_R^c \nu_R + h.c. = (\bar{\nu}_L \quad \bar{\nu}_R^c) \begin{pmatrix} 0 & m_D \\ m_D & M_R \end{pmatrix} \begin{pmatrix} \nu_L \\ \nu_R \end{pmatrix} \quad (1.22)$$

with m_D neutrino Dirac mass naturally comparable with the other lepton masses. If $M_R \gg M_Z$ the eigenvalues of the matrix (neutrino physical masses) are

$$m_1 \approx M_R \quad \text{and} \quad m_2 \approx \frac{m_D^2}{M_R} \quad (1.23)$$

For example, if M_R is 10^{15} GeV and $m_D \approx 100$ GeV, the neutrino mass becomes $O(10^{-2})$ eV.

1.2.3 Muon decay with massive neutrino

Inserting in the SM Lagrangian massive neutrinos, the decay $\mu \rightarrow e + \gamma$ becomes possible. Figure 1.1 shows the relevant Feymann diagrams. Assuming that only ν_e and ν_μ are mixed, we can write the decay rate:

$$\Gamma(\mu^+ \rightarrow e^+ \gamma) = \frac{G_F^2 m_\mu^5}{192 \pi^3} \frac{\alpha}{2\pi} \left(\frac{m_1^2 - m_2^2}{M_W^2} \right)^2 \sin^2(2\theta) \quad (1.24)$$

Normalizing to the standard muon decay and replacing $\Delta m^2 \sin 2\theta$ with the measured values from KamLAND [16] ($\Delta m^2 = 6.9 \times 10^{-5}$ e $\sin 2\theta = 0.91$ al 95% di C.L.), we obtain $\text{BR} \approx 10^{-55}$, not presently measurable.

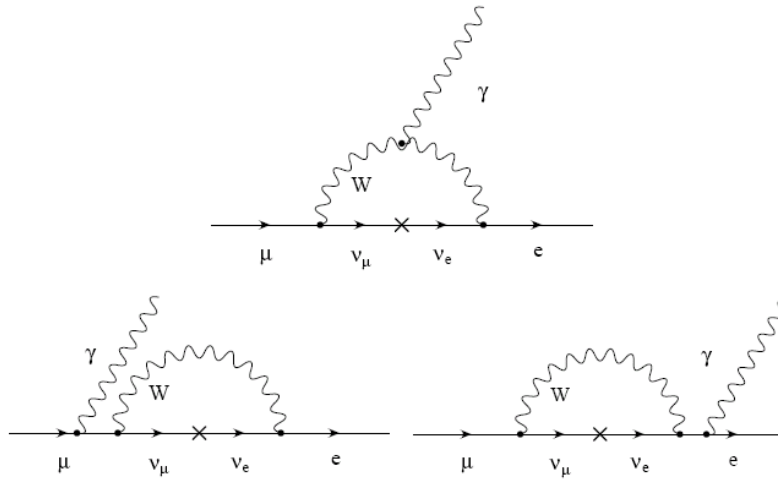


Figure 1.1: $\mu \rightarrow e + \gamma$ decay diagram with neutrino oscillations.

1.2.4 Beyond the Standard Model: SUSY-GUT theories

Supersymmetric grand unified theories arise from the introduction of the mechanisms of supersymmetry (SUSY) within the grand unified theories or GUTs.

- GUT theories [23] assume that the SM is a subset of a larger gauge theory used to describe physics at higher energies, in particular, suggest a unification of electroweak and strong forces at energies above M_G ($\approx 10^{15}$ GeV). Since quarks and leptons appear together in irreducible representations of the symmetry group adopted, conservation laws of baryon number, lepton number and flavor are not valid anymore. Moreover, because of the existence of a flavor violation in transition among quarks of different generations, a similar violation must be present for leptons. Below the unification scale, interactions are separated and particles acquire different properties. These theories can overcome SM theoretical problems related to electric charge quantization and the relationship between lepton and quark charges; further, all of SM coupling constants are related to a single parameter called g_G . GUT theories involve the $\mu \rightarrow e\gamma$ decay but the process is suppressed by a factor $\frac{1}{M_G}$ being experimentally not measurable.
- The supersymmetry mechanisms [23] introduce, in a particular model, new symmetries to cancel the divergences in the computation of Higgs boson mass. They hypothesize new-

particles (super-particles or sparticles) with same internal quantum numbers and masses equal to those of the normal particles (in condition of non broken supersimmetry), but differ for $\frac{1}{2}$ in spin value. Table 1.1 shows how each boson is associated in supersymmetry

Particles MS	Spin	Particles SUSY	Spin
quarks(q)	1/2	squarks(sq)	0
leptons(l)	1/2	sleptons(sl)	0
gluons(G)	1	gluino	1/2
W^\pm, Z^0, γ	1	chargino $\tilde{\chi}_i^\pm (i = 1 - 2)$	1/2
bosone di Higgs H	0	neutralino $\tilde{\chi}_i^0 (i = 1 - 4)$	1/2

Table 1.1: SUSY particles related to MS ones (in Standard Model Minimal Supersymmetric extension (MSSM)).

with a fermionic sparticle and vice versa. In the computation of Higgs mass divergences related to fermionic loops disappear since each fermionic loop has an associated loop with its corresponding sparticles. Being a boson, the loop has opposite sign to the fermionic one, thus canceling the divergence (fig.1.2).

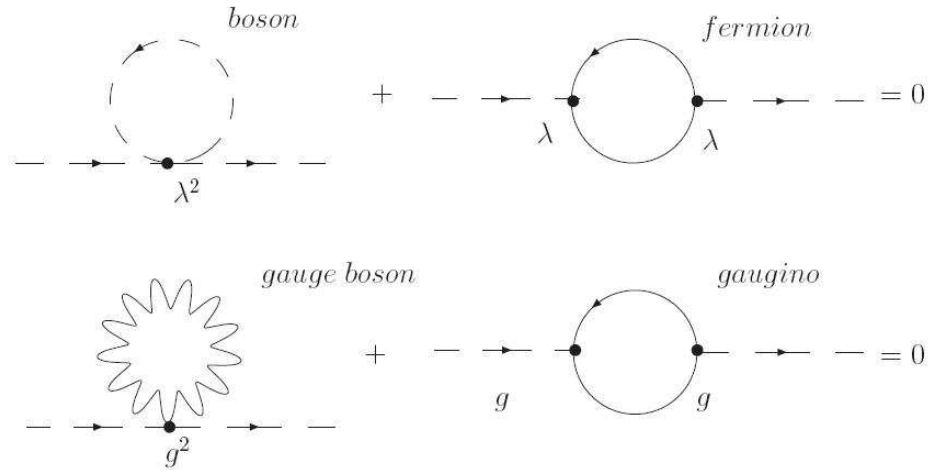


Figure 1.2: Cancellation of quadratic terms (divergencies).

SUSY-GUT theories involve unification of electromagnetic, weak and strong interactions. They have lepton flavor violation mechanisms similar to GUT models, but the interaction can be mediated by sparticles with masses of about 100 GeV (fig.1.2.4). This gives values for $\mu \rightarrow e + \gamma$ decay BR that can be as high as $10^{-12} - 10^{-16}$. Figure 1.4 for SU(5) [25]

and figure 1.5 for SO(10) [26] show the expected values for $\text{BR}\mu \rightarrow e + \gamma$) as a function of right-handed selectron mass. The expected BRs for SU(5) and SO(10) are far from the current limit (MEGA [27]) but can be tested (entirely for SO(10), partially for SU(5)) by the MEG experiment which aims to reach a $\text{BR} \approx 10^{-13}$.

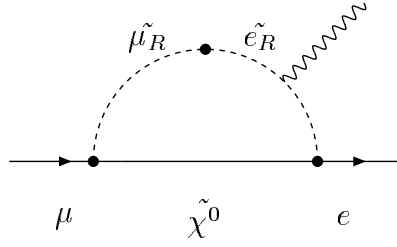


Figure 1.3: Feynmann diagram for $\mu \rightarrow e\gamma$ decay in $SU(5)$ $SUSY - GUT$ theory.

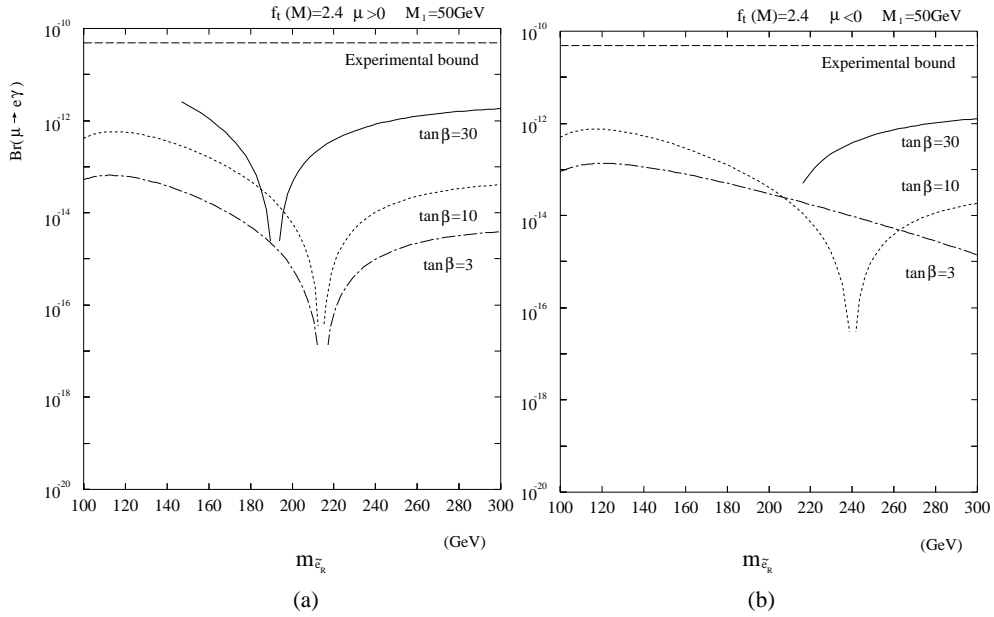


Figure 1.4: Expected BRs of $\mu \rightarrow e\gamma$ decay for $SU(5)$ $SUSY - GUT$ as a function of right-handed selectron mass for different values of $\tan \beta$.

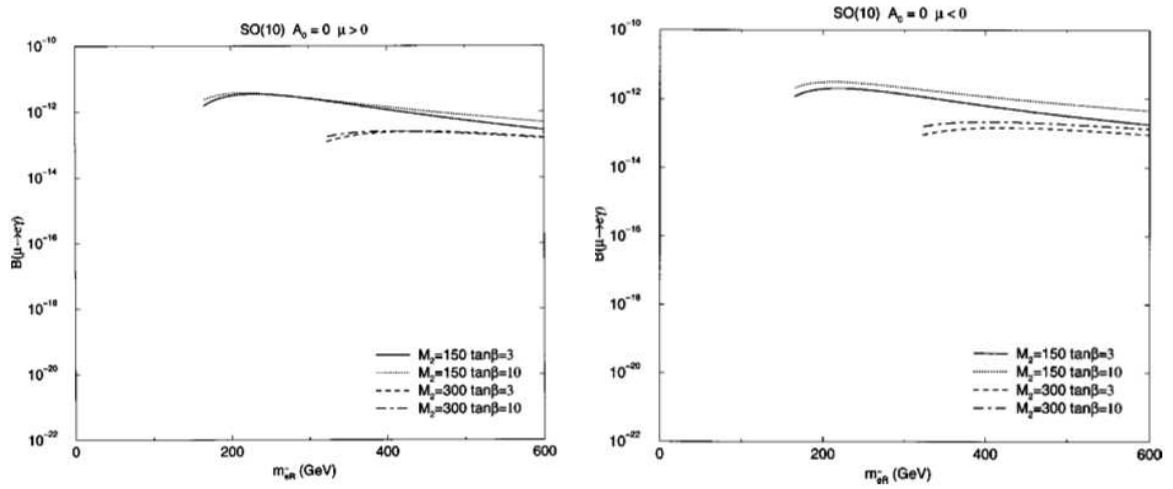


Figure 1.5: Expected BR of $\mu \rightarrow e\gamma$ decay for $SO(10)$ $SUSY - GUT$ as a function of right-handed selectron mass for different values of $\tan\beta$.

1.3 Search for the $\mu \rightarrow e + \gamma$ decay

1.3.1 State of research of the decay

The search for the $\mu \rightarrow e + \gamma$ decay began in 1947 with an experiment made by Hincks and Pontecorvo [30], that put a limit on the BR < 0.1 , using cosmic ray muons. With the advent of particle accelerators, and thus more intense muon sources, the experiments continued: in 1955 an experiment at Columbia University Nevis cyclotron put the limit at $BR = 2 * 10^{-5}$ [31]. In 1958, Feinberg [32] predicted the decay with a rate of 10^{-4} , but given the lack of experimental evidence, then emerged the hypothesis that the process was forbidden because of lepton flavor conservation. The existence of two different types of neutrino: ν_e and ν_μ was hypothesized by Pontecorvo [33] and it was confirmed by an accelerator experiment at Brookhaven National Laboratory in 1962 [34]. Currently the most accurate measurement of BR is the one of the MEGA collaboration: $BR < 1.2 * 10^{-11}$. MEG aims to lower this limit by two orders of magnitude reaching a sensitivity of $\approx 10^{-13}$. Table 1.2 shows the most recent experiments, the resolutions obtained in the e^+ and γ kinematical variables and the final limit obtained.

Experiment	Year	ΔE_e	ΔE_γ	$\Delta t_{e\gamma}$	$\Delta\theta_{e\gamma}$	Upper Limit	Reference
TRIUMF	1977	10%	8.7%	6.7 ns	-	$< 3.6 \times 10^{-9}$	[36]
SIN	1980	8.7%	9.3 %	1.4 ns	-	$< 1.0 \times 10^{-9}$	[37]
LANL	1982	8.8%	8%	1.8 ns	37 mrad	$< 1.7 \times 10^{-10}$	[38]
CrystalBox	1986	8%	8%	1.8 ns	87 mrad	$< 4.9 \times 10^{-11}$	[39]
MEGA	1999	1.2%	4.5%	1.6 ns	15 mrad	$< 1.2 \times 10^{-11}$	[35]

Table 1.2: Experiments to search for the decay $\mu e\gamma$ in the last 30 years : resolutions and results.

1.3.2 Event signature

The signature of a $\mu \rightarrow e + \gamma$ decay at rest is the simultaneous emission of the two daughter particles, having opposite directions and energy equal to one half of the muon mass $E_\gamma = E_e = m_\mu/2 = 52.8$ MeV. Backgrounds are of two different kinds:

- Physical: namely muon radiative decay.
- Accidental: from the accidental coincidence between a positron from the standard muon decay and a high energy photon from all other possible sources (radiative decay, annihilation in flight, or bremsstrahlung) within the experimental resolutions.

Physical background

The physical background in the decay $\mu \rightarrow e + \gamma$ is given by the radiative decay of the muon: $\mu^+ \rightarrow e^+ \nu_e \bar{\nu}_\mu \gamma$. This decay can be confused with a signal event when the positron and photon are emitted along the same line of flight and the two neutrinos have low energy. One can calculate the differential decay width as a function of the following variables $x = \frac{2E_e}{m_\mu}$, $y = \frac{2E_\gamma}{m_\mu}$, $z = \pi - \theta_{e\gamma}$. The interesting case is when the energy of the positron and the photon is very close to one half of the muon mass. We can expand the expression of the decay width in the region $x \approx 1$, $y \approx 1$, $z \approx 0$ [40]. Figure 1.6 shows the fraction of $\mu \rightarrow e\nu\nu\gamma$ decays mistaken as $\mu \rightarrow e\gamma$ the branching as a function of Δx e Δy , under the assumption of $\Delta z \leq 2\sqrt{\Delta x \Delta y}$ with Δx , Δy e Δz the experimental resolutions (FWHM) of the respective variables. As you can see from the figure, to obtain a physical background of the order of 10^{-15} , Δx and Δy must be ≈ 0.01 . The MEG collaboration aims at the following resolutions (FWHM):

$$\Delta E_e = 0.7 \div 0.9\% \quad \Delta E_\gamma = 4\% \quad \Delta\theta_{e\gamma} = 17 \div 20.5 \text{ mrad} \quad \Delta t_{e\gamma} = 0.15 \text{ ns} \quad (1.25)$$

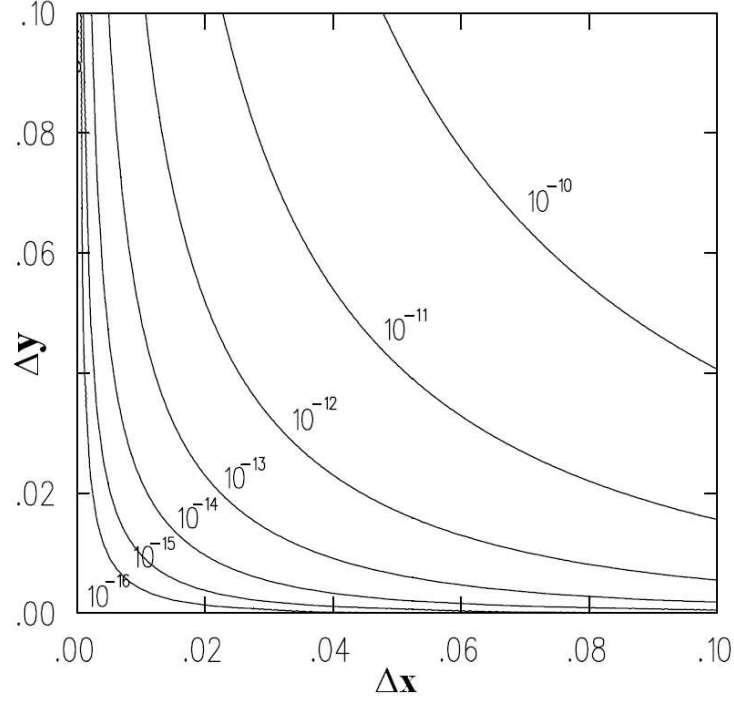


Figure 1.6: Fraction of $\mu \rightarrow e\nu\nu\gamma$ decays mistaken as $\mu \rightarrow e\gamma$ as a function of positron and photon energy resolutions ($x = \frac{2E_e}{m_\mu}$, $y = \frac{2E_\gamma}{m_\mu}$).

It is possible to verify that, with MEG expected resolutions, the condition $\Delta z \leq 2\sqrt{\Delta x \Delta y}$ is verified.

Accidental background

Reaching of the greatest possible sensitivity in a reasonable amount of time requires an intense muon beam. In the MEG experiment, the accidental background is more important than the physical one. The effective accidental branching ratio can be defined as:

$$BR_{acc} = N_{acc} \times N_\mu \quad (1.26)$$

with N_{acc} and N_μ number of accidentals and total muons, respectively. We can compute:

$$N_{acc} = R_\mu^2 f_e f_\gamma \Delta t_{e\gamma} \left(\frac{\Delta\theta_{e\gamma}}{4\pi} \right)^2 T \quad \text{and} \quad N_\mu = R_\mu T \quad (1.27)$$

$$\Rightarrow BR_{acc} = R_\mu f_e f_\gamma \Delta t_{e\gamma} \left(\frac{\Delta\theta_{e\gamma}}{4\pi} \right)^2 \quad (1.28)$$

where f_e e f_γ are the integrated fractions of positron and photon spectra in the intervals $\left[m_\mu/2 - \Delta E_{e/\gamma} ; m_\mu/2 \right]$, $\Delta E_{e/\gamma}$ being the positron and photon energy resolutions; $\Delta\theta_{e\gamma}$ and $\Delta t_{e\gamma}$ the angular and time resolutions; T total time. We can estimate f_e and f_γ reconsidering the x and y variables of previous paragraph. The integration range for the spectrum of Michel decay positrons, expressed in (x, y) variables, is $1 - \Delta x \leq x \leq 1$. The integration range for the photon spectrum is $1 - \Delta y \leq y \leq 1$. Considering only radiative decay γ , it turns out that $f_e \propto 2\Delta x$ and $f_\gamma \propto (\Delta y)^2$.

$$\Rightarrow BR_{acc} = R_\mu (2\Delta x) \left(\frac{\alpha}{2\pi} (\Delta y)^2 [\ln(\Delta y) + 7.33] \right) \left(\frac{\Delta\theta_{e\gamma}^2}{4} \right) (2\Delta t_{e\gamma}) \quad (1.29)$$

Substituting in the expression the following values $R_\mu \approx 3 \times 10^7 \text{ s}^{-1}$, $\Delta x \approx 1\%$, $\Delta y \approx 6\%$, $\Delta\theta_{e\gamma} \approx 3 \times 10^{-4} \text{ sr}$ e $\Delta t_{e\gamma} \approx 1 \text{ ns}$, the accidental branching ratio and rate are $BR_{acc} \approx 3 \times 10^{-13}$ and $R_{acc} \approx 9 \times 10^{-5} \text{ s}^{-1}$. Note the quadratic dependence of the accidental background from the energy resolution of the photon. For this reason an innovative calorimeter has been developed for the MEG experiment.

1.3.3 MEG sensitivity

The number of events measured by the experiment (N_e) depends on the following variables: R_μ beam intensity, T total live time of experiment, Ω solid angle covered by the apparatus, ϵ_e detection efficiency of 52.8 MeV positrons, ϵ_γ of 52.8 MeV photons, ϵ_{sel} selection efficiency of signal events and $(B(\mu \rightarrow e\gamma))$ the branching ratio of searched decay:

$$N_e = R_\mu T \frac{\Omega}{4\pi} \epsilon_e \epsilon_\gamma \epsilon_{sel} B(\mu \rightarrow e\gamma) \quad (1.30)$$

We define the sensitivity to single event or SES, the value of $B(\mu \rightarrow e\gamma)$ for which the number of events expected is equal to 1:

$$SES = \frac{1}{R_\mu T (\Omega/4\pi)} \times \frac{1}{\epsilon_e \epsilon_\gamma \epsilon_{sel}} \quad (1.31)$$

Substituting for ϵ_e and ϵ_γ estimated values for the experiment:

$$R_\mu = 3 \times 10^7 \quad T = 2.6 \times 10^7 \quad \Omega/4\pi = 0.09 \quad \epsilon_e = 0.45 \quad \epsilon_\gamma = 0.60 \quad \epsilon_{sel} = 0.7 \quad (1.32)$$

we obtain a SES of 3.8×10^{-14} . If signal is not observed, it is simple to roughly convert the SES into an upper limit at 90% of confidence level (CL) as following. The signal event distribution is a poissonian:

$$P(N_e|\mu) = \frac{e^{-\mu} \mu^{N_e}}{N_e!} \quad (1.33)$$

with μ equal to the number of expected events, N_e number of observed events. In our case N_e is equal to 0. For a CL equal to 90%, we thus have:

$$B(\mu \rightarrow e\gamma) < \left(\ln \frac{1}{1-\alpha}\right) \left(\frac{1}{R_\mu T \frac{\Omega}{4\pi} \epsilon_e \epsilon_\gamma \epsilon_{sel}}\right) \quad (1.34)$$

with α equal to 0.1. Substituting the experiment values, we obtain:

$$B(\mu \rightarrow e\gamma) \approx 2.0 \times 10^{-13} \quad @ \ 90\% \ CL \quad (1.35)$$

Chapter 2

The MEG experiment

As already stated in section 1.3.2 the $\mu \rightarrow e + \gamma$ signature, for a muon at rest, is a photon and a positron emitted in coincidence in time, collinear, both with energy equal to about 52.8 MeV (one half of the muon mass). In order to distinguish these events from background it is necessary to measure the energy, the time and direction of the two particles, with a very good resolution. All the photon quantities are measured by a new type of liquid Xe calorimeter, while for positron by the superconducting COBRA (COstant Bendig RAdius), a set of sixteen drift chambers and some scintillation counters. The experiment is at the Paul Scherrer Institute (PSI) at Villigen in Switzerland, where the most intense muon beam in the world is present. In figure 2.1 a scheme of the experiment is shown.

In the chapter we will use as a reference system, a system of axes with origin in the MEG target and the two angles θ and ϕ , as shown in figure 2.2.

2.1 Beam and target

The PSI accelerator provides a continuous beam of protons of energy equal to 590 $\frac{MeV}{c}$ and intensity equal to $\approx 2 mA$. The main properties of the proton beam are listed in table 2.1. This beam hits two different graphite targets, a thinner one called M-target and a thicker called E-target, before being stopped in a high power beam dump or refocused on the target of a high-flux spallation neutron source (SINQ). From these two targets, seven secondary pion and muon beam-lines are produced. The $\pi E5$ channel, dedicated to MEG, extracts low energy pions and muons from E-target at an angle of 175° with respect to the primary proton beam. The main characteristics of $\pi E5$ beam are listed in table 2.2. The momentum of muons produced by

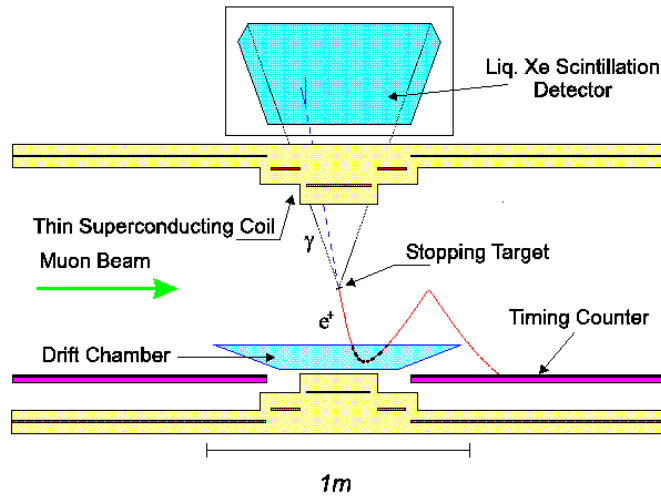


Figure 2.1: A 2D scheme of experiment MEG apparatus.

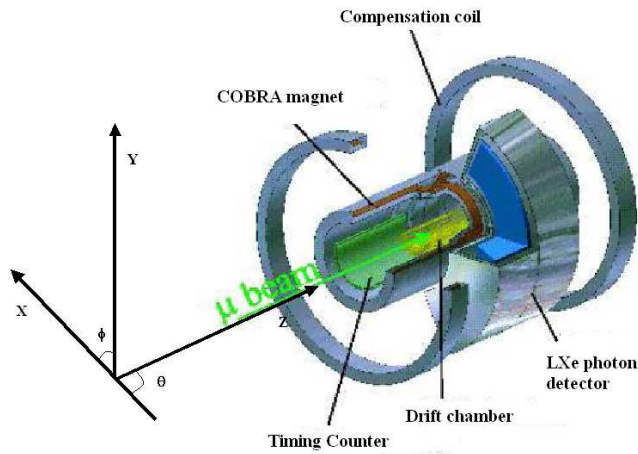


Figure 2.2: Coordinate system.

the decay $\pi^+ \rightarrow \mu^+ + \nu_\mu$, with the pion at rest, is $29 \frac{MeV}{c}$. Since the range of these muons in graphite is $\approx 1mm$, those that manage to escape from the target are produced near the surface, and are named "surface muons"[42]. They have well determined momentum and are completely polarized. In fig. 2.3 the different particle fluxes measured in the $\pi E5$ line are shown as a function of the momentum. The peak around $29 \frac{MeV}{c}$ is related to surface muons. Positrons have an intensity about a factor of ten higher than muons and may interfere with the proper operation of the experiment.

Injection energy	72 MeV
Extraction energy	590 MeV
Extraction momentum	1.2 GeV/c
Relative energy spread (FWHM)	$\approx 0.2\%$
Beam emittance	$\approx 2 \text{ mm} \times \pi \text{ mrad}$
Beam current	1.8 mA DC
Accelerator frequency	50.63 MHz
Time between pulses	19.75 ns
Bunch width	$\approx 0.3 \text{ ns}$

Table 2.1: Main proton beam characteristics.

Beamline length	10.4 m
Pulse energy range	20-120 MeV/c
Pulse resolution	2%
Solid angle	150 msr
Beam section(FWHM)	$40 \times 40 \text{ mm}^2$
Horizontal emittance	15.3 cm-rad
Vertical emittance	3.6 cm-rad

Table 2.2: $\pi E5$ beamline characteristics

In the experimental hall, the beam is focused by a triplet of quadrupoles, passes through an electrostatic separator (Wien filter) which spatially separates muons from positrons and then it is refocused through a second quadrupole triplet. Finally, a transport solenoid (BTS) serves as a junction between the last quadrupole and the MEG magnet (fig.2.4). In fig.2.5 the positron and muon separation, after the separator, is shown. The intensity of the beam was measured in the final configuration and is equal to approximately $\approx 3 \times 10^7 \mu^+ / \text{sec}$. The section of the beam is roughly circular with a σ of 10 mm. To be able to observe the decays at rest, muons must be stopped in a target. Among the various materials considered for performing this task, a target of 175 μm of polyethylene (CH₂) was chosen to minimize multiple scattering and positron Bremsstrahlung in the target. However, since the range of a 29 $\frac{\text{MeV}}{c}$ -pulse muon is about 1.1 mm in polyethylene, in order to optimize the stopping rate two caveats were taken :

- A muon pulse degrader of about 300 μm of Mylar is inserted inside the transport solenoid

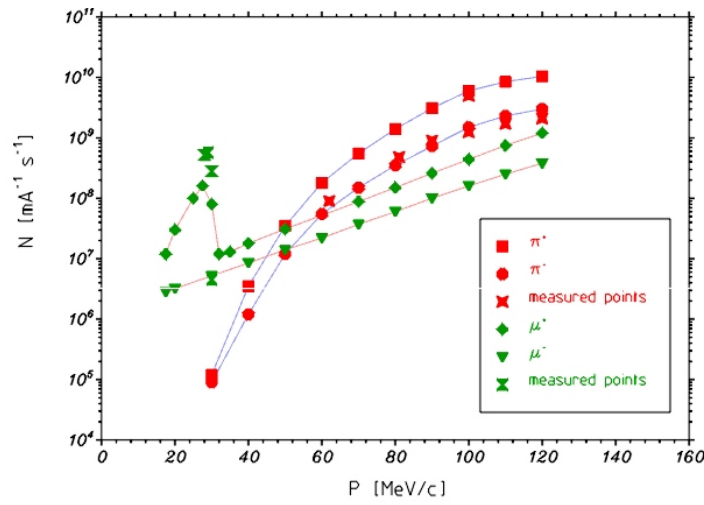


Figure 2.3: Muons and pions in $\pi E5$ beam as an energy function

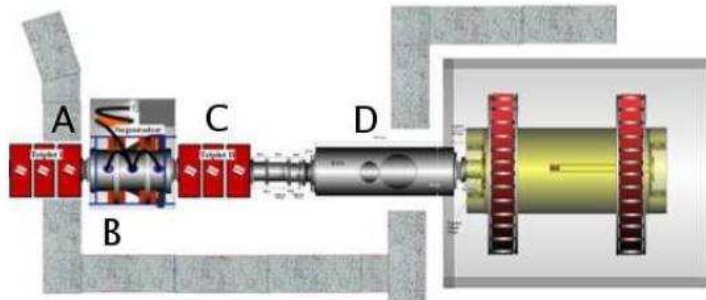


Figure 2.4: Scheme of beamline: A and C are triplets of quadrupoles, B is the Wien filter and D is the BTS.

- The target has an angle of 20.5° relative to the muon beam direction. This angle maximizes the CH_2 thickness crossed by the beam and minimizes the outgoing multiple scattering.

The target is immersed in an atmosphere of He in order to minimize the positron multiple scattering and can be displaced to prepare calibrations of calorimeter as described in the next chapters.

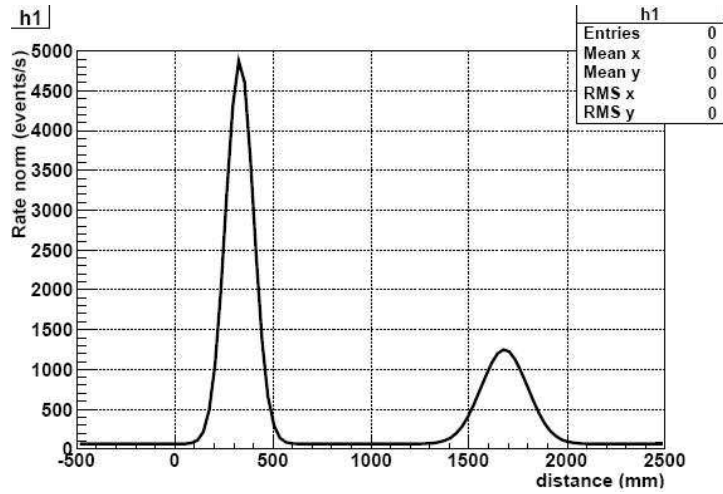


Figure 2.5: Positrons(left) and muons(right) separation after a Wien filter

2.2 The positron detector

Positron momentum and direction are determined by a tracking system consisting of the superconducting magnet COBRA and a drift chamber system, while the time of flight is measured by a scintillation counter system called "timing counter" (TC) (fig.2.6). Before describing the

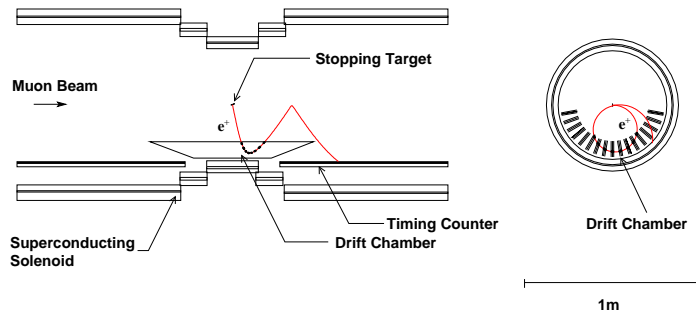


Figure 2.6: Positron detector scheme.

various devices individually, we analyze some features of the experiment:

- There is an intense background of low momentum positrons produced by the muon standard decay $\mu^+ \rightarrow e^+ + \nu_e + \bar{\nu}_\mu$ (Michel positrons) that can crowd the drift chambers and affect their operation.

- With uniform magnetic field, positrons emitted with an angle of 90° relative to the direction of the field, spend a considerable amount of time within the drift chambers causing problems to track reconstruction and instability in the operation of drift chambers themselves (fig.2.7).

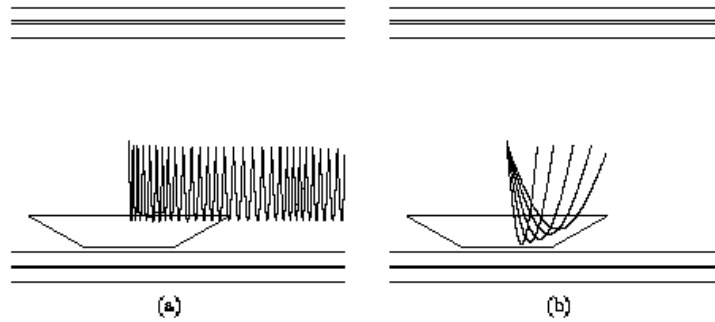


Figure 2.7: Uniform magnetic field problems : (a) positrons emitted to 88° pass through the chambers several times; (b) the radius of curvature of particles with the same pulse emitted at different angles depends on the angle.

It was therefore decided to:

- Use a degressive and non homogeneous magnetic field.
- Place the drift chambers at some distance from the target.

The non homogeneous magnetic field allows rapid extraction of the positrons emitted at angles close to 90° and makes the radius of curvature dependent only on the momentum and not on its transverse component; this feature is useful for the event analysis and could be used, in principle, for the selection of events (fig.2.8). Low momentum positrons are confined in a cylinder with a small radius and do not reach the drift chambers.

2.2.1 COBRA magnet

The non homogeneous field of MEG is obtained through the use of five superconducting coils of three different radii. In fig.2.9 the magnetic field profile is shown. Two additional resistive coils in Helmholtz configuration are placed outside to reduce the magnetic field in the region of the calorimeter because photomultiplier tubes are very sensitive to both the intensity of the magnetic field and its direction. Indicating the maximum intensity applicable to a PMT as the one that reduces its output by a factor of 2, in the fig.2.10 it is clear the allowed values are

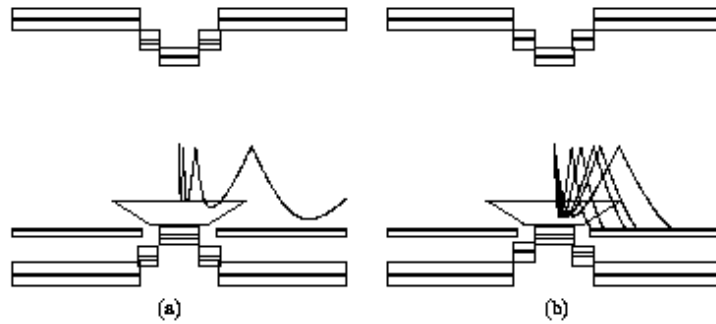


Figure 2.8: The non homogeneous magnetic field: (a) positrons emitted to 88° are quickly extracted from chambers; (b) the radius of curvature of particles with the same pulse emitted at different angles don't depend on the emission angle.

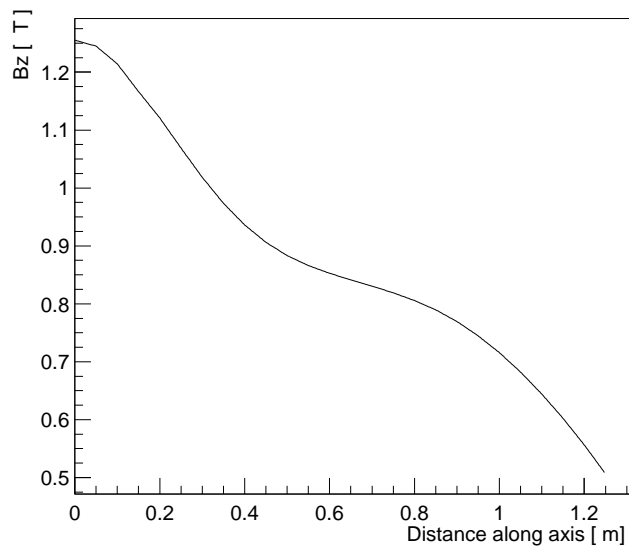


Figure 2.9: Field intensity along z as function of target center.

50 gauss in the direction perpendicular to the axis of the PMT and 150 gauss in the parallel direction. In fig.2.11 the intensity of the magnetic field near the calorimeter is shown.

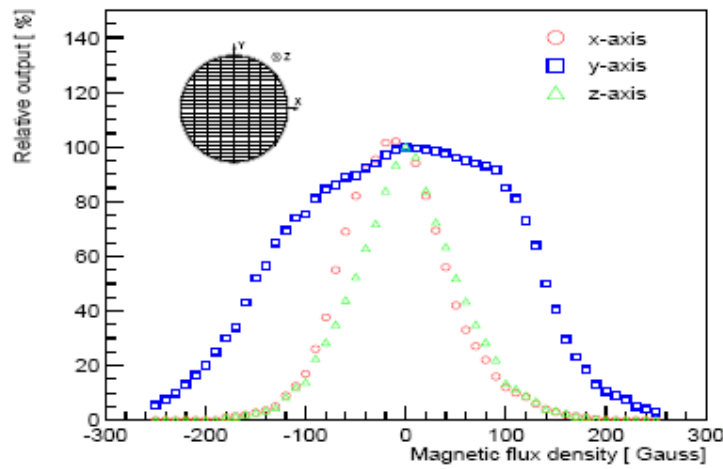


Figure 2.10: PMTs signal as function of magnetic field.

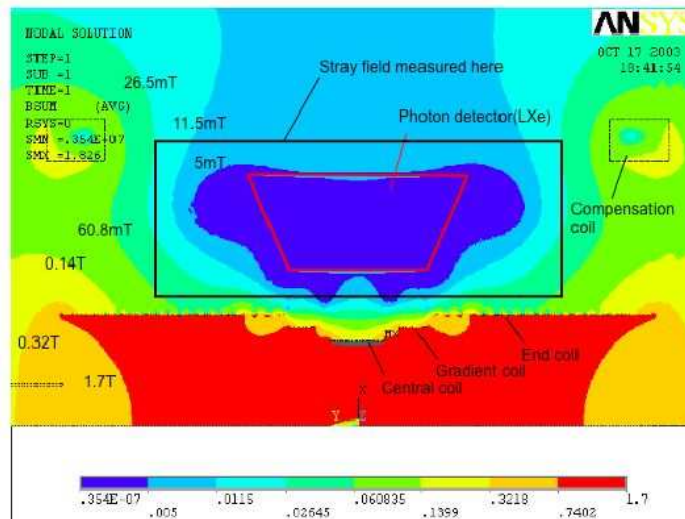


Figure 2.11: Magnetic field map in experimental area. The x-values are expressed in Tesla.

2.2.2 Drift chambers

Positron trajectories are determined by means of 16 drift chamber sectors radially aligned at 10.5° intervals in azimuth (see fig.2.13). Each sector is made up of two staggered trapezoidal arrays of drift cells to resolve the left-right ambiguity (fig.2.12). The sensitive area of the chamber extends from a radius of 19.3 cm to a radius of 27.0 cm. The active region extends

up to $z = \pm 50$ cm at the inner radius and $z = \pm 21.9$ cm at the outer radius. For 29 MeV/c positrons emitted from the target the coverage is equal to $|\cos \theta| < 0.35$ and $|\phi| < 60^\circ$. The

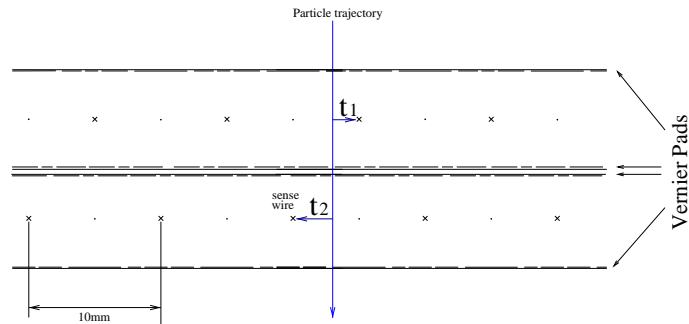


Figure 2.12: Scheme of a drift chamber sector.

angle and momentum resolution are primarily limited by the multiple scattering of particles in the chamber structure and gas. For this reason, particular attention was paid to materials used in the construction of the chambers: the wall, working as a cathode, is made of an $12.5 \mu\text{m}$ thick polyamide foil, with a 250 nm aluminum coating. An array of sense (anode) and potential wires, fixed to a carbon fiber frame, is mounted inside the chambers. The carbon frame has only three sides and it is open towards the target. This open-frame makes wire and foil stretching more challenging, but keeps the amount of material to a minimum; the overall material crossed by the typical trajectory of a 52.8 MeV/c positron corresponds to $0.002 X_0$.

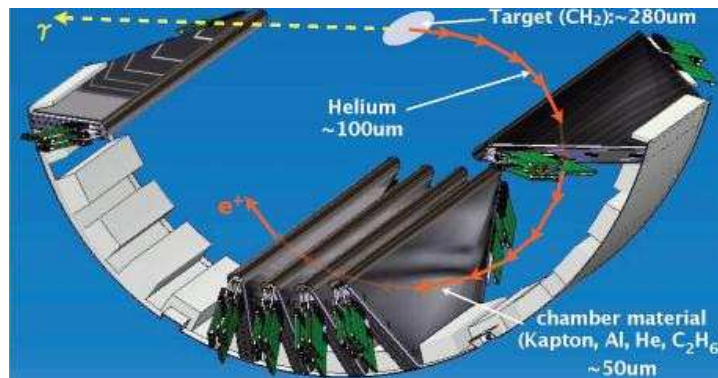


Figure 2.13: Drift chamber configuration.

The cell configuration allows the simultaneous measurement of the r -coordinate and of the absolute time of a chamber-sector positron crossing. The difference between the drift times $t_1 - t_2$ in two adjacent cells gives the r -coordinate of the track with $100 - 200\mu m$ accuracy, while the mean time $\frac{(t_1+t_2)}{2}$ gives the absolute time of the sector crossing with $\approx 5ns$ accuracy. By measuring the difference in charge collection at the two ends of the wire, it is possible to measure the z with a resolution of 1 cm. In order to improve it, which is essential for a good reconstruction of tracks, the thin layer of aluminum deposit on the four cathode foils is patterned to make a 5 cm period Zig-Zag-strip, called Vernier pattern as shown in fig.2.14. This allows to reach resolutions of the order of $300 - 500\mu m$. The chambers, and the volume in which they are immersed, are filled with a mixture of He and C_2H_6 in equal parts.

2.2.3 The Timing Counter

The Timing Counter (TC) was designed to measure the positron timing with a resolution of 100 ps (FWHM) (fig.2.15), essential for achieving the desired sensitivity. It also provides a fast measure of the positron impact point (z resolution of about 1 cm, ϕ of about 3 cm) usable in the trigger system. It is composed of two half cylinders hodoscopes, coaxial with COBRA and placed on both side of the positron spectrometer. Each hodoscope is made of 15 square-section bars of plastic scintillator (80 cm long and 4 cm in thick) and 256 BC404 Bicron scintillating fibers with square cross-section (5 mm x 5mm) perpendicular to the bars (fig.2.16). At both ends of each bar there is one phototube that collect the signals. These phototubes have been chosen to operate in the MEG magnetic field and are inclined at 20 degrees with respect to z to minimize the effect of the field (fig.2.17). The signals of each scintillating fiber is collected

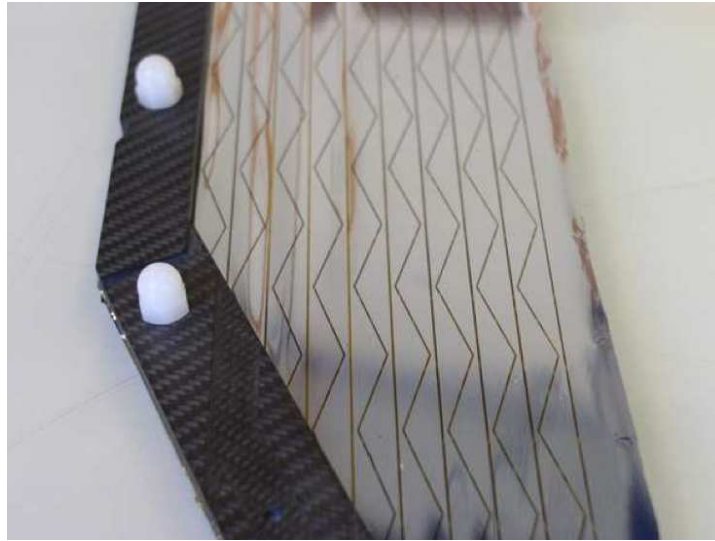


Figure 2.14: Vernier pattern of chambers cathodic foils.

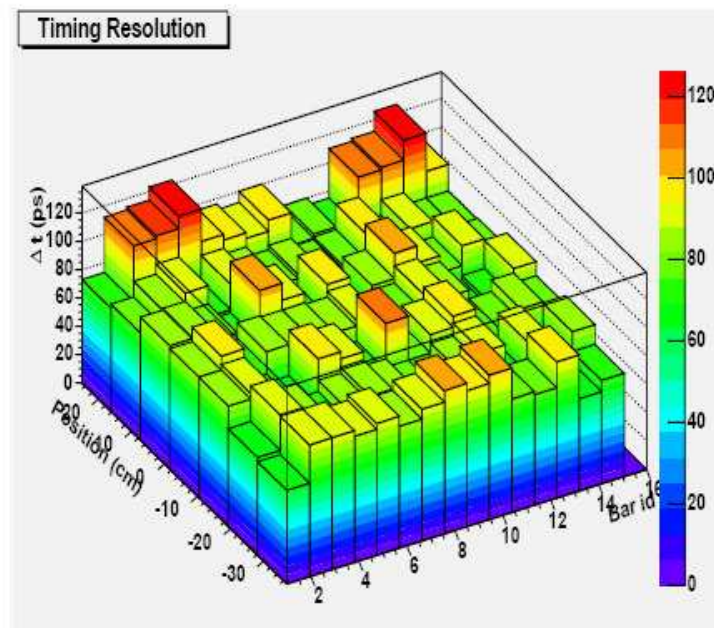


Figure 2.15: Time counter resolution as function of impact point.

by two Avalanche Photo Diodes (APDs), practically insensitive to the magnetic field. The positron impact point is reconstructed using both the ratio between the signals for bars and

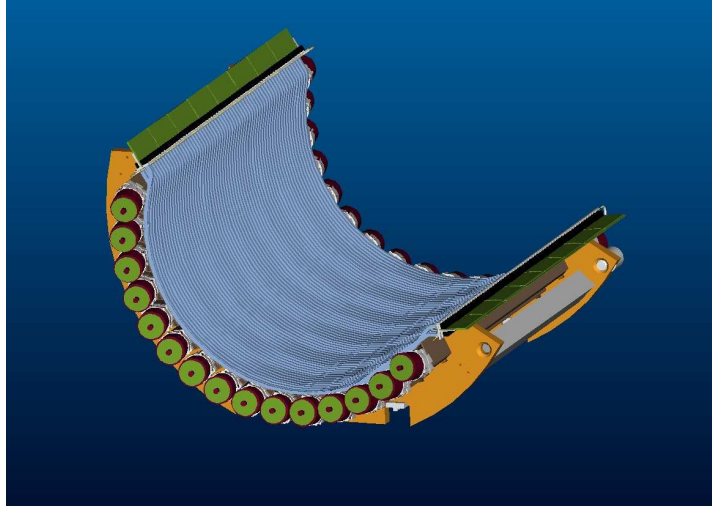


Figure 2.16: Timing counter structure.

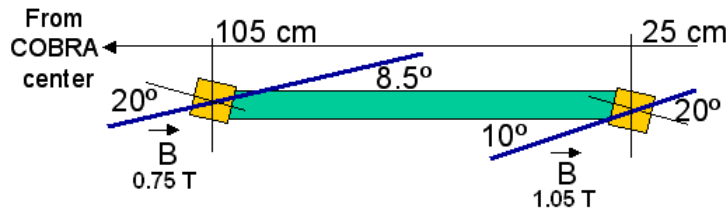


Figure 2.17: Timing counter positioning scheme.

the information from the fibers. The arrival time is instead measured by the bars only. The whole apparatus is at a 29.5 cm radius and its acceptance is 145° in ϕ and $25 < |z| < 95$ cm. The shape of the detector was designed so that a positron will cross on average two or three bars per event. In order to protect PMTs from Helium, the TC is isolated by a shell of plastic where nitrogen is fluxed.

2.3 The photon detector

The photon detector is the most challenging and innovative part of the experiment. We give here a general description of this device but its characteristics will be thoroughly examined in the following chapters. The MEG calorimeter is a $0.8m^3$ C-shaped volume filled with about 800 liters of liquid xenon cooled ($T = 165$ K) by a pulse-tube refrigerator and by auxiliary liquid

nitrogen lines mounted on the internal part of the cryostat. The detector is outside COBRA and , thanks to the resistive coils in Helmholtz configuration, it is immersed in a magnetic field with value less than 50 gauss. The internal and external radii of the active volume are 65 cm and 112 cm respectively, for a $17 X_0$ thickness, and angular extension $\pm 60^\circ$. The calorimeter covers a solid angle of $\approx 12\%$ ($|\cos\theta| \leq 0.35$ and 120°). On the internal surface immersed in the liquid xenon and mounted on an aluminum and plastic (peek, only inner face to minimize γ conversion) structure (fig. 2.18), there are about 846 2'' photomultiplier tubes developed with HAMAMATSU Photonics Inc. to work at low temperature, in a low magnetic field, in UV-region and at high pulse rate.



Figure 2.18: Picture of photomultipliers mounted on internal aluminum and peek structure.

A schematic layout of the γ -detector is shown in fig.2.19. All the photon variables (energy, direction and time) are measured with it. Energy and timing are related to the time and the collected light measured by each phototube. Direction is measured using the starting point on the target, extracted from the positron track, and the photon first conversion point, obtained

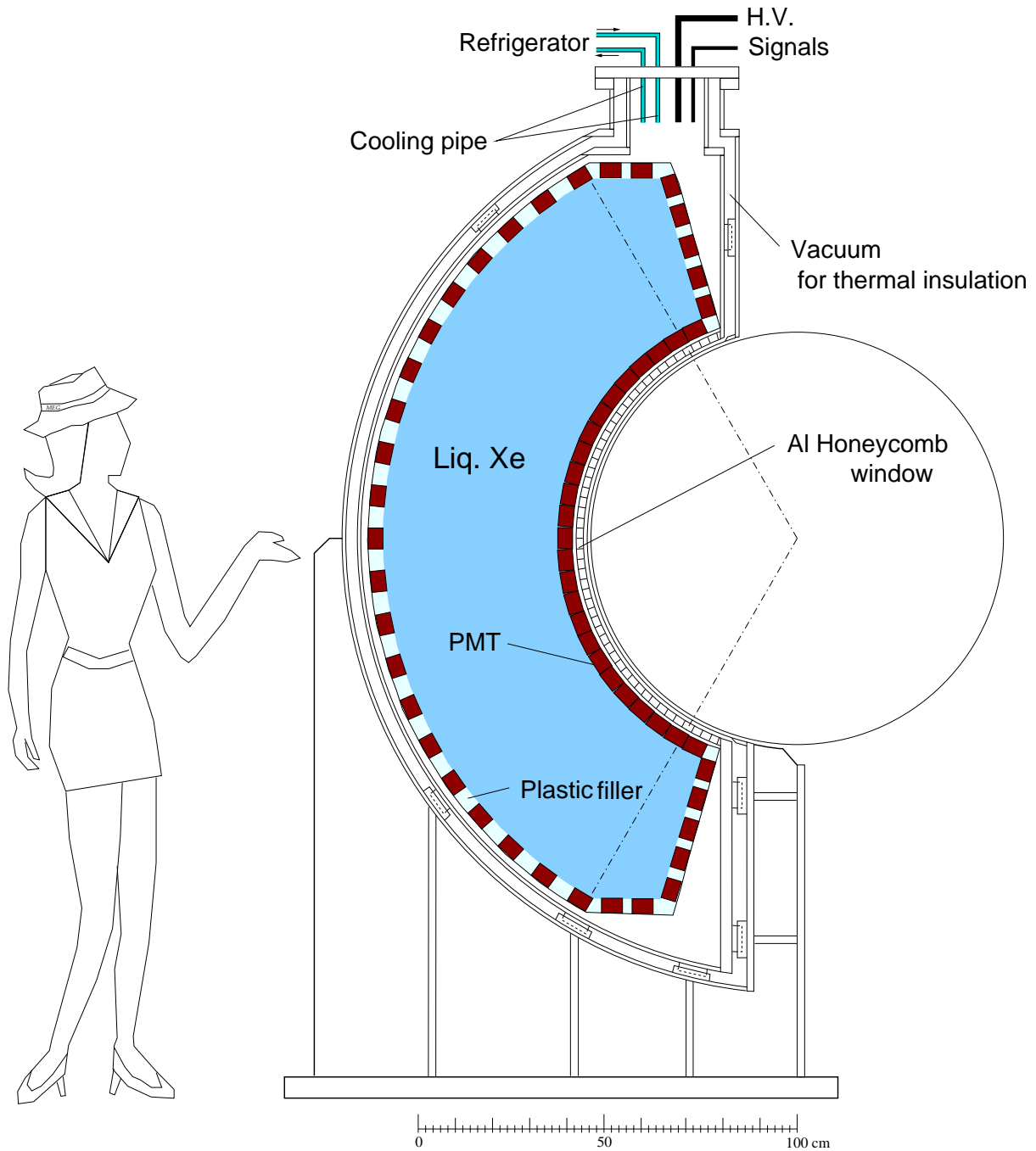


Figure 2.19: Cross section of calorimeter.

by the light distribution in the calorimeter. In order to extract these information and remove accidental pileup events, all pmt waveforms are digitized and registered (see next section).

2.4 Trigger and DAQ system

2.4.1 The trigger system

The MEG experiment trigger uses, for the selection of events and the rejection of the background, the signals of the calorimeter (the calorimeter PMT) and TC (the TC PMT), while it ignores drift chamber ones because they are too slow. Information is analyzed from three types of electronic boards VME (type 1, type 2, Ancillary) that digitize signals and process them using basic algorithms written on the FPGA (Field Programmable Gate Arrays) present on the boards (fig.2.20). The photon energy is measured adding the light collected by each

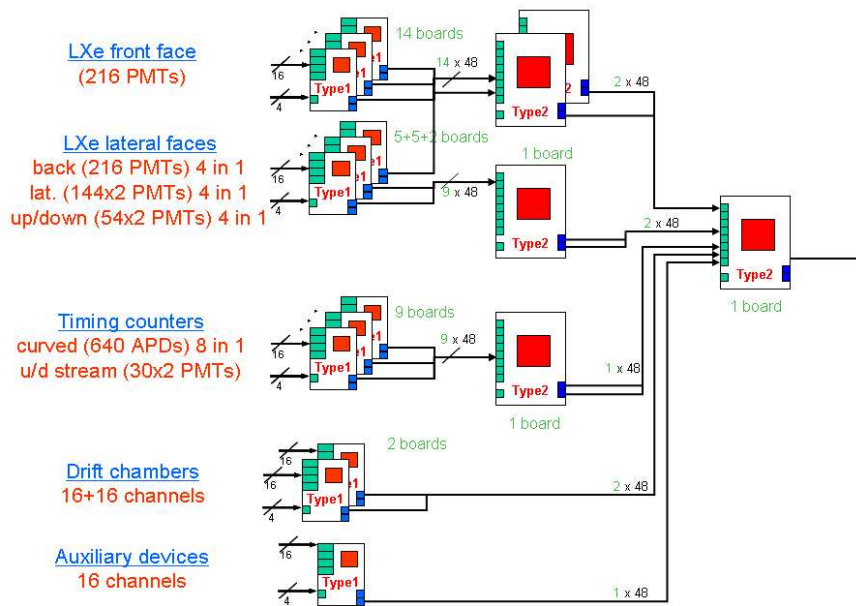


Figure 2.20: Trigger scheme.

PMT of the calorimeter. Its direction is reconstructed using the information of the PMT with the largest signal. The trigger is also able to digitize the waveform of the PMT signal (100 MHz sampling) in order to make a real-time subtraction of the pedestal, the rejection of certain sources of noise and estimate the time of arrival of photons from the front edge of the signal. The positron arrival time is provided by the TC. The direction is determined by the impact point on TC that is reconstructed using the information from hit bar and fiber. Because of

the magnetic field and the resulting curve trajectory of the positron, the reconstruction of the collinearity of the photon and the positron, without the knowledge of the track, is not trivial. To overcome this problem, it has been created a "look up table" that associates to a positron point of impact a photon conversion point in the calorimeter. This table is validated using a mix of data and MC. The final trigger rate is about 5 Hz.

2.4.2 The DAQ system

The signals from the calorimeter, the TC and the chambers are digitized using the Domino Sampling Chip (DRS[41]), developed at PSI. It consists of 1024 capacitors which are sequentially charged from the incoming signal. When the trigger generates a signal, the DRS is stopped and the contents of the 1024 capacitors are read. This chip allows a sampling speed of 2 GHz (500 ps bin width), necessary to reject pileup events and obtain the desired timing resolutions.

2.5 MEG experiment software

MEG software is divided in two sections: one for the simulation (MEGMC) and one for the reconstruction of events (MEGAnalyzer). The data produced by the simulation can be read directly from MEGAnalyzer or processed by an intermediate code called MEGBartender. MEGMC is based on standard packages of Cern in Fortran (Zebra[47] and GEANT3[48]) while the MEGAnalyzer and MEGBartender were developed in a C++ environment called ROME, derived from the CERN ROOT package[49]. We will describe briefly the main elements making up the software whose scheme is shown in fig.2.21.

2.5.1 The MonteCarlo GEM

GEM, the simulation program MEG experiment, is written in FORTRAN77[50] and based on GEANT3. The Code is divided into three sections:

- the simulation of physical events;
- management of geometry, which is divided into subsections for each specific detector, based on the routines of GEANT3 (GSPOS, GSVOLU ,...);
- routines of general utility (input / output data, histograms, etc ...).

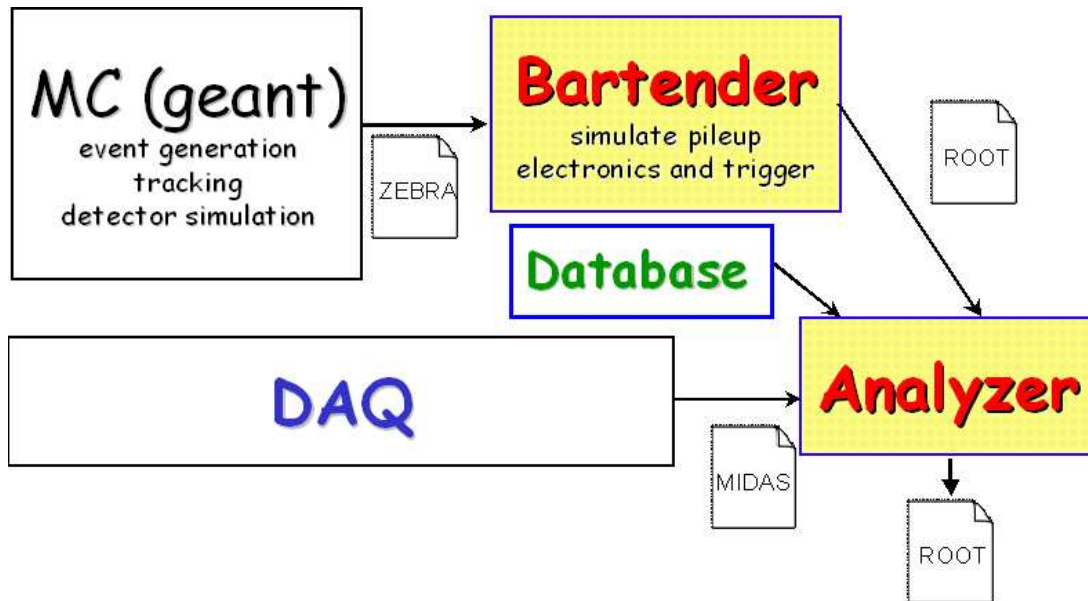


Figure 2.21: Scheme of the structure of MEG software.

The generation of the events is performed by the routine MEGEVE, which can simulate events of signal, correlated and accidental background, calibrations, etc ... each with the appropriate position, energy and time distributions. MEGEVE gives as output the production vertex and the pulse of the particle at the initial time. Output variables of MEGEVE are transferred to GEANT3 routines (GSVERT, GSKINE, ...) in order to track the particles in the detector. At each step of the trajectory and deposit of energy the signals of all detectors are simulated using routines specifically developed by the collaboration. In particular for liquid Xe calorimeter, the photon path is simulated taking into account some physical characteristics of the sensitive medium:

- Rayleigh distribution in Xenon, whose differential cross section is proportional to $\lambda^4(1 + \cos^2\theta)$ where λ is the wavelength of the light and θ is the angle between the initial and the scattered photon direction.
- absorption of scintillation light by impurities in Xenon, described by an absorption length λ_a .
- absorption by the quartz window of the photomultiplier tubes ($\approx 3 - 4\%$ for normal incidence).

- total or Fresnel reflection at the interface between the Xenon and the photocathode surface.

GEM output is a ZEBRA file in which are collected characteristics of the event (type of particle, initial pulse, etc ...) and the physical parameters associated with signals produced by each detector (charge, rise time of the signal, etc. ...). In particular, for the electromagnetic calorimeter, GEM provides out the arrival times of scintillation photons on each photomultiplier sampled at intervals of 250 ps, half of sampling speed of the real experiment hardware. In addition to this information, variables useful in analysis and reconstruction phase (charge collection and time measured by each phototube, the total charge collected by each face of the calorimeter ,...) and others simulated variables (total energy released, the photon conversion point in the Xenon, or the first interaction in the case of Compton scattering, the angles of the particle in the calorimeter) useful to compare the true and reconstructed values, for quality check of the algorithms, to determine the expected resolutions, etc ..., are saved.

2.5.2 The data analysis structure: ROME

ROME is an "object oriented environment" for analysis programs, developed for MEG, structured to include all the most common operations of data analysis (loop on events, management of histograms, etc ...). A group of class C++ manages all procedures, leaving to the user the task of defining the analysis algorithms. ROME is interfaced with the ROOT libraries for analysis and storage of data, with the Midas[51] and Zebra libraries for reading the data, with mysql 4.0[52] libraries for the database. The structure of the analysis is written in XML language and transformed into C++ classes by a special translator, called ROMEBuilder. The ROMEBuilder also creates an executable file, documentation of the structure and a configuration file where you can manage several global parameters. The structure of Rome is reported in fig.2.22. In ROME there are six items, based on similar properties ROOT: task, histogram, tree, folder, steering parameter, bank.

- Task. Tasks are objects that perform some action, such as the reconstruction of kinematic variables in the different detectors. When the XML is compiled generate two files for each selected task: an include file (. H) and a source file (. Cpp), which can be modified by the user.
- Folder. The folder are objects that allow the storage of data. In particular, each folder can contain data from a single event and is overwritten, event to event, unless you select

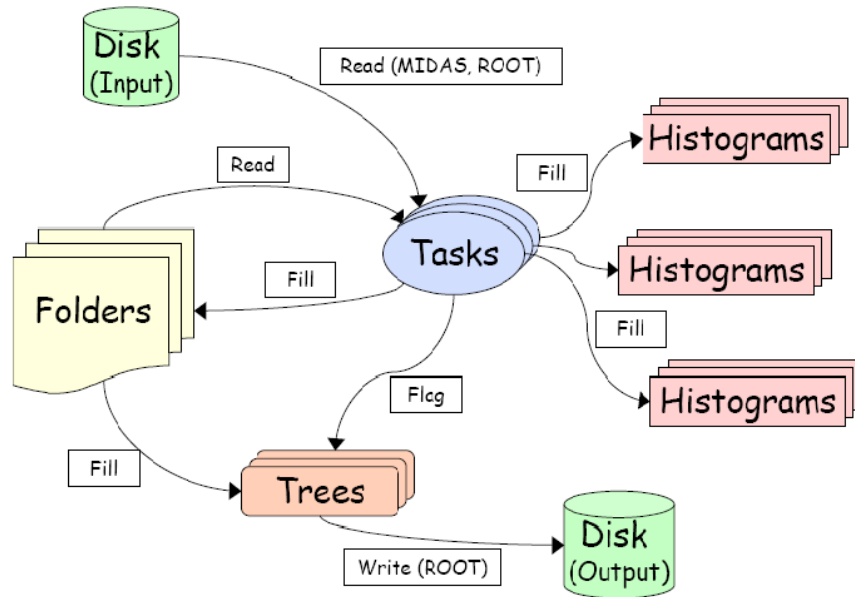


Figure 2.22: Rome structure.

the appropriate option to save the contents.

- Tree. The tree of ROME, inherited from ROOT, are objects that allow the storage of large amounts of data with an "event-list" structure.
- Histogram. Histograms are inherited from ROOT.
- Steering Parameter. ROME allows the user to define parameters to select the tasks to use, the databases, the input and output format and so on. These parameters must be specified before the analysis starting within a configuration file, created automatically by ROMEBuilder and editable by the user.
- Bank. A bank is a substructure of an event that can contain only one type of data, both single values that value arrays. ROME provides access to ZEBRA and Midas banks. The Midas bank is structured as shown in fig.2.5.2.

The MEGAnalyzer

The MEGAnalyzer is a code written in ROME environment that contains the algorithms to be applied to the data. The MEGAnalyzer inputs are ZEBRA files produced by the Monte Carlo,

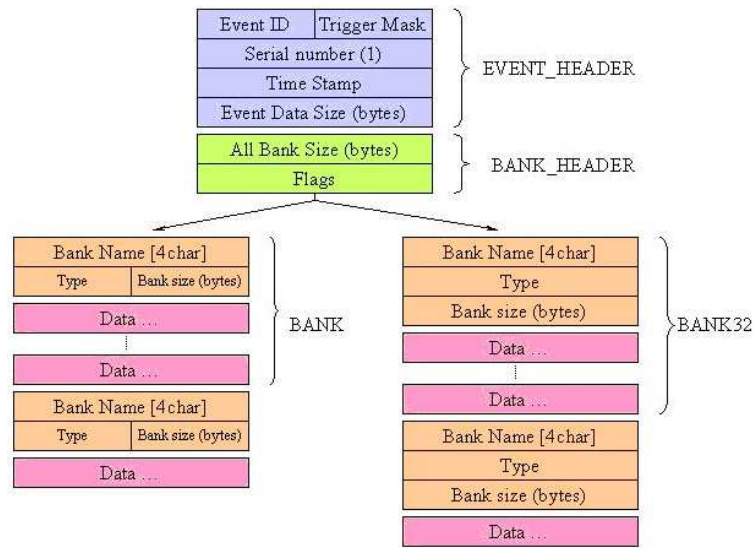


Figure 2.23: Midas bank structure.

Midas files produced by data acquisition, and ROOT files produced by MEGBartender (see next section) or MEGAnalyzer. The MEGAnalyzer is structured with specific tasks for the analysis and reconstruction of events within a single detector. In particular, for the calorimeter the algorithms to reconstruct the physical variables well as the calibration procedures have been implemented. The MEGAnalyzer returns output data reconstructed and organized in tree root.

The MEGBartender

The MEGBartender is an intermediate code between GEM and MEGAnalyzer, written in ROME environment. It does two important things:

- It simulates the signal waveforms and the response function of each detector using the information provided by GEM. The simulated waveforms are used to test the analysis algorithms implemented in MEGAnalyzer.
- It sums different event types, simulated and real, to study the waveforms in case of overlapping background ("pile up"). So it is possible to simulate pile-up in order to develop appropriate algorithms for separation and recognition.

Chapter 3

The Liquid Xenon Calorimeter

The photon kinematical variables (energy, time and position) are measured by the liquid xenon calorimeter. In order to accomplish this job, a new kind of large acceptance, large mass (roughly 2.2 Tons) calorimeter based on liquid xenon scintillation light was developed. In this chapter, we discuss the main components of this detector, starting from the liquid xenon properties to explain the whole detector structure and development.

3.1 Liquid Xenon as scintillation medium

Since the discovery of their scintillating proprieties, liquid rare gases, are considered as optimum mediums for radiation detectors. In particular the liquid Xenon is used for various applications from dark matter search to medical applications. The properties that make it an excellent scintillator are:

- Liquid Xenon is free from problems of non-uniformity, cracks and aging. It is also free from radioactive isotopes too.
- The high atomic number ($Z=54$) and density ($\rho \approx 2.95 \frac{\text{g}}{\text{cm}^3}$) cause a little radiation length ($X_0 = 2.77 \text{ cm}$). This allows a compact structure detector.
- High scintillation photon production. For each MeV of deposited energy, about 40000 scintillation photos are produced, comparable with NaI crystals ($\approx 80\%$).
- High transparency to its scintillation light.
- Very fast response.

There however are some problems related to the use of xenon:

- The scintillation light wavelength is ≈ 178 nm in the vacuum ultraviolet (VUV).
- The VUV light is absorbed from common impurities (water and oxygen).
- Xenon boiling temperature is 165 °K: a cryogenic system is necessary.

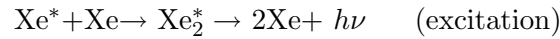
Table 3.1 summarizes xenon characteristics.

Density	2.95 g/cm ³ [54]
Liquefaction and fusion temperature	165 K, 161 K [53]
Average deposited energy for scintillation photon	24 eV [55]
Radiation length	2.77 cm [56]
Decay times	4.2 ns, 22 ns, 45 ns [55]
Wavelength of emission light peak	175 nm [60][61]
Absorption length for scintillation light	> 300 cm (purified) [57]
Rayleigh scattering length	≈ 40 cm
refraction index (on peak)	1.56 [58][59]

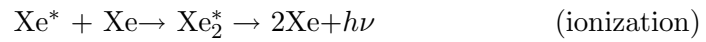
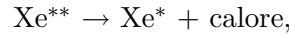
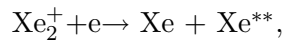
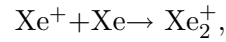
Table 3.1: Liquid Xenon characteristics.

3.1.1 Emission mechanisms and light yield

There are two different ways to produce scintillation light in xenon: ionization and excitation of the atoms.



or



It is important to note that:

- the scintillation light emission proceeds via the production of excimers, Xe₂ molecules existing only in an excited state, which eventually de-excite produce a VUV photon ($\lambda_{peak} = 178$ nm, $\Delta\lambda = 14$ nm FWHM).

- scintillation photons have an energy of 7.1 eV, less than the first excited state of Xenon atom (8.3 eV); so the reaction $h\nu + Xe \rightarrow Xe^*$ is forbidden and the self-absorption of pure liquid Xenon is very small.
- The excimer production and de-excitation mechanisms have different characteristic times for ionized or excited atoms, and the ratio between ionization and excitation is different for different particles. In particular, the fast components (4 ns, 22 ns) are related to the de-excitation of excimer singlet and triplet states that are dominant for heavy particles like α 's that mainly produce the excitation process. The slow component (45 ns) is related to ionization and recombination and it is dominant for photons or relativistic electrons. Fig. 3.1.1 shows the different waveforms for α and γ events.

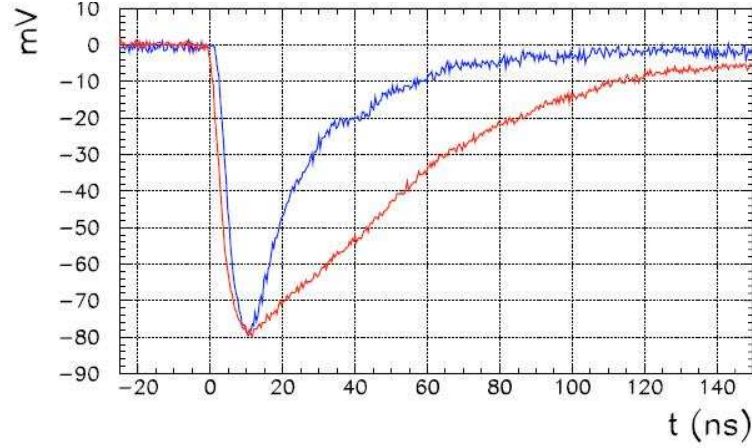


Figure 3.1: Pulse shape for α -particles (blue) and γ s (red) in liquid xenon.

The light emission yield is given in terms of W_{ph} , the average energy needed to produce a scintillation photon. The total number of emitted scintillation photons (N_{ph}) comes from either ionized (N_i) and excited (N_{ex}) Xe atoms:

$$N_{ph} = N_i + N_{ex} \quad (3.1)$$

By defining W_i and E_0 the average energy to create an electron-ion pair and the deposited energy in the Xenon respectively, we can write:

$$W_{ph} = \frac{E_0}{N_{ph}} = \frac{E_0}{N_i + N_{ex}} = \frac{E_0}{N_i} \cdot \frac{1}{1 + \frac{N_{ex}}{N_i}} = W_i \cdot \frac{1}{1 + \frac{N_{ex}}{N_i}} \quad (3.2)$$

The W_i value is reported in literature and is 15.1 eV [62]. It is important to note that different ionizing particles have different ratio $\frac{N_{ex}}{N_i}$ due to their different ionization density. In table 3.2 W_{ph} for relativistic electrons, photons and α -particles are reported.

Particle type	W_{ph} (eV)
relativistic e/ γ	23.7 ± 2.4 [63]
α -particle	19.6 ± 2.0 [63]

Table 3.2: Average energy needed to produce a scintillation photon in liquid Xe for different particles.

3.1.2 Attenuation of scintillation light and impurities

Attenuation consists of scattering and absorption. Because the size of scattering center is smaller than the wavelength of the radiation, the Rayleigh scattering well describes the diffusion inside Xenon. We can write the attenuation length λ_{att} as:

$$\frac{1}{\lambda_{att}} = \frac{1}{\lambda_{Ray}} + \frac{1}{\lambda_{abs}} \quad (3.3)$$

- **Rayleigh scattering.** Rayleigh scattering length depends on wavelength of photons (λ), density (ρ) and the refractive index of the liquid. The inverse of the scattering length for a single component can be written as [64]:

$$h = \frac{8\pi^3}{3\lambda^4} \left[kT\rho^2 k_T \left(\frac{\delta\epsilon}{\delta\rho} \right)_T + \frac{kT^2}{\rho c_v} \left(\frac{\delta\epsilon}{\delta T} \right)_\rho \right] \quad (3.4)$$

where k is the Boltzmann's constant, T the temperature, k_T is the isothermal compressibility, c_v is the heat capacity at constant volume and ϵ is the (real part of the) dielectric constant. For liquid Xenon at 178 nm we obtain $\lambda_{Ray} \approx 45$ cm in agreement with experimental measurements [65][66][67][68]. For non-pure fluids an additional contribution comes from fluctuations in the concentrations of impurities. For sufficiently diluted impurities this contribution is [65]:

$$h_{imp} = \frac{8\pi^3}{3\lambda^4} \left[\frac{xM}{N_a} \left(\frac{\delta\epsilon}{\delta x} \right)^2 \right] \quad (3.5)$$

with x impurity concentration, M molecular weight and N_a Avogadro's number. For liquid Xenon at 178 nm we obtain:

$$h_{imp} \approx 10^{-8} \left(\frac{x}{1 \text{ ppm}} \right) \text{ cm}^{-1} \quad (3.6)$$

negligible for low impurities level.

- **Absorption length and quenching impurities.** Due to the scintillation mechanism self-absorption should be small. Photo-absorption is dominated by impurities in the liquefied gas, in particular water and Oxygen. Figure 3.2 and 3.3 shows oxygen and water attenuation cross sections as function of wavelength with the Xenon scintillation spectrum superimposed.

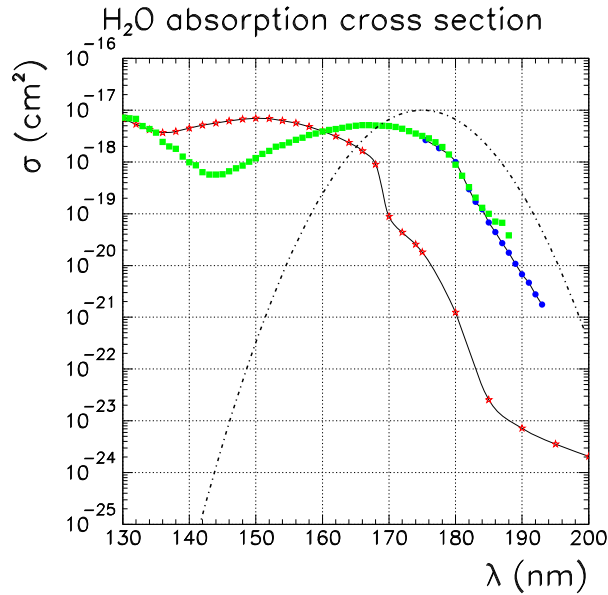


Figure 3.2: Cross section of absorption in water as function of the wavelength. Red dots are in liquid phase, green and blue ones in vapour. The dash gaussian is the emission spectra of xenon.

Quenching processes of LXe are poorly known. One of the possible mechanisms is capture of the ionization electron. In this case only the recombination process would be influenced. Since α -particles and γ -rays have different behavior in liquid Xenon (see 3.1.1) we can therefore think of using the first ones for studying absorption and second ones to measuring quench effects.

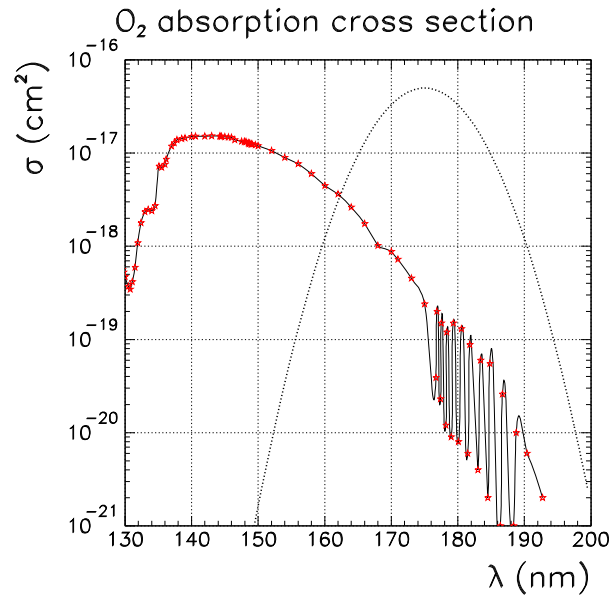


Figure 3.3: Cross section of absorption in oxygen as function of the wavelength. The dash gaussian is the emission spectra of xenon.

3.2 Calorimeter cryogenic equipment and purification system

Xenon liquefaction temperature is 165°K, its production is expensive and not very fast. The MEG calorimeter is the largest xenon detector in the world, using around 1000 liters of liquid Xenon. A specific cryogenic system was developed in order to handle it. Figure 3.4 shows a schematic view. Table 3.3 summarizes xenon main cryogenic proprieties. Below we explain all the single parts of the cryogenic system.

Gas Xenon storage. This storage consists of eight tanks with each 250 liters of volume. Here xenon is stored in gas phase (pressure of 70 bar at temperature of 25°C). The GXe storage is connected to the LXe storage tank, detector and purification system. Xenon can be transferred to the LXe storage using of a pressure difference. When the gas is transferred, it is continuously liquefied and pressure inside the LXe storage is kept stable around 0.1 MPa. Transfer continues until pressure equilibrium is established: at the end about 1.5 Kg of xenon remain inside the GXe storage. The whole liquefaction process takes one month. In order to recover the xenon in GXe storage, the tanks are cooled down using LN₂ and LXe storage is pressurized up to 0.18 MPa by using a heater. During the running and stopping period xenon

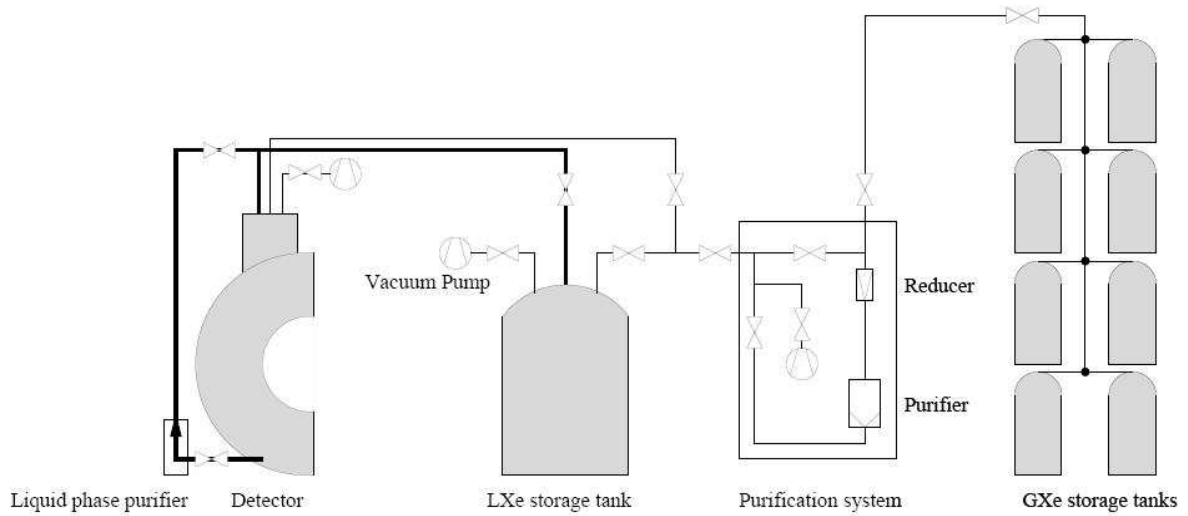


Figure 3.4: Cross section of absorption in oxygen as function of the wavelength. The dash gaussian is the emission spectra of xenon.

is stored in the detector or in the LXe storage but, during long-term shutdown period, it is usually stored in the GXe storage because no control systems or electric power are needed. Figure 3.5 shows a picture of tanks system.

Liquid Xenon storage tank [69]. The LXe storage has a maximum capacity of 1000 liters of liquid xenon. Its structure is very similar to the detector cryostat (see next paragraph). A heater, a pulse tube cryocooler and a liquid nitrogen line are mounted at the top or bottom of the dewar to allow transfer and storage operations. The tank is connected to detector by vacuum insulated pipes, and the liquid xenon transfer is made by using pressure difference. The operation needs about three days and is much faster than gas phase transfer. When all cooling systems are stopped, xenon pressure inside of the tank increases about 0.1 MPa in about 40 hours: therefore the system is safe in case of shutdown or control system fault for several hours. Figure 3.6 shows the 1000l dewar.

Cryostat The cryostat had to meet some important requirements: it must endure thermal stress in the range between room temperature and 165°K, pressure about 1.5 bar plus liquid xenon weight during normal operation and more than 2 bar during transfer, and finally it must be built in order to minimize the γ conversion probability on the inner face. Because it is located in a strong magnetic field, it is made of non magnetic and low permeability materials. The

Property	Value
Density	2.95 g/cm ³
Saturation temperature (K)	164.78
Latent heat (boiling)(kJ/kg)	95.8
Latent heat (melting)(kJ/kg)	1.2
Specif heat (kJ/kg)	0.3484
Viscosity (Pa · s)	5.08 × 10 ⁻⁴
Temperature/pressure at triple point (K,MPa)	161.36,0.0815

Table 3.3: Xenon cryogenic main properties.



Figure 3.5: Gas xenon storage tanks in the experimental area.

cryostat structure consists of two C-shape vessels: the inner one (the cold vessel) in contact with liquid xenon and the external one (the warm vessel). The shape maximizes the solid angle for γ acceptance and minimizes the xenon volume. For thermal insulation, the volume between the two vessels is evacuated and super insulation layers are installed to suppress heat from radiation. A pulse-tube refrigerator and a liquid nitrogen cooling pipe are mounted at the top to liquefy



Figure 3.6: 1000l liquid xenon storage tank.

xenon and to keep the temperature stable. Table 3.4 summarizes the heat load of the different parts of the calorimeter. The use of a pulse tube cryocooler is an important improvement in cryogenic systems [70] since no moving parts are in contact with the cold liquid thus reducing vibrations. An auxiliary liquid nitrogen line (fig. 3.7) is in contact with the external part of the cold vessel for precooling or to be used in case of problems with the main cryogenic system. In order to monitor xenon temperature and pressure, several pt-100 are located on internal and external surfaces of the cold vessel. Liquid xenon level is monitored using a capacitance level meter [71]. All the cables from sensors and PMTs pass through feedthroughs attached on three large nozzles at the top of cryostat. They also house vacuum pumps, the refrigerator system, the pressure/vacuum gauges and various valves for xenon operations. Particular care was paid to the design the gamma ray entrance window of the calorimeter in order to minimize the conversion of γ 's. Both cold and warm vessel have a very thin steel windows (about 0.5

Type of load	Cryostat part	Value(W)
Radiation	From outer to inner vessel	3.1
Conduction	Nozzle via gas xenon	0.2
Conduction	Nozzle via bellows	4.6
Conduction	Support (brace and supporting pipe)	6.3
Heat generation	PMT (65 mW/PMT)	52
Conduction	PMT HV and signal cables	50
Total		116.2

Table 3.4: Heat load of the calorimeter.



Figure 3.7: Liquid nitrogen line attached on external part of cold vessel.

mm). The inner window is reinforced with a panel of aluminum honeycomb and carbon fibers (fig.3.8). The length of the whole window is about $0.075 X_0$.

Purification system. The purification system consists of two parts: gas and liquid phase purification. The gas system consists of a diaphragm pump that circulates xenon through a gas-getter to remove water, oxygen, nitrogen, carbonic monoxide and anhydride, hydrogen and hydro-carbon molecules down to 1.0 ppb; it was successfully used with a 100l prototype [73]. Unfortunately the process speed ($\approx 100 \text{ cm}^3$ of liquid/hour) is very low. For this reason, a purification system with circulation of liquid xenon was developed [72]. It consists of a cryogenic centrifugal pump and a purifier cartridge. In addition, to remove oxygen, a purifier using copper beads, developed at CERN for liquid Argon, was installed at the outlet of pump. The circulation speed is $\approx 35 \text{ l/hour}$ allowing a complete liquid xenon circulation in about 25 hours. Because the circulation pump induces noise on the detectors, it is possible to perform

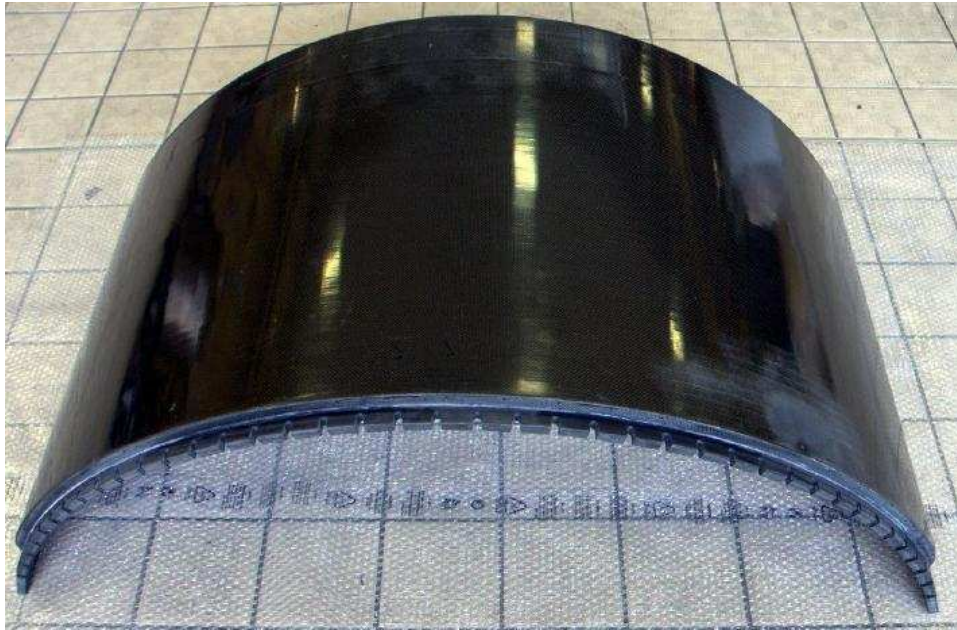


Figure 3.8: Inner panel picture.

the liquid phase purification only during beam-maintenance periods. Figure 3.9 shows a picture of liquid phase purification system.

3.3 PMTs

The calorimeter PMTs must work in the following conditions:

- **VUV region.** Xenon scintillation light is emitted in the VUV region.
- **Magnetic field.** The calorimeter is immersed in a low magnetic field (≈ 50 gauss).
- **Cryogenic temperature.** The PMTs must be immersed in liquid Xenon (-108 °C) to efficiently collect the light.
- **High rate background.** During data taking, there is high rate background by neutrons and gamma rays.

For these reasons we used a new kind of a new model of photomultiplier (R9869) developed with Hamamatsu photonics. These PMTs have a photocathode made up of Bialkali (K-Cs-Sb) to work at low temperature and to have good quantum efficiencies in VUV region ($\approx 15\%$). A

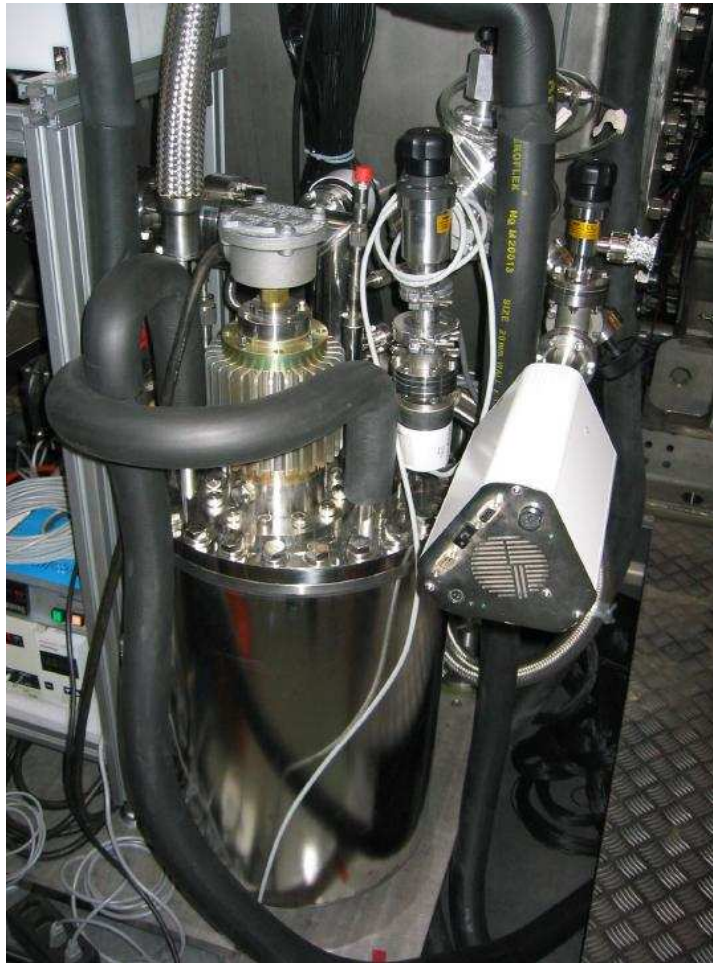


Figure 3.9: Liquid xenon purification system.

quartz window is used to transmit the light. Aluminum strips are put on the photocathode to reduce the sheet resistance at low temperature (see next paragraph). The PMTs have a compact structure with twelve amplification stages to work in magnetic field. Two Zener diodes are used in last two steps to avoid an effect of overlinearity in high background conditions (see next paragraph). Figure 3.10 shows a picture of R9869 photomultiplier.

3.3.1 PMTs in high background condition

The MEG experiment works in an environment with a high low energy photon background. This intense background may produce two distinct effects on the gains of the PMTs.



Figure 3.10: Phototube R9869

Photocathodic resistance at low temperature The resistance of the photocathode of the photomultiplier increases at low temperatures [75]. In high rate condition, it can cause a drastic decrease in the response of the PMT because of spatial charge effects. The phenomenon was observed in a prototype [73] reproducing the high background with a LED (BL), and observing the signal of a second LED (SL). Figure 3.11 shows the behavior of a phototube different from R9869 (R6041): when the BL was on (high rate ON) we observed an exponential decrease of the SL light, which returned to its initial value when BL was off (High rate OFF). This effect is not present at room temperature and was interpreted as an resistivity increase at low temperature. The problem was solved by inserting strips of aluminum on the photocathode to reduce its resistivity. Figure 3.12 shows the results for different types of photomultipliers. It is clear that the phototube with a greater density of aluminum strips is not influenced by the temperature. All tests were performed in Argon to reach temperatures lower than liquid Xenon (Argon liquefaction point -150°C).

Gain alteration by anodic current The gain stability of a photomultiplier depends on the operating voltage but, the anodic current I_a , the current due to the flux of photoelectrons from the photocathodic surface to the anode, can modify the voltage between the last dynode and the anode and then modify the gain. The anodic current is correlated to the number of photons that hit the photocathode and a high background of low energy photons can increase it. The gain variation can be expressed as a function of the ratio $\frac{I_a}{I_b}$ between the anodic current and the bleeder current. Figure 3.13 shows the gain behavior when the ratio increases. In order

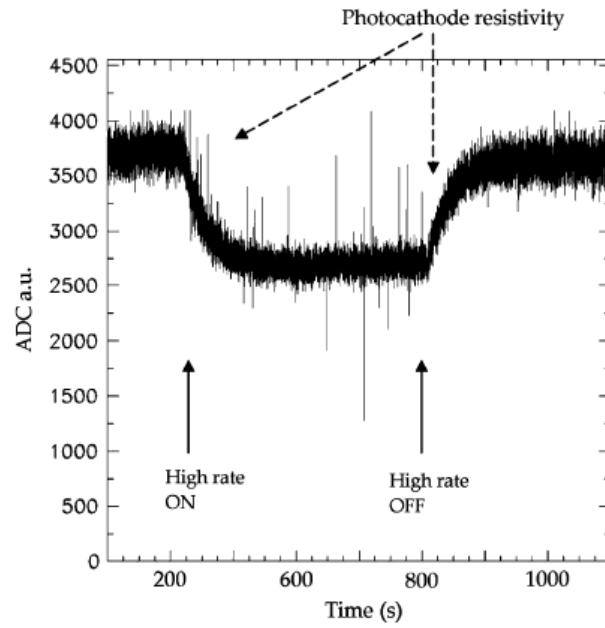


Figure 3.11: Response of R6041 set Pmt with low temperature and high background.

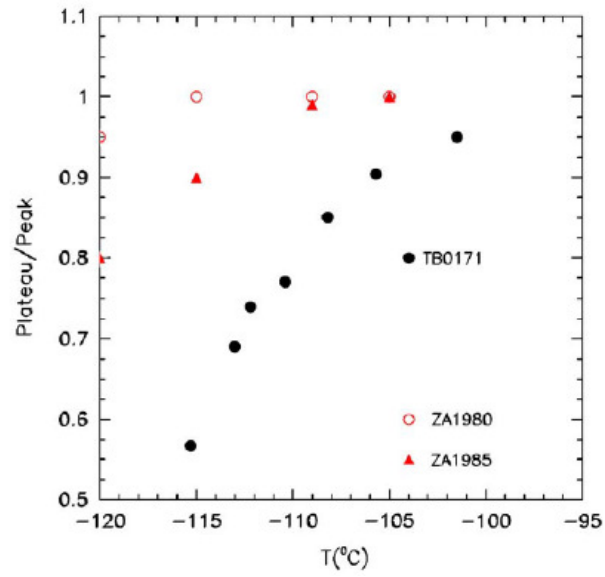


Figure 3.12: Photo cathode resistivity as function of temperature: TB0171: set R9288 with low aluminum strip density, ZA1980 and ZA1985: set R9869 with double aluminum strip density.

to avoid any rate dependency (overlinearity) effect, it is necessary to keep this ratio less than 0.01. To keep the voltage between the last dynodes and the anode stable, MEG PMTs have

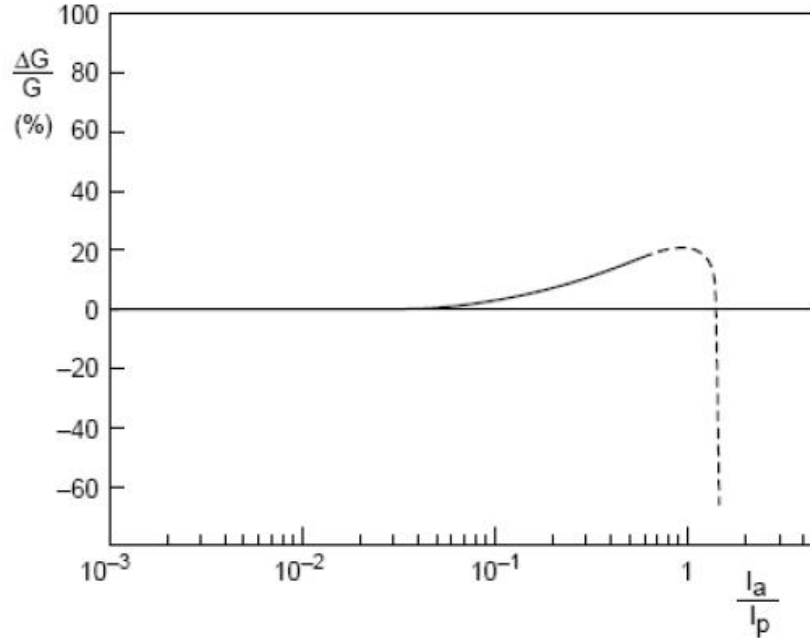


Figure 3.13: Gain variation (overlinearity) as a function of ratio $\frac{I_a}{I_p}$.

two Zener diodes in the last two amplification steps instead of normal resistors (fig.3.14).

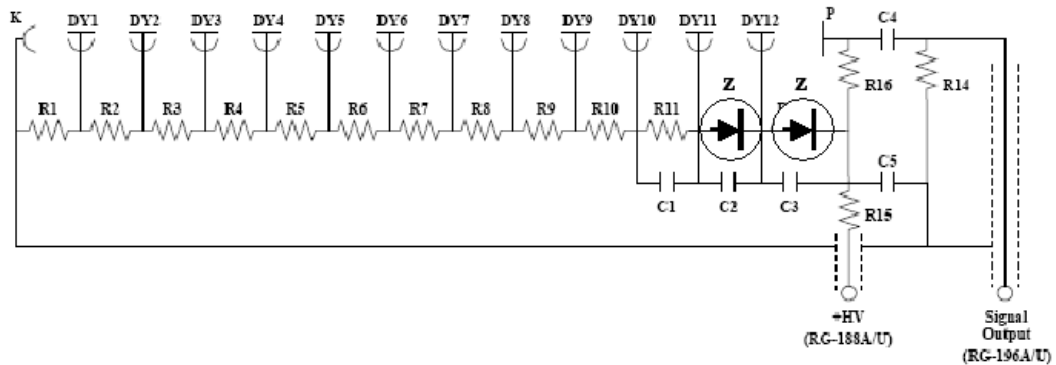


Figure 3.14: Diagram of photomultiplier with two Zener diodes instead of the usual resistors in the last two steps of the bleeder circuit.

In this way the overlinearity is eliminated and the fast gain decreasing happens at higher $\frac{I_a}{I_p}$ ratios. Figure 3.15 shows the response comparison between two phototubes with and without

diodes respectively. The operation of one half of the pmt's was tested in a small xenon facility

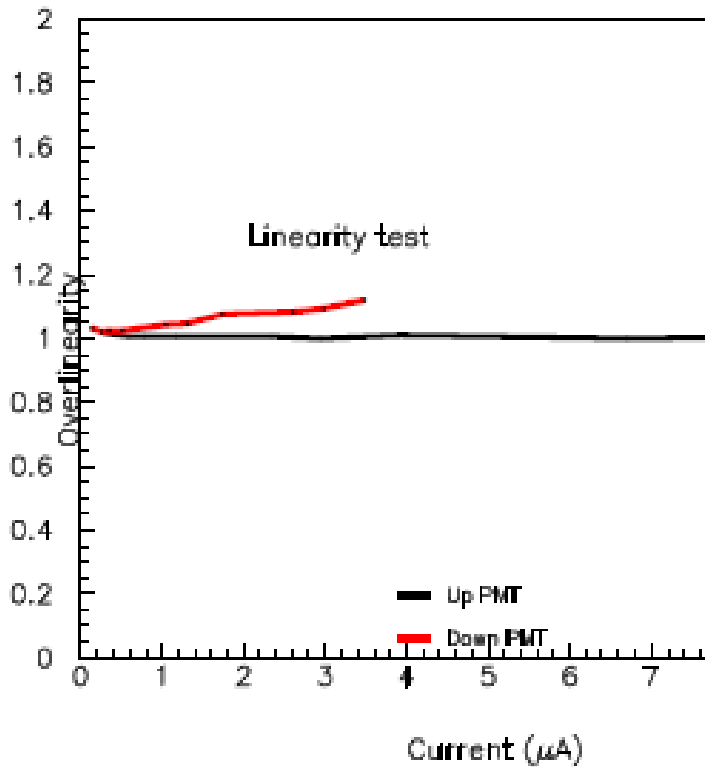


Figure 3.15: Response comparison between two phototubes with (black) and without (red) diodes respectively.

in Pisa [74] at values of the anodic current higher than that of the experiment. All the pmt's tests showed a linear behavior.

Chapter 4

The Liquid Xenon detector calibration methods

The MEG experiment success is related to the very high precision in measuring the variables of μ -decay products, in particular γ 's ones. In order to ensure that the required calorimeter performances are reached and maintained during the whole run, we developed several complementary and redundant methods to calibrate and monitor the behavior of the detector. The following chapter gives an overview of all used and future calibration methods.

4.1 LXe optical proprieties and PMTs characteristics

The calorimeter performances are strongly related to the liquid xenon optical proprieties and the PMTs response characteristics: the amplifications (gains g) and quantum efficiencies (QEs).

4.1.1 LED and PMTs gains

In order to estimate the gains, 44 LEDs are mounted on the calorimeter lateral and back faces in twenty different positions (fig.4.1), able to lighten all photomultipliers. Assuming a linear response of PMTs and a Poisson distribution for photoelectrons, we can write:

$$q = gN + q_0 \quad (4.1)$$

$$\sigma^2 = g^2N + \sigma_0^2 \quad (4.2)$$

with q and σ the charge and the standard deviation of signal pulse, g the gain, N the number of photoelectrons, q_0 and σ_0 the charge and the standard deviation values correspond to the

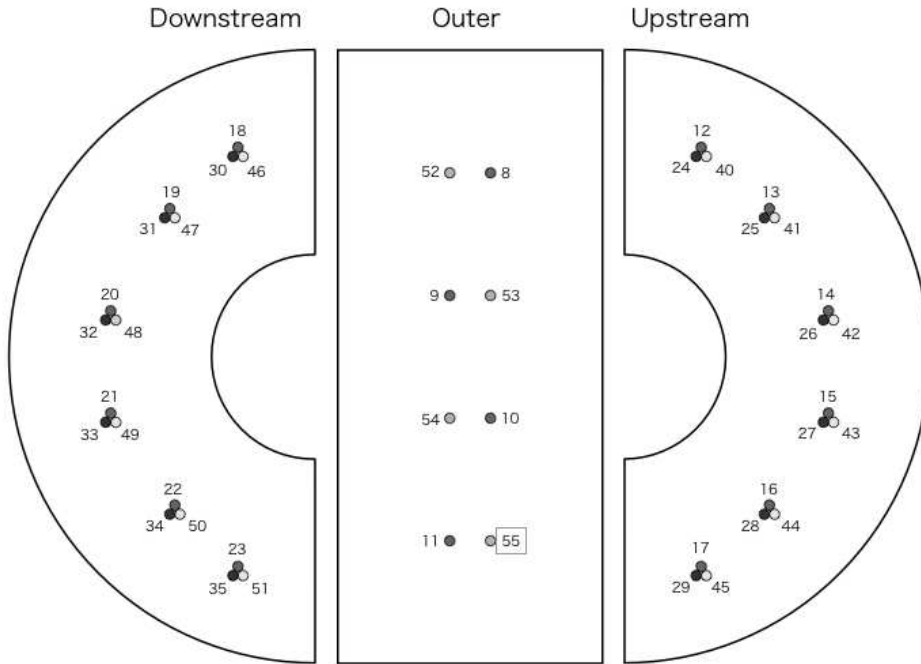


Figure 4.1: LEDs for calibration mounted inside the calorimeter in several positions. Different markers represent different attenuation factors.

pedestal. Combining the previous equations, we obtain:

$$\sigma^2 = g(q - q_0) + \sigma_0^2 \quad (4.3)$$

Neglecting the σ_0 and pulsing LEDs at different voltages, we obtain a good evaluation of g with a linear fit of σ^2 versus $q - q_0$. Figure 4.2 shows an example of the procedure for a photomultiplier.

4.1.2 α -sources

Five tungsten wires, with a diameter of $100 \mu\text{m}$, are mounted inside the calorimeter along the beam direction and fixed on the side faces. On each wire there are five ^{241}Am dots [76] bound with a gold foil wrapped and thermocompressed. Since they are immersed and in contact with liquid xenon, they were severely tested [77] and are protected by a thin gold layer ($\approx 1.5 \mu\text{m}$) (fig.4.3). The activity of each α -sources is ≈ 200 Bq. The activity of each α -source is ≈ 200 Bq and the mean life is long ($t_{1/2} = 430$ years) to ensure a stable intensity emission for many years.

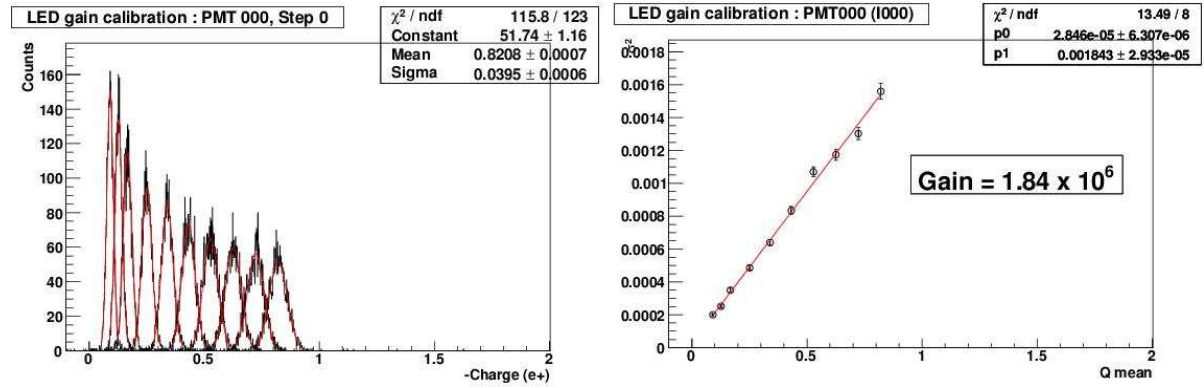
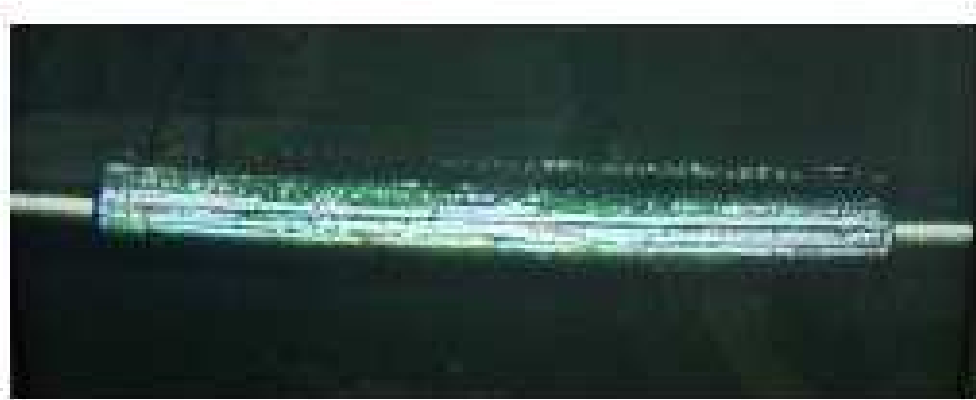


Figure 4.2: Example of a gain fit for a photomultiplier

Figure 4.3: ^{241}Am α -source fixed on wire.

Quantum efficiencies Because of the known energy (5.4 MeV), known positions and stable emission, α -sources are the most effective method to measure the PMTs QEs. Each photomultiplier is lightened by sources at different distances: comparing the expected and the real number of photoelectrons of an alpha event, and fitting the resulting plot we obtain an evaluation of photomultiplier quantum efficiency. The method requires a very good knowledge of the physical process inside the calorimeter for a correct α -events simulation, including reflections and absorptions on calorimeter walls and photomultiplier photocathode and inlet quartz window. We usually perform two different QE evaluations:

- **In gas xenon.** This is much simpler method because we can assume the absorption and Rayleigh scattering as negligible and set xenon refractive index equal to 1. Moreover the

average path of α -particle in gas xenon is ≈ 7 mm, so the energy is released far from the wire, the wire diameter can be neglected and the sources are reconstructed as spherical blobs. QE is however related to light emission spectra and temperature: the emission spectrum is the same as in liquid [60] [61] while temperature is maintained as much as possible near to the liquefaction one.

- **In liquid xenon.** In this case, it is crucial to use the correct values of absorption, Rayleigh scattering and refractive index. Moreover the α -particle average path in liquid xenon is ≈ 40 μm comparable with the wire diameter (100 μm): this creates a shadow effect (fig.4.4). As consequence the reconstructed position is not the real one and α -

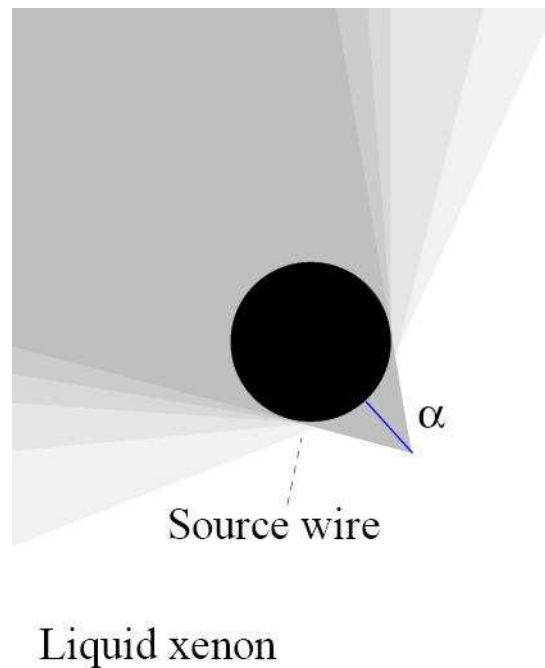


Figure 4.4: Alpha particle in liquid xenon: wire diameter (100 μm) is comparable with the α average path, this creates a shadow effect.

sources are reconstructed as rings. The radius of the rings depends on several physical factors (refraction, reflectivity, absorption, Rayleigh, etc...) which must be included in the simulation. It is difficult to measure at the same time all the necessary parameters but it is possible to obtain a satisfactory agreement between data and MC (see fig.4.5) by using ad-hoc parameter values.

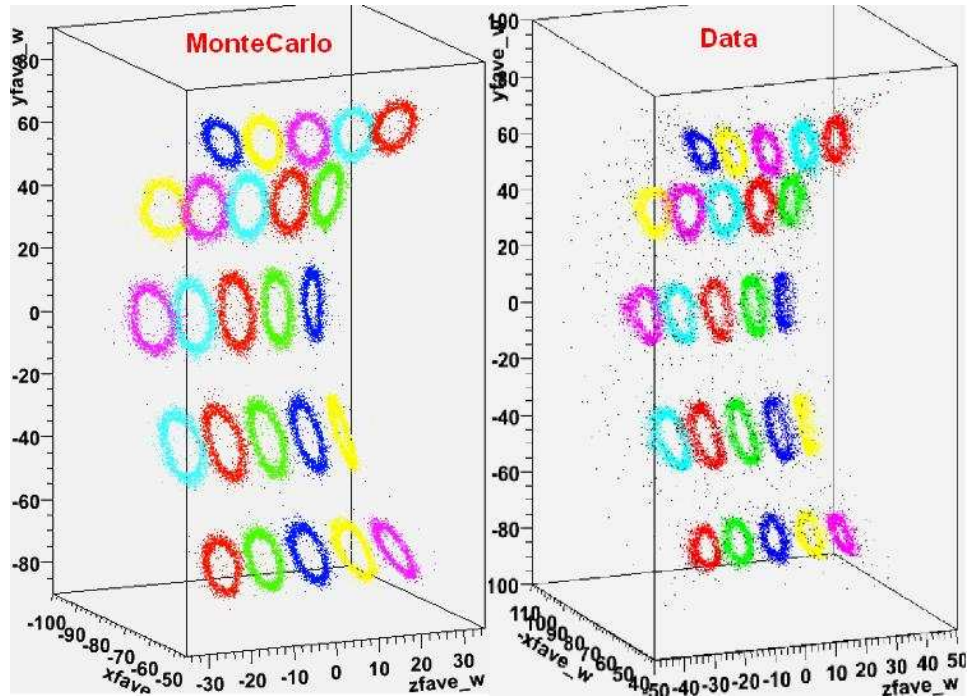


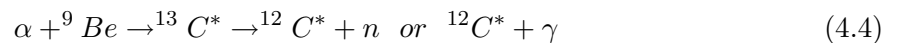
Figure 4.5: α -sources in liquid xenon: comparison between MC (left) and real data (right).

Figure 4.6 shows alpha data taken with the calorimeter half-filled with liquid Xenon: it is possible to note the different source reconstruction in gas and liquid phase. Figure 4.7 shows the correlation between gas and liquid measured QEs.

Absorption length In order to measure the absorption length of liquid xenon, we perform an exponential fit to the ratio of simulated and measured photoelectrons number as function of the distance to each photomultiplier (fig. 4.8). α -particles produce xenon scintillation mainly through excimer state de-excitation. This component of scintillation is barely influenced by electronegative impurities (see par. 3.1.1), α s cannot be used for measuring the level of all possible impurities.

4.2 Calibration 4.4 MeV γ s from AmBe source

A source of $^{241}\text{AmBe}$ produces 4.4 MeV γ rays from the ^{12}C deexcitation:



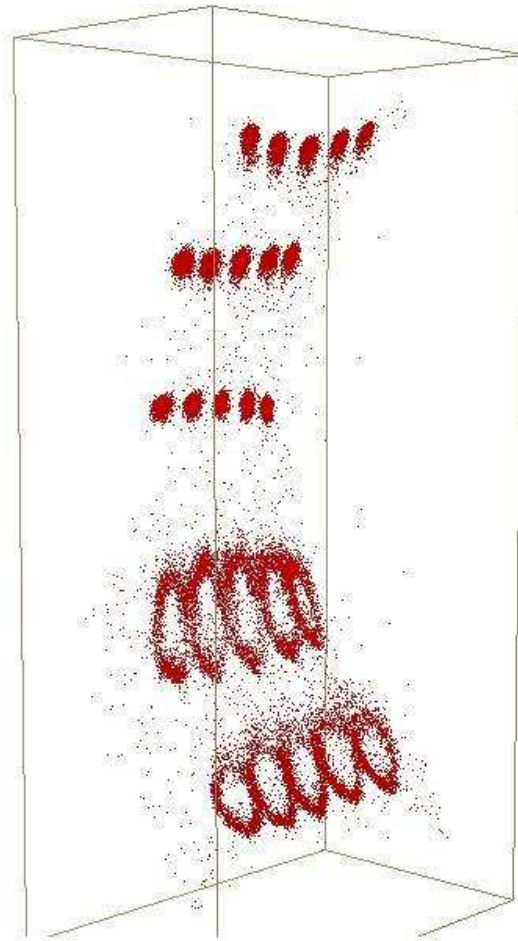


Figure 4.6: Reconstruction of the alpha source position with half filled calorimeter: the dots are sources in gas Xenon, the rings in liquid Xenon.

The used source has an activity of 50kBq and is placed in a polyethylene box ($50 \times 50 \times 50 \text{ cm}^3$) surrounded by a 5 cm-thick led block (fig. 4.9). During the calibration, it is moved to a measure box (fig.4.10) in front of the calorimeter using a dedicated air-compress line. The α -particles, from sources mounted inside the calorimeter, are the main background for this calibration, but it is possible to remove this background by using the different waveform τ between γ -signal and α -signal (see par.3.1.1). Figure 4.11 shows the total (black), α -background (red) and 4.4 MeV (blue) spectra. Despite the low energy of the γ s, this calibration is simple and fast and can be used in case of other γ -sources (see next paragraphs) are not available.

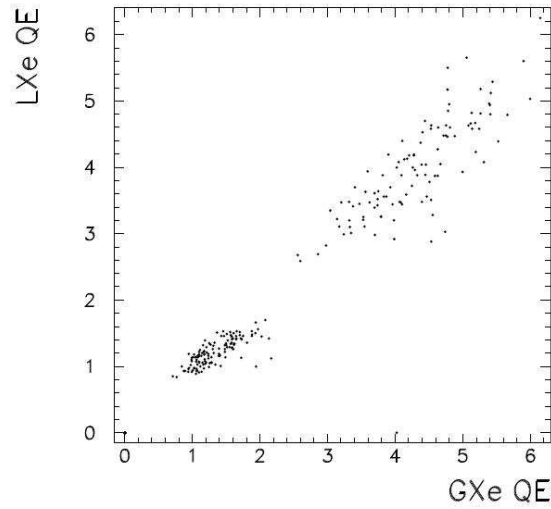


Figure 4.7: Correlation between the QE measured in liquid and gaseous xenon.

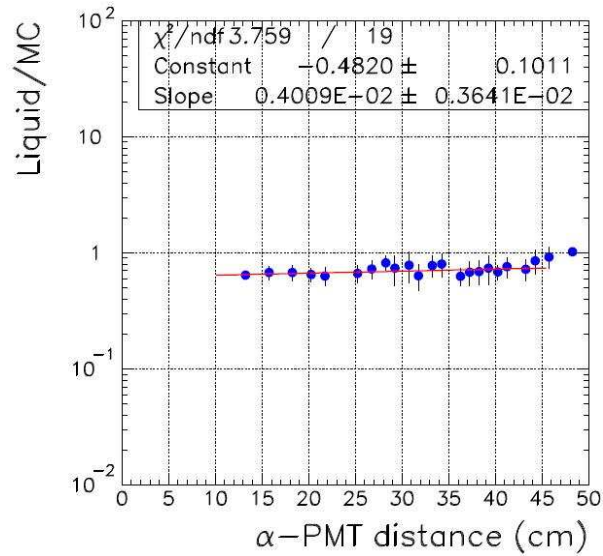


Figure 4.8: Ratio of simulated and real photoelectrons number (in LXe) versus the distance of each photomultiplier.

4.3 Calibration with Nickel 9 MeV line

Nickel has a large cross section for thermal neutron capture and single intense line emission of about 10 MeV. Table 4.1 shows the Nickel isotopic abundance and the energy of related

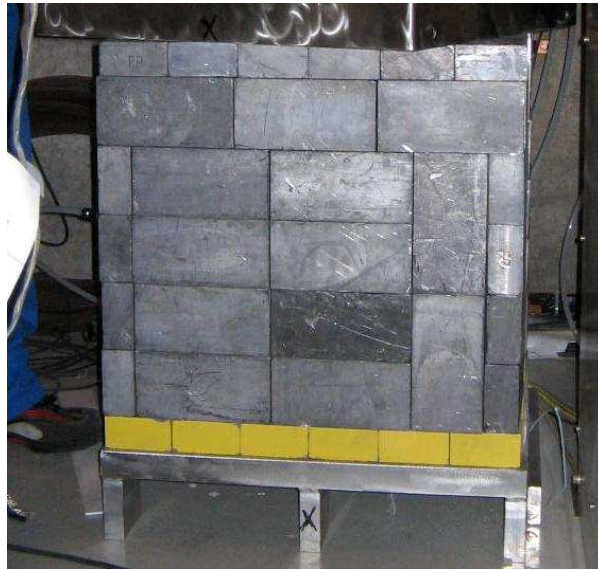


Figure 4.9: Picture of AmBe source repository.

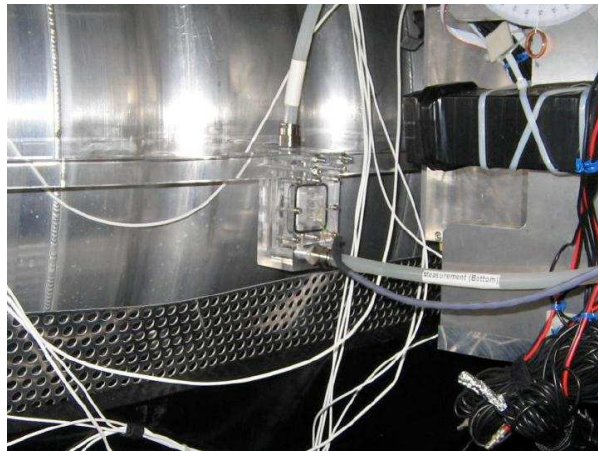
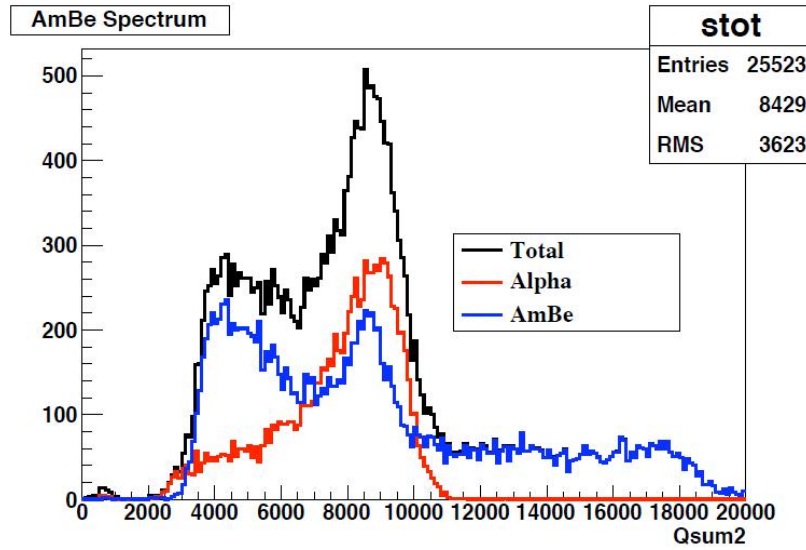


Figure 4.10: Picture of AmBe source measurement box.

emission lines. Figure 4.12 shows the Nickel line measured by a NaI detector. MEG uses a Thermo Scientific D 211 [78] neutron generator. The generator can produce a continuous or pulsed (maximum frequency 100 Hz) neutron flux. Table 4.2 shows the generator main properties. The generator is closed in a polyethylene box to moderate neutrons. In the face towards the calorimeter, polyethylene is mixed with thin nickel plates (fig.4.13).

Despite the γ s energy is only one sixth of a photon from a MEG event, there are two good

Figure 4.11: 4.4 MeV- γ spectrum (blue) after the α -subtraction (red) in photoelectron number.

Reaction	Abundance %	Capture σ [barn]	Emission peak [MeV]
$^{58}\text{Ni}(n, \gamma) \rightarrow ^{59}\text{Ni}^*$	67.88	4.4	9.000
$^{60}\text{Ni}(n, \gamma) \rightarrow ^{61}\text{Ni}^*$	26.23	2.6	7.820
$^{62}\text{Ni}(n, \gamma) \rightarrow ^{63}\text{Ni}^*$	3.66	15	6.838
$^{64}\text{Ni}(n, \gamma) \rightarrow ^{65}\text{Ni}^*$	1.08	1.52	6.098

Table 4.1: Nickel isotopic abundance and the energy of related emission lines.

Technical proprieties	
Generator type	D-D ($Q=3.27$ MeV, $E_n=2.45$ MeV) [79]
Neutrons per impulse	2.5×10^4
Neutrons per second	2.5×10^6 (@100 Hz)
Generator average life	>500 h
Frequency	10-100 Hz
Impulse width	$\approx 10\mu s$

Table 4.2: Neutron generator main proprieties.

reasons to perform this calibration:

- It is a fast calibration (daily repeatable) with γ -rays.
- The neutron generator gives a signal when it produces neutrons. Triggering on this

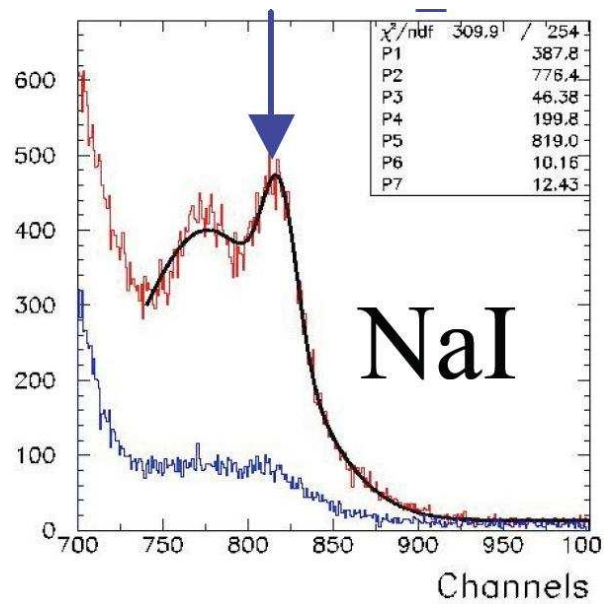


Figure 4.12: The 9 MeV γ -line with a NaI detector.



Figure 4.13: Neutron generator polyethylene box.

signal, it is possible to perform the calibration with beam, in the normal MEG data

taking conditions.

Figure 4.14 show the Nickel peak in the LXe with beam.

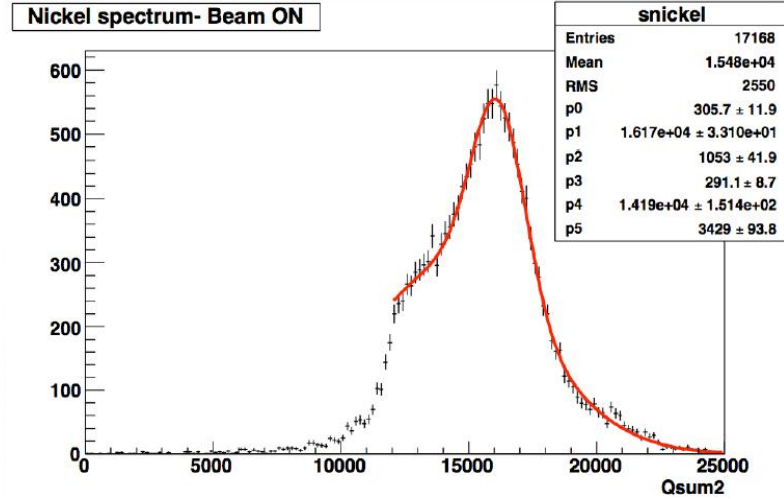


Figure 4.14: Nickel peak with beam.

4.4 Calibrations with Cockroft-Walton accelerator

Normally available radiative-ray sources produce photons with energies much below what expected for $\mu \rightarrow e + \gamma$ decay (52.8 MeV). In order to overcome the problem, a 1MeV Cockroft-Walton proton accelerator is used in combination with MEG apparatus (fig. 4.15). Table 4.3 summarizes the accelerator proprieties. In order to avoid any influence on the COBRA mag-

Proprieties	MEG CW
Energy [KeV]	100-1000
Energy ripple [KeV] (FWHM)	<0.5
Angular divergence [mRad x mRad] (FWHM)	5 x 5
Beam spot at 3m [cm x cm]	< 1, 1
Energy stability (FWHM)[%]	0.1
Current range [μA]	1-100
Current stability [%]	2

Table 4.3: Proprieties of MEG Cockroft-Walton accelerator.



Figure 4.15: Photo of Cockcroft-Walton accelerator.

net, it was placed in a separate zone downstream of the experimental area and the proton beam is sent to the apparatus center from the opposite direction of muon beam through an auxiliary beamline. Part of this beamline is extendable to allow inserting and removing it quickly (about 50 minutes for the whole insertion-extraction procedure). Both the accelerator and the auxiliary beamline are remotely controlled. The target used for calibrations is a lithium-tetraborate crystal ($\text{Li}_2\text{B}^4\text{O}_7$) which enables use of two different reactions simultaneously:

- ${}^7_3\text{Li}(\text{p},\gamma){}^8_4\text{Be}$. This reaction produces a 17.6 MeV gamma-line and is resonant at $T_p = 440$ keV with width $\Gamma \approx 12.5$ keV and cross section (on peak) $\sigma_p \approx 5$ mb [81]. The γ -energy is only three times smaller than the $\mu \rightarrow e + \gamma$ decay and it is very useful to monitor (purification, uniformity, etc...) and calibrate (energy) the calorimeter. Figure 4.16 shows the lithium peak measured with LXe calorimeter. The second peak comes from decay to the excited state of ${}^8\text{Be}$ instead of the ground state as shown in the reaction schema (fig. 4.17).
- ${}^{11}_5\text{B}(\text{p},\gamma){}^{12}_6\text{C}$. This reaction produces three γ -lines at 16.1, 11.7 and 4.4 MeV (fig.4.17):

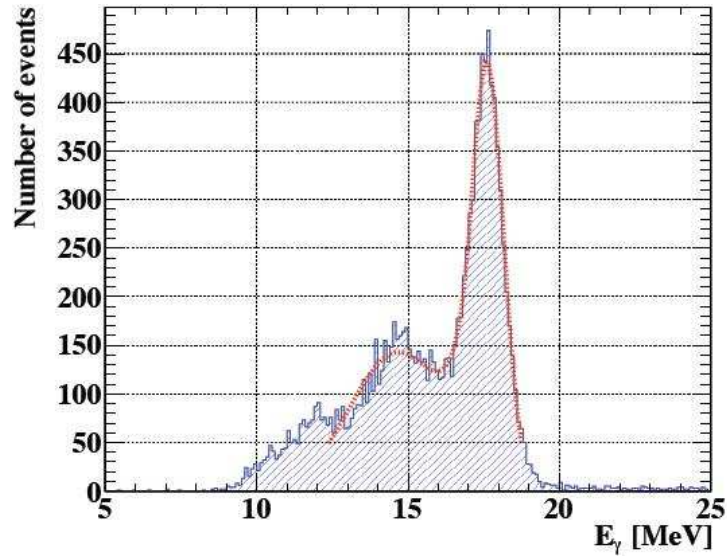


Figure 4.16: Lithium peak measured with LXe calorimeter.

the last two are emitted together with no angular correlation and can be simply used to calibrate relative timing between TC and calorimeter. This reaction is resonant at $T_p = 163$ keV with width $\Gamma \approx 5.3$ keV. Figure 4.18 shows the Boron peaks measured with LXe calorimeter.

More information about accelerator installation, setup and operation is given in [80].

4.5 Calibrations with Charge Exchange Process

ΠE5 beamline can transport negative pions which can be sent to a liquid hydrogen target to interact through the charge exchange reaction $\pi^- + p \rightarrow \pi^0 + n$. The produced neutral pions decay in two photons which can be used to calibrate the calorimeter with γ energies close to that of $\mu \rightarrow e + \gamma$ decay. An auxiliary NaI detector is used to trigger monochromatic 55 or 83 MeV photons. This method allows the determination of the energy, position and time resolutions of the LXe detector at described γ energies.

4.5.1 Kinematics of the reaction

Negative pions captured by protons at rest can give rise to two possible reactions:

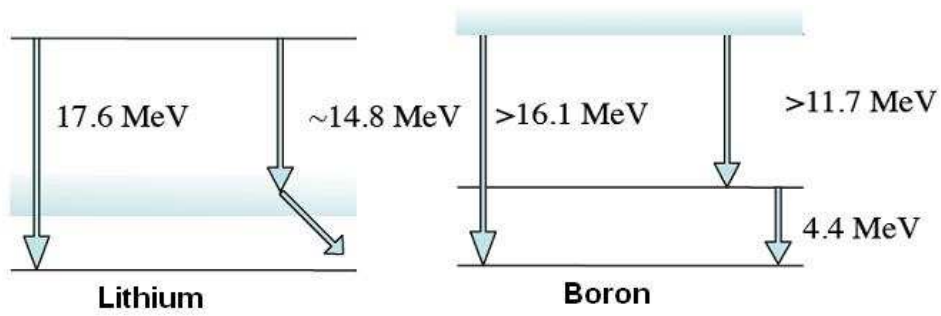


Figure 4.17: Reaction schema of ${}^7_3\text{Li}(p,\gamma){}_4^8\text{Be}$ and ${}^{11}_5\text{B}(p,\gamma){}_6^{12}\text{C}$.

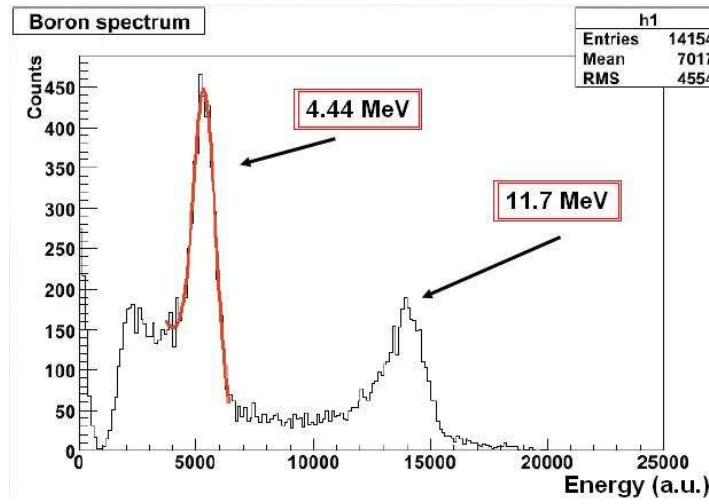


Figure 4.18: 11.6 and 4.44 MeV boron peaks measured with LXe calorimeter.

- The charge exchange reaction (CEX)



and

- The radiative capture reaction:



The ratio between the two processes was called "Panofsky ratio" because was originally measured by Panofsky [82]:

$$R = \frac{\Gamma(\pi^- + p \rightarrow \pi^0 + n)}{\Gamma(\pi^- + p \rightarrow \gamma + n)} = 1.533 \pm 0.021 \quad (4.7)$$

4.6 produces a high energy γ (129 MeV). On the contrary π^0 in 4.5 is produced with a pulse of 28 MeV/c so the energy of two γ s has a flat distribution between $54.9 \text{ MeV} < E_\gamma < 82.9 \text{ MeV}$. Moreover, because of the decay kinematics, the opening angle between the two photons has a strong correlation with the energy and we can write (as function of one of the two energies)(fig.4.19):

$$\theta_{\gamma\gamma} = \arccos \left(1 - \frac{m_{\pi^0}^2}{2E_\gamma(E_{\pi^0} - E_\gamma)} \right) \quad (4.8)$$

For this reason, selecting the γ s at fixed angle is equivalent to select their energy: in particular the energies for the 2 photons selected back to back are 54.9 and 82.9 MeV. It is important to note that a request of $\frac{\Delta E}{E} < 1\%$ corresponds to $\Delta\theta_{\gamma\gamma} < 5^\circ$.

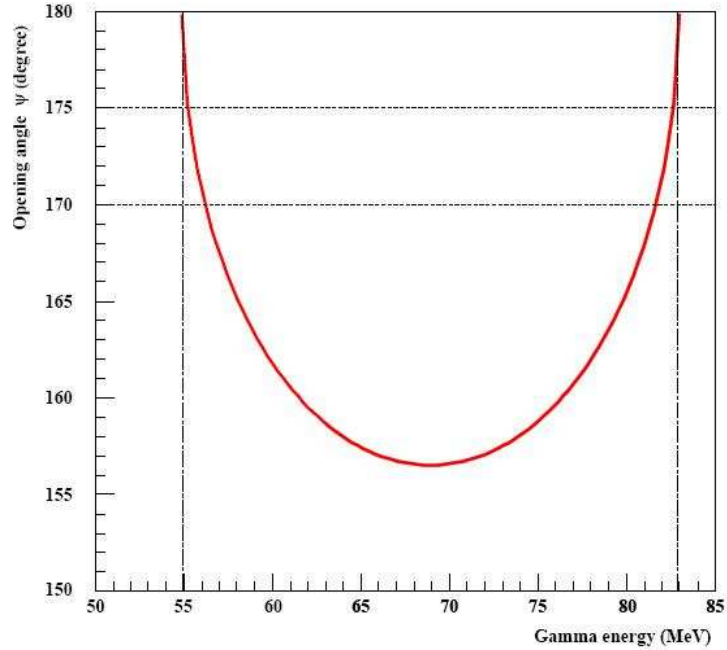


Figure 4.19: Correlation between energies and opening angle for the two γ s of π^0 decay.

4.5.2 Liquid hydrogen target

In order to have a reasonable CEX event rate, we used a target of liquid hydrogen. The target is basically a cylindrical cell of 50 mm diameter, 75 mm length, closed on the entrance side by a thin 135 μm mylar window (fig. 4.20). The cell is fixed at the end of a ≈ 2 m long pipe to place it at the center of COBRA magnet. Hydrogen is kept liquid by a liquid helium flow, which is controlled using two different valves and a pump in order to keep the liquefied volume stable. The working principle of the target is the following: a fixed amount of hydrogen is kept in a constant large volume (H_2 tank) constantly connected to the cell. During normal operation the cell is cooled down to 20 K and therefore fills up with liquid hydrogen, lowering the tank pressure. When the helium flux ends, hydrogen is left free to expand back to the tank volume. During normal operation the cell is filled with ≈ 150 cc of liquid hydrogen, at a temperature of approximately 20 K. This corresponds to 127 litres of hydrogen gas at standard temperature and pressure (the hydrogen expansion factor is ≈ 845). The buffer we use is made of 2 bottles of 47 liters each, for a total of 94 liters. This means that the amount of hydrogen to liquefy fills our buffer at 1.35 bar. The buffer is filled at the beginning with 2.5 bar of hydrogen, so that for an operating pressure of 1.2 bar the target cell is filled at 96% level (1.3 bar are liquefied, 1.2 bars make up the resulting pressure). Figure 4.21 shows a schematic view of the LH_2 target. The installation and setting of the target takes about 4 days.



Figure 4.20: Liquid hydrogen target cell.

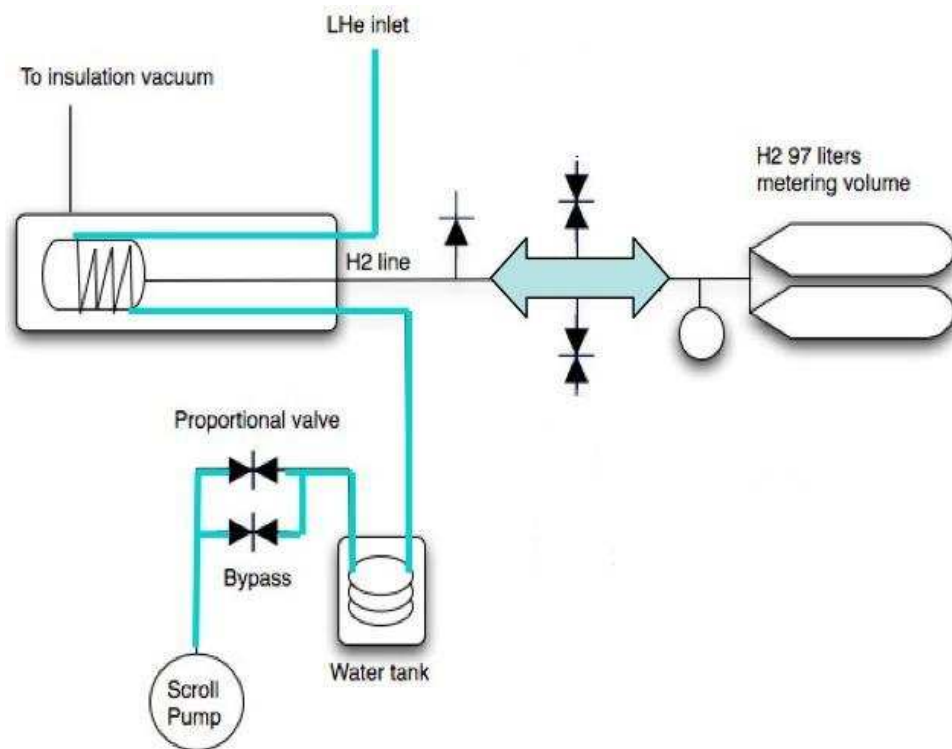


Figure 4.21: Schematic picture of liquid hydrogen target.

4.5.3 The NaI and preshower detector

The detector used to measure the second γ (at 180° with respect to the γ entering the calorimeter) is a grid of NaI crystals. It consists of nine crystals ($62.5 \times 62.5 \times 305 \text{ mm}^3$), each read out by an APD. In front of the NaI grid, two plastic scintillation counters ($70 \times 70 \times 7 \text{ mm}^3$), separated by a lead slab of 5 mm and read by two fine mesh photomultipliers, are used for timing purposes. The whole detector is mounted on a mechanical structure that allows to move it in different positions to scan several portions of the calorimeter along ϕ and z directions (fig. 4.22).



Figure 4.22: NaI detector mounted on a movable mechanical structure.

Chapter 5

Photon Reconstruction algorithms

This chapter shows the algorithms developed to measure the different photon kinematic characteristics. We conclude the chapter showing the procedure to reject cosmic rays and pileup events.

5.1 Reconstruction general remarks

The LXe critical energy is ≈ 14 MeV therefore a 52.8 MeV γ does not create a real "shower" but loses energy in few steps. Consequently shower development has large fluctuations. Fig. 5.1 shows the MC energy release for four different shower events. It is important to take in account this fact to measure the γ variables, in particular timing and position. The waveform of each PMT of the calorimeter is recorded: charge and timing are extracted from it (see next section). Gain and QE of each PMT are used to obtain the number of photoelectrons (N_{phe}) detected by that PMT and the number of photons (N_{pho}) hitting its photocathode:

$$N_{phe,i} = \frac{Q_i}{eG_i} \quad (5.1)$$

$$N_{pho,i} = \frac{N_{phe,i}}{QE_i} \quad (5.2)$$

where e is the electron charge, G_i and QE_i are the gain and the quantum efficiency of i -th photomultiplier. For γ reconstruction purposes, in addition to the general reference system (see section 2) we define a local coordinate system for liquid xenon calorimeter (u, v, w) :

$$u = z \quad (5.3)$$

$$v = R_0 \tan^{-1}\left(\frac{-y}{x}\right) \quad (5.4)$$

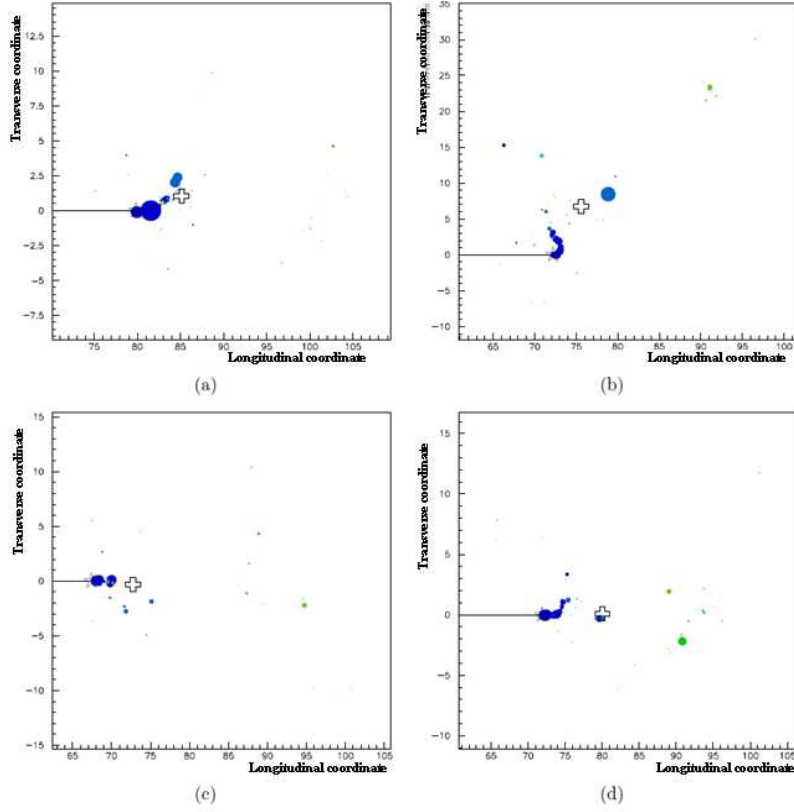


Figure 5.1: Examples of 52.8MeV- γ shower in the calorimeter . The star indicates the first interaction point; the cross is the weighted shower position; the spot dimensions are proportional to the released energy; the color corresponds to the shower time development (blu=before rosso=after).

$$w = \sqrt{x^2 + y^2} - R_0 \quad (5.5)$$

where $R_0 = 67.85$ cm is the radius of inner face, (u, v) are the projected position on the inner face, and w is the depth in the detector defined as the radial direction in cylindrical coordinates with the origin at the inner face surface (5.2).

Since at the edges of the calorimeter γ s are not totally contained, it can be useful to define a fiducial volume excluding the borders of the acceptance region as shown in figure 5.3:

$$|u| < 25\text{cm}, \quad |v| < 71\text{cm} \quad (5.6)$$

Only events in this region will be used to algorithm developments and final analysis.

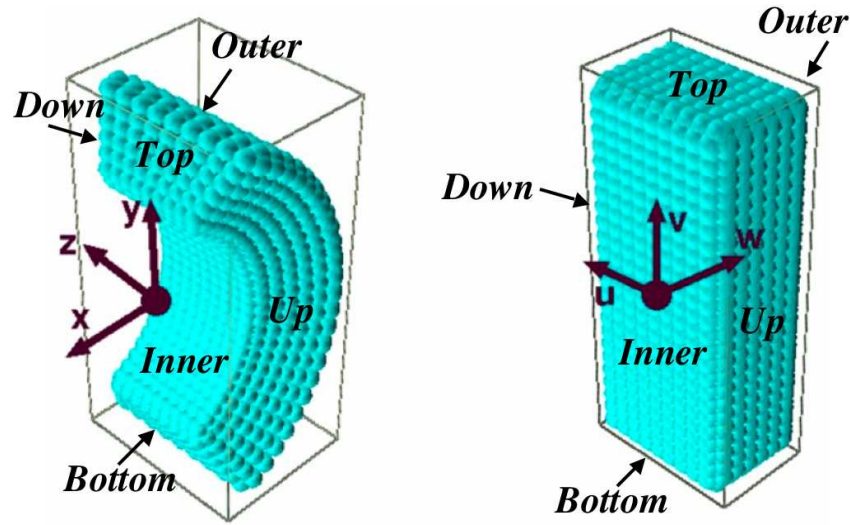


Figure 5.2: Definition of reference system (u,v,w) than (x,y,z) for calorimeter.

5.2 Photomultiplier waveform analysis

Figure 5.4 shows a typical photomultiplier DRS waveform. The baseline is estimated averaging the points before the waveform.

- **Charge.** The charge is extracted integrating the waveform. If a γ interacts close to a PMT, the waveform could saturate the electronics of that PMT(fig.5.5). In order to use the signal of that PMT, we measure the time the pulse is over a given threshold. Knowing the shape of the waveform of a γ -ray interaction event, we can estimate its charge.
- **Time.** Recorded waveforms are used to extract γ timing in two ways:
 1. a linear interpolation among different samplings is used to determine the timing at which preset threshold is passed (leading edge method);
 2. a constant fraction method is used: the timing at which the waveform reaches a fraction of the maximum amplitude is taken (30% for MEG).

5.3 Energy reconstruction

Because of the short radiation length, all the energy of gamma rays around 50 MeV is deposited inside the calorimeter and converted to scintillation light. For this reason, if absorption length is sufficiently long, the total number of collected photons is proportional to the energy regardless

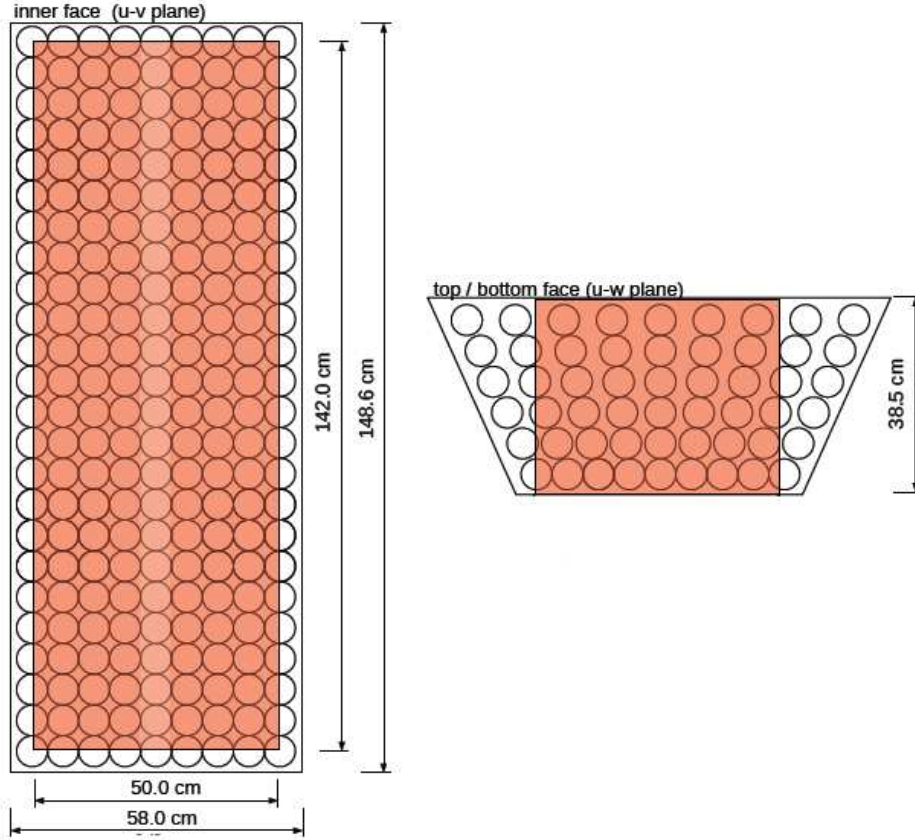


Figure 5.3: View of the fiducial volume (red region).

of the development of the shower. We can therefore use as good estimator of energy the following quantity:

$$N_{sum} = \sum_i w_i \times N_{pho,i} \quad (5.7)$$

where w_i are geometrical factors taking into account the local fraction of calorimeter surface covered by PMT's. The PMT coverage is different depending on calorimeter face (fig.5.6).

However when the first conversion point is very close (<2 cm) to a PMT, N_{sum} becomes very sensitive to the event position because it depends very much on the position of the conversion point (in front of a PMT or between two PMTs). In order to consider this effect, we separate "normal" ($w > 2$ cm) from "shallow" ($w < 2$ cm) events. The energy of these latter is corrected depending of the solid angle subtended by each PMT from conversion point. The correction function is extracted from data (γ s from CW or CEX) [86]. Another algorithm used to compute

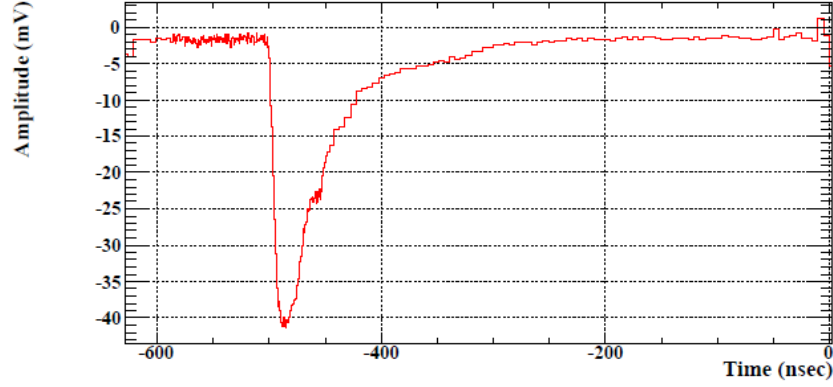


Figure 5.4: Example of PMT waveform.

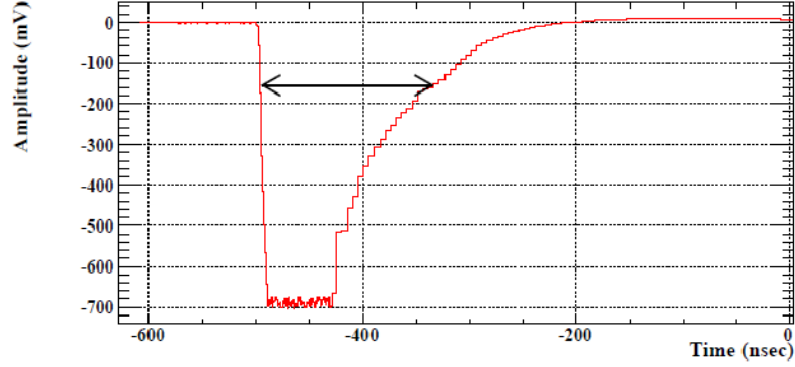


Figure 5.5: Example of PMT saturated waveform.

energy is the "Linear fit" (LF) [87]. We can define the event energy as linear sum of the PMTs charges plus a constant:

$$E = a_0 + \sum_i a_i Q_i \quad (5.8)$$

The coefficients a_i are obtained using a MC simulation by minimizing the following expression:

$$\chi^2 = \langle (E_{LF} - E_r)^2 \rangle \quad (5.9)$$

where E_r is the "true energy of event". The result of the minimization procedure is analytical:

$$a = \langle E_r \rangle - \left\langle \sum_j c_j Q_j \right\rangle \quad (5.10)$$

$$a_i = \frac{M^{-1}}{N-1} \left[\sum_{MCevents} E_r Q_i - \frac{1}{N} \sum_{MCevents} E_r \sum_{MCevents} Q_i \right] \quad (5.11)$$

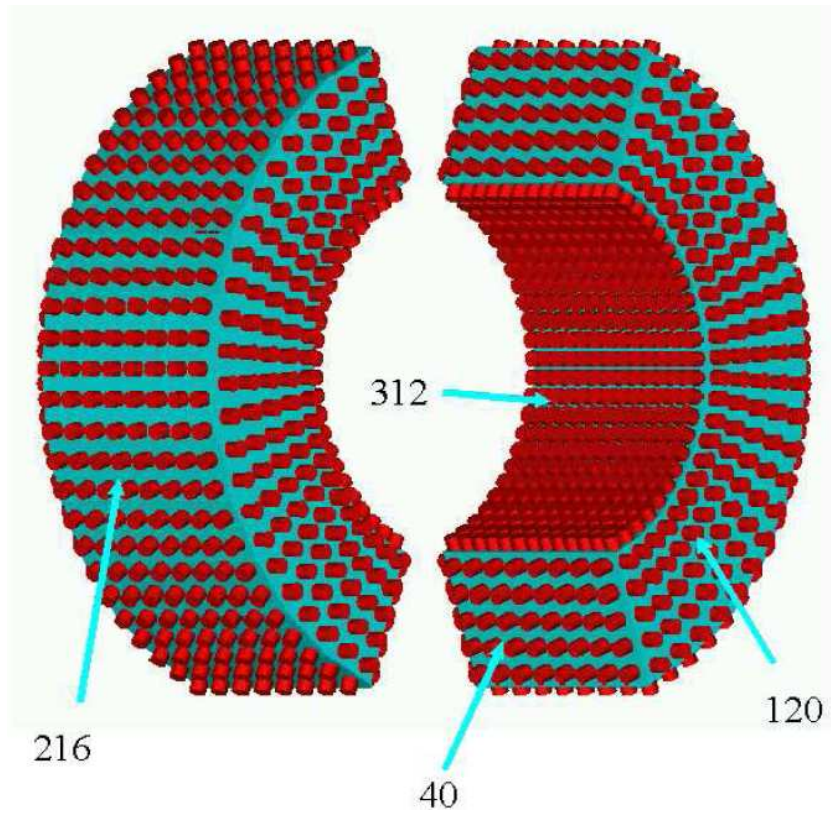


Figure 5.6: PMT distribution in the calorimeter: different faces have different PMT coverage.

with M covariance matrix computed by MC simulation:

$$M_{kl} \cong \langle (Q_k - \langle Q_k \rangle) (Q_l - \langle Q_l \rangle) \rangle \quad (5.12)$$

LF performances obviously depends on how well MC simulation can reproduce real data.

5.4 Position reconstruction

As shown in the section 5.1, a 52.8 MeV γ has large fluctuations in the shower shape: it releases its energy in few steps (≈ 3) so it is subject to large fluctuations. For this reason the purpose of position reconstruction is to estimate the position of first conversion point instead of the center of the shower (influenced by the fluctuations). The first interaction point, because of the short radiation length, is almost always very close to the entrance face. Usage of inner face PMTs is the best way to estimate the first conversion point.

We use three methods to do it:

- **A weighted mean of light deposit.** This analytical method is the simplest and the fastest: the position of each PMT is weighted with the corresponding collected light.

$$\begin{aligned}\bar{x} &= \frac{\sum_i N_{pho,i} x_i}{\sum_i Q_i} \\ \bar{y} &= \frac{\sum_i N_{pho,i} y_i}{\sum_i Q_i} \\ \bar{z} &= \frac{\sum_i N_{pho,i} z_i}{\sum_i Q_i}\end{aligned}\tag{5.13}$$

with (x_i, y_i, z_i) and Q_i , the coordinates and the charge of the i -th PMT (all PMTS) respectively. The interaction point estimated in this way is biased towards the detector center. For this reason a correcting factor must be applied to evaluate the photon position correctly.

- **A fit to PMT amplitudes.** The light collected by a PMT is related to the solid angle $\Omega(x_i, y_i, z_i)$ from which it is seen at a certain conversion point. The three coordinates of gamma ray interaction $(x_\gamma, y_\gamma, z_\gamma)$ can be calculated by minimizing:

$$\chi^2 = \sum_i \frac{N_{pho,i} - c \times \Omega_i(x_\gamma, y_\gamma, z_\gamma)}{\sigma_{pho,i}}\tag{5.14}$$

where c is a constant factor and $\sigma_{pho,i}(N_{pho,i})$ is statistical uncertainty of the PMT's charge calculated by

$$\sigma_{pho,i} = \sqrt{\frac{N_{phe,i}}{QE_i}}\tag{5.15}$$

This method is limited by the assumption that the scintillation light source be point-like. To minimize this effect, only a small group of PMTS in restricted region of the inner face are used. We perform a first fit using a handful of PMTs (≈ 45) around the one which has seen more light. The procedure is repeated with a smaller PMTs group (≈ 15) around the point obtained from the previous fit. Figure 5.7 shows an example of this procedure. Because the shower usually develops in the original γ -direction, this reconstructed position has a bias in u and w coordinates; MC corrections are applied to avoid this problem.

- **Linear fit method.** This procedure is similar to that described in the previous section

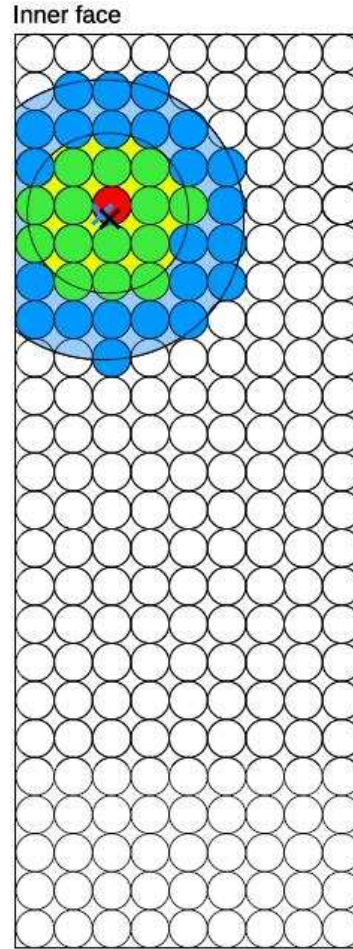


Figure 5.7: An example of the position fitting procedure. The blue cross is the estimate from the first fit around the PMT with the maximum measured charge using PMTs inside a 3.5-PMT radius circle. The black cross is the estimate of second fit around the first fit outcome using PMTs inside a 2-PMT radius circle.

for energy. We define:

$$\begin{aligned}
 x &= b_0 + \sum_i b_i \frac{Q_i}{Q_{tot}} \\
 y &= c_0 + \sum_i c_i \frac{Q_i}{Q_{tot}} \\
 z &= d_0 + \sum_i d_i \frac{Q_i}{Q_{tot}}
 \end{aligned} \tag{5.16}$$

Minimizing the following expressions we can obtain the coefficients b_i, c_i, d_i :

$$\begin{aligned}\chi^2 &= \sum_{MCevents} (x - x_r)^2 \\ \chi^2 &= \sum_{MCevents} (y - y_r)^2 \\ \chi^2 &= \sum_{MCevents} (z - z_r)^2\end{aligned}\tag{5.17}$$

where x_r, y_r, z_r are the “true” spatial coordinates of each MC event.

5.5 Time reconstruction

We define the time of i-th pmt as:

$$T_i = t_i - t^{scint} - t^{delay} - t^{tt} - \frac{d_i}{v_{LXe}} - \frac{L}{c}\tag{5.18}$$

where

- t_i is the time extracted from the event waveform. If the leading edge method is used (see section 5.1), we need to correct the time with a timewalk factor.
- t^{scint} is the average arrival time of the first scintillation photon. In case of N_{phe} scintillation photons, from exponential distribution we can write:

$$t^{scint} = \tau \log \frac{N_{phe}}{N_{phe} - 1}\tag{5.19}$$

where τ is de-excitation time of xenon.

- t^{delay} is the delay due to cables, electronics, etc... It is estimated by using the time difference distribution of each PMT with respect to the tagging detector (NaI preshower detector) in CEX runs.
- t^{tt} is the transit time of the photomultiplier. We incorporate it in t^{delay} .
- $\frac{d_i}{v_{LXe}}$ is the time from the interaction point to the PMT. d_i is the minimum distance and v_{LXe} is the light velocity inside liquid xenon. It is important to note that, in general, d_i is the distance from the interaction point and the nearest edge of the PMT photocathode. This is not true for events in front of the PMT: in this case we take the perpendicular line from the interaction point to the PMT photocathode (see fig.5.8).

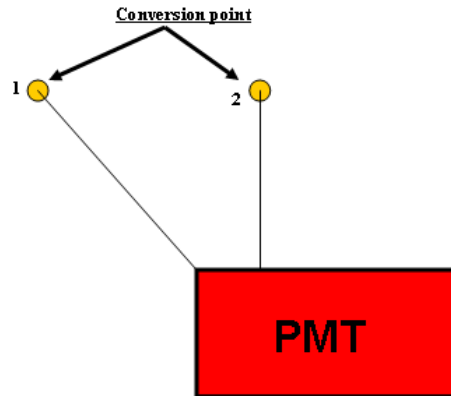


Figure 5.8: Minimum distance from conversion point to PMT: 1) generic event; 2) event in front of PMT photocathode.

- $\frac{L}{c}$ is the time from the emission point on the MEG target to the conversion point inside the calorimeter. L is the distance and c is the light velocity in vacuum. The emission point on the target is extracted from the positron track.

Figure 5.9 shows a schematic view of the different contributions.

We developed two different algorithms to compute the time of one event in the xenon calorimeter:

- XECPMTWeightedAverageTime.
- XETimeFit.

5.5.1 XECPMTWeightedAverageTime

XECPMTWeightedAverageTime is an analytical algorithm: each contribution to T_i is separately estimated and included into the equation 5.18. For t_i we use the leading edge time with a threshold of 5 mV, far from noise fluctuations (DRS baseline sigma is ≈ 1 mV). The timewalk is corrected with a factor estimated by CW Lithium events by fitting the following expression:

$$t_i = t_i^{ld} - \frac{W}{\sqrt{Q_i}} \quad (5.20)$$

where t_i^{ld} is the leading edge time, W is the correction factor we are looking for and Q_i is the charge of i -th PMT. Fig.5.10 shows the correction factor distribution for all PMTs and inner

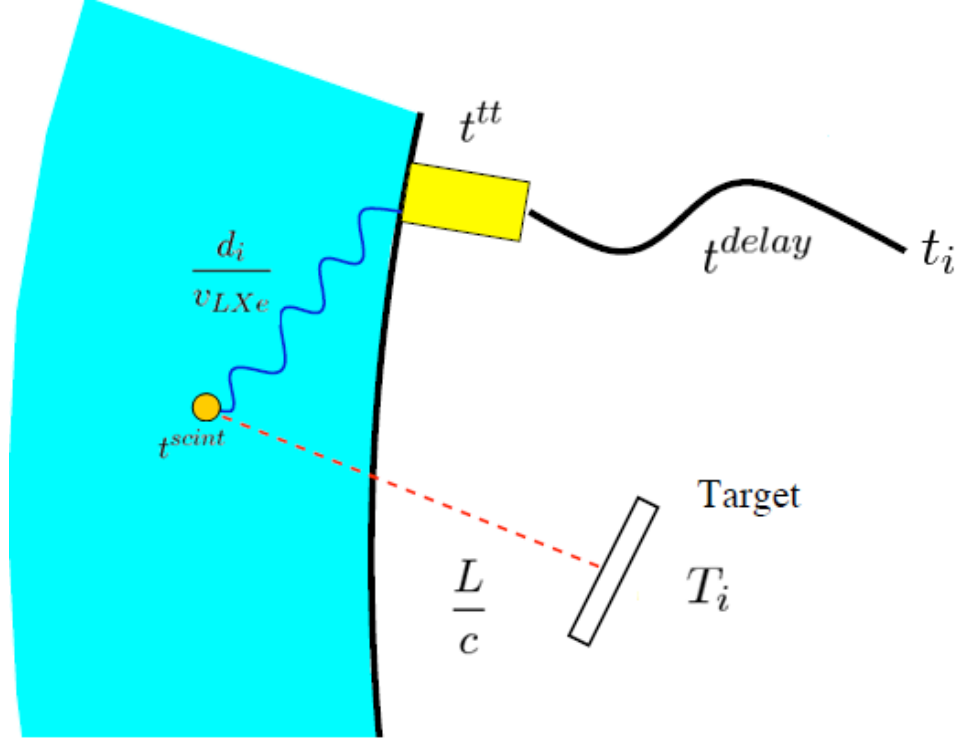


Figure 5.9: Schematic view of different contributions from equation 5.18.

face PMTs alone. The presence of large tails in the W distribution of all PMTs is due to low energy of Lithium γ : less scintillation photons reach the non-inner faces and the W estimate is less accurate. The time of the event is the average of the time of each PMT, weighted with its respective sigma:

$$\sigma_i^2 = \frac{\sigma_{tt}^2}{N_{phe,i}} + \quad (5.21)$$

$$\frac{\tau^2}{N_{phe,i}^2} + \quad (5.22)$$

$$\left[\frac{1}{v_{LXe} d_i} \left(w + r_0 + \cos\left(\frac{v}{r_0}\right) x_{pmt-i} - \sin\left(\frac{v}{r_0}\right) y_{pmt-i} \right) + \frac{1}{cL} (w + r_0) \right]^2 \sigma_W^2 + \quad (5.23)$$

$$\left[\frac{1}{v_{LXe}} (u - z_{pmt-i}) + \left(\frac{1}{cL} u \right) \right]^2 \sigma_u^2 + \quad (5.24)$$

$$\left[\frac{1}{v_{LXe}} (w + r_0) \left(\cos\left(\frac{v}{r_0}\right) y_{pmt-i} + \sin\left(\frac{v}{r_0}\right) x_{pmt-i} \right) \right]^2 \sigma_v^2 \quad (5.25)$$

where

- 5.21 is the fluctuation related to the transit time: σ_{tt} is provided by HAMAMATSU (≈ 800 ps) and \sqrt{N} arises from the Gaussian distribution of the transit time of electrons

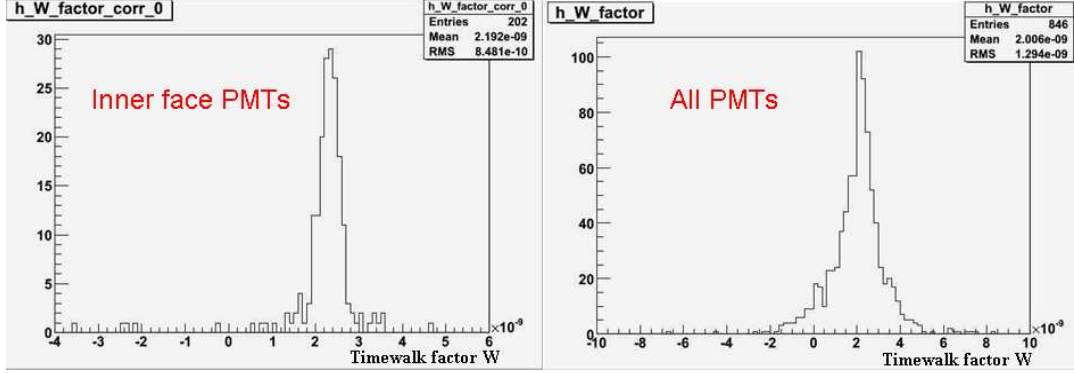


Figure 5.10: Timewalk correction factor distribution: left, inner face PMTs alone; right, all PMTs.

along the dynode chain.

- 5.22 is the fluctuation related to scintillation time ¹.
- 5.23, 5.24, 5.25 are the fluctuations related to the term $(\frac{d_i}{v_{LXe}} - \frac{L}{c})$ computed by using the method of the partial derivatives: u, v, w are the coordinates of interaction point, $x_{pmt-i}, y_{pmt-i}, z_{pmt-i}$ are the coordinates of the PMT center, r_0 is the radius of calorimeter, $\sigma_w, \sigma_u, \sigma_v$ are the spatial resolutions in u, v, w .
- Since the fluctuation related to t^{delay} is estimated $\approx 10\text{ps}$ (σ_{DRS}), fix for all PMTs, we could ignore it.

We reject PMTs seeing less than 80 photoelectrons. v_{LXe} is estimated by fitting time as function of the distance from conversion point to each PMT. To eliminate effects due to diffusion light, we

¹The fluctuation on the emission time of a single scintillation photon with such an exponential distribution is:

$$\sigma_t^2 = \langle t^2 \rangle - \langle t \rangle^2 = \tau^2 \quad (5.26)$$

In case of emission of N scintillation photons the scintillation timing is determined by the earliest emitted photon, whose distribution is given by:

$$P(t_{min})dt_{min} \propto e^{-\frac{Nt_{min}}{\tau}} dt_{min} \quad (5.27)$$

where t_{min} is the emission time of the earliest photon. Hence the fluctuation in case of N emitted photons scales with N and not with \sqrt{N} :

$$\sigma_{t_{min}}^2 = \langle t^2 \rangle - \langle t \rangle^2 = \frac{\tau^2}{N^2} \quad (5.28)$$

use only PMTs with angles between the photocathode normal and the reconstructed interaction point less than 45° . In order to obtain the event time, two further corrections are applied:

1. The distribution of the PMT time as function of the distance from conversion point to PMT shows a non-flat behavior for events close to PMT ($<5\text{cm}$). This effect could be explained as a non correct position reconstruction for events close to PMTs. We correct it using a different light speed inside the liquid xenon for events with distance less than 5 cm.
2. PMTs with large angles with respect to the conversion point collect a lot of diffused light photons, and could give non a correct estimate of the time. In order to avoid this problem, we reject pmts with a time too far (more than 2σ) from the mean. Figure 5.11 shows an example of PMT time distribution for an event.

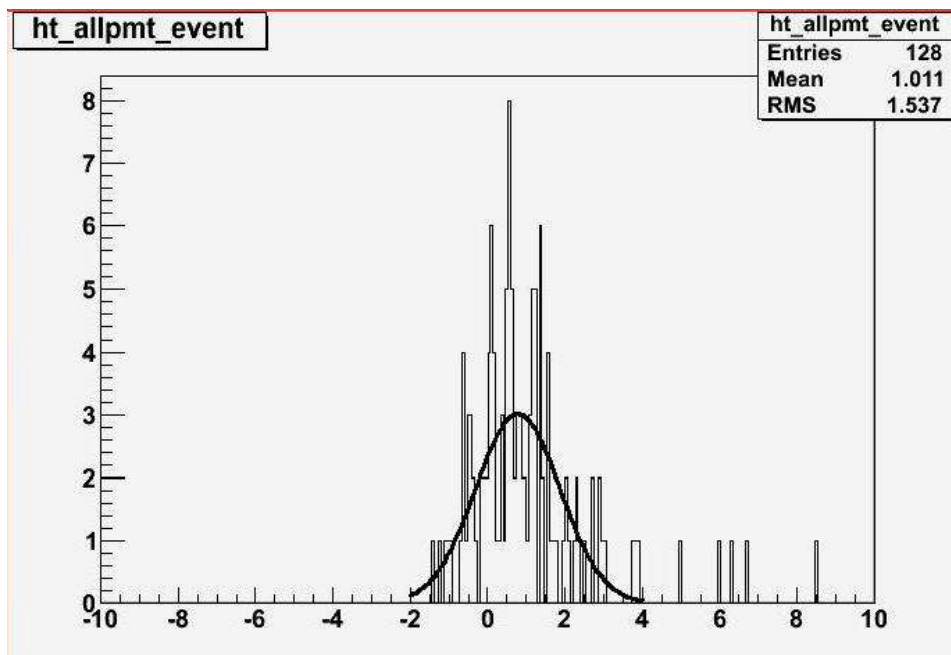


Figure 5.11: An example of PMT time distribution: PMTs with time more than 2σ from the mean are rejected.

5.5.2 XECTimeFit

XECTimeFit differs from XECPMTWeightedAverageTime because:

- It uses a t_i evaluated by using a constant fraction (software) discriminator;
- It uses PMTs seeing more than 50 photoelectrons (instead of 80);
- It introduces an empirical function to model the dependence of the time from indirect light;
- It computes the event time T by minimizing the following expression:

$$\chi_{time}^2 = \sum_i \frac{(t_{hit,i} - T)^2}{\sigma_{t,i}(N_{phe})^2} \quad (5.29)$$

where $t_{hit,i}$ is the PMT constant fraction time corrected for the t^{delay} , $\frac{d_i}{v_{LXe}}$ and indirect light, $\sigma_{t,i}(N_{phe})$ is the time resolution as a function of $\frac{1}{\sqrt{N_{phe}}}$.

More informations about this algorithm is given in [86].

5.6 Pileup rejection

We define as pileup event an accidental coincidence between two γ s from any possible source. Assuming a muon rate stop $\approx 3 \times 10^7 \frac{\mu}{s}$, around 9% of γ events have a pileup during the decay time of scintillation light (MC simulation). Two procedures to recognizing and rejecting pile-up events were developed:

- **Time separation.** We identify pileup events using χ^2/NDF of time reconstruction fit which it is larger in case of pileup. Figure 5.12 shows the χ^2/NDF distribution of data (xenon alone, events reconstructed in fiducial volume with $E_{gamma,i} 46$ MeV) and MC (signal events): we fix a cut to $\chi^2/NDF < 3$ because in the simulation less than 2% of signal events have a $\chi^2/NDF > 3$.
- **Spatial separation.** A search for peaks on the light distribution of inner face PMTs is performed. In this way, we can find the position of each gamma ray and identify also pileup events with the two photons entering the calorimeter almost at the same time (for these events the previous procedure is not efficient). The efficiency of this procedure depends on the threshold set to search peaks for and is noise limited.

If the pileup event has only time separation, it is rejected. If spatial separation is present, we try to recover the event. We exclude the PMTs around the pileup γ and, using a table with the average outputs of each PMT for each position, we estimate the energy by fitting the remaining

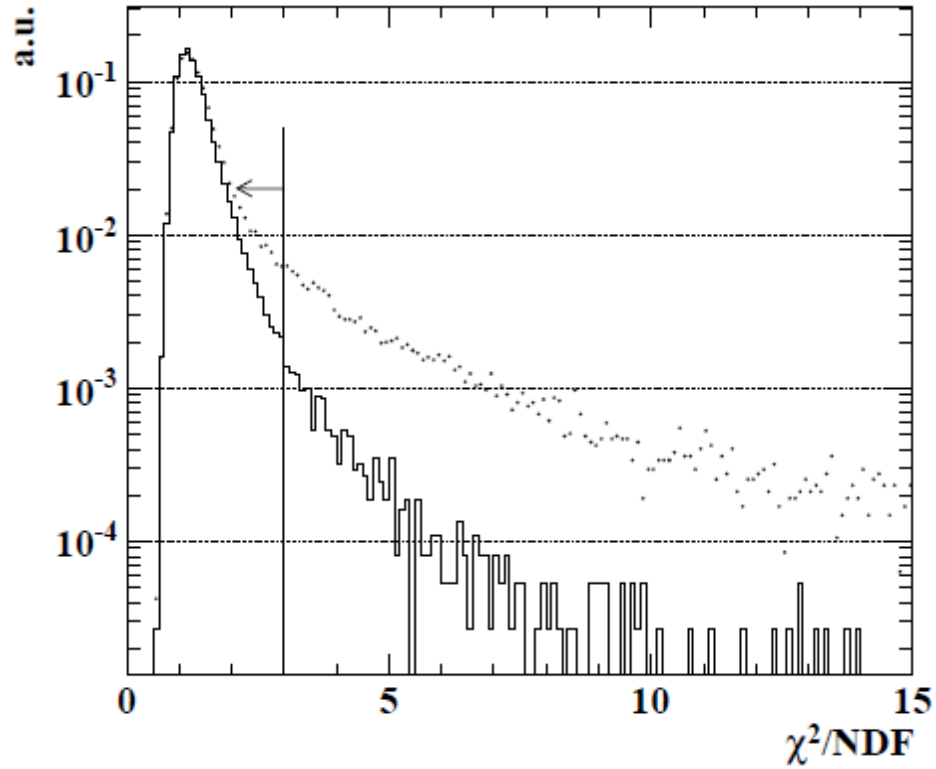


Figure 5.12: Distribution of normalized χ^2/NDF of the time fitting: distribution of xenon alone data reconstructed in fiducial volume with $E_{\gamma} \approx 46$ MeV (dotted) and MC signal event simulation (continue).

ones. The table is computed using CW data. With the same table, we compute the expected outputs of PMTs involved in the pileup and replace their charge values with the expectation. Subsequently the usual energy reconstruction is performed. However, if the pileup γ energy is larger than 10% of the main γ energy (≈ 5 MeV for signal events), the event is rejected because it is not possible to estimate correctly the pileup contribution. Figure 5.13 shows the scintillation light distribution for one event into the calorimeter before and after a pileup elimination.

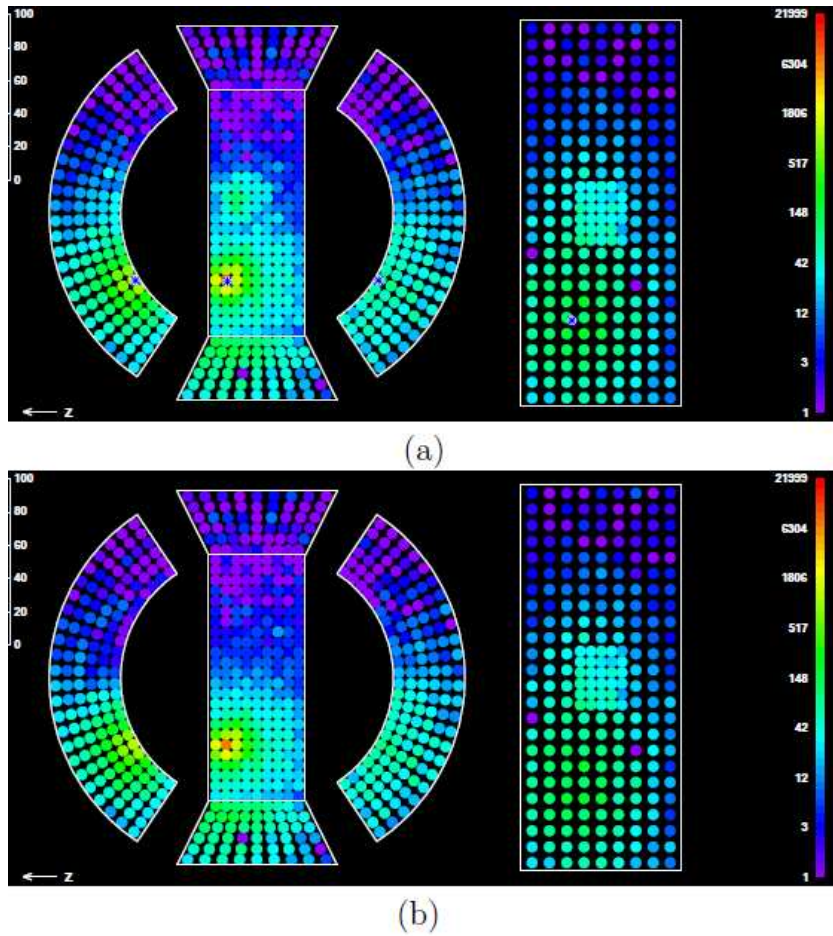


Figure 5.13: Scintillation light distribution into the calorimeter before (a) and after (b) a pileup elimination.

5.7 Cosmic ray rejection

Cosmic rays (CR) hit the calorimeter. Figure 5.14 shows a spectrum of calorimeter alone without beam. The rate of low energy backgrounds from cosmic is much lower than that from radiative decay or positron annihilation in flight, so pileup contribution from these events is very unlikely. The situation is different in a narrow energy around the signal: event rate of cosmic rays is comparable with RD or AIF so it is necessary reject them. We could reject them using the event topology: since the cosmic rays deposit large quantity of energy in the deep region of the detector, we require a cut $\frac{N_{Inner}^{pho}}{N_{pho}^{Outer}} > 0.3$. Figure 5.15 shows the $\frac{N_{Inner}^{pho}}{N_{pho}^{Outer}}$ distribution for CR (calorimeter data alone without beam), gamma ray events from beam (calorimeter data

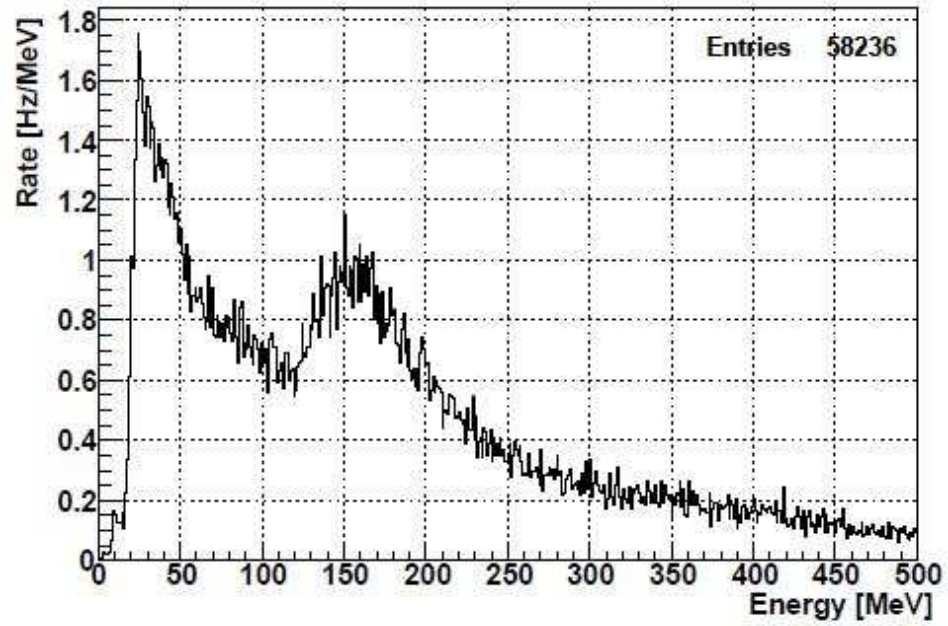


Figure 5.14: Cosmic ray spectrum in the calorimeter: rate in ordinate.

alone with beam) and simulated signal events from MC. The cut reduces the cosmic ray rate in the region $51 < E_\gamma < 55$ MeV to 0.35 Hz (5 Hz without cut) to be compared with 20 Hz γ rate from the beam. The inefficiency due to this cut is 1.1 %.

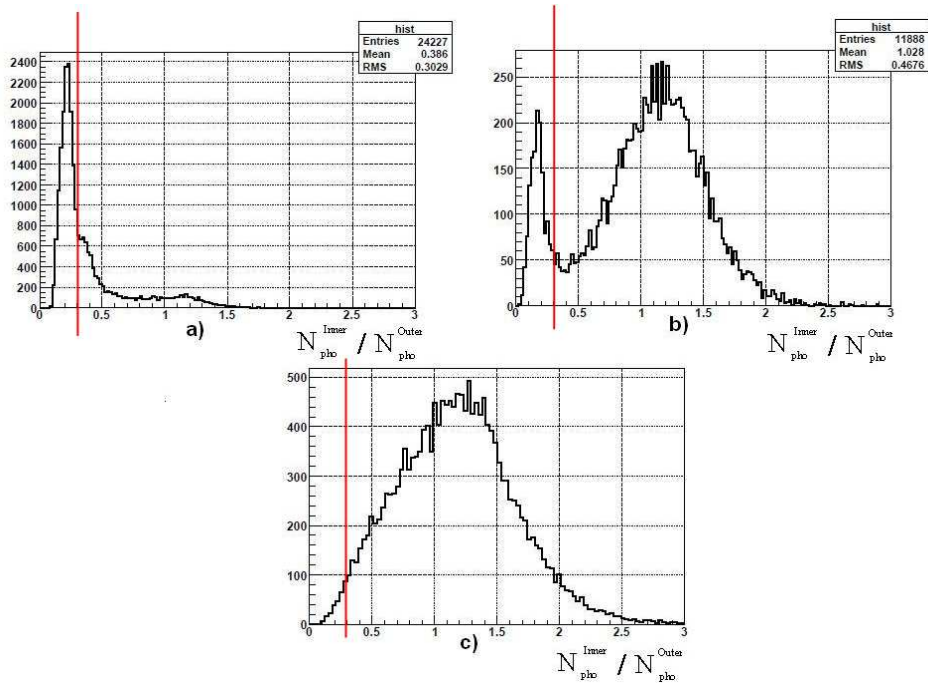


Figure 5.15: $\frac{N_{pho}^{Inner}}{N_{pho}^{Outer}}$ distribution: a) calorimeter alone without beam (cosmic rays); b) calorimeter alone with beam (cosmic rays and γ from beam); c) simulated signal from MC. The red line is the cosmic reject cut.

Chapter 6

Performances of the LXe Calorimeter in 2008 MEG run

2008 run was the first physics run of the MEG experiment; it started on September 12 and ended on December 22. The calorimeter was filled with liquid xenon in May and it remained operational until the end of the data taking. Xenon was purified in liquid and gas phases and was constantly monitored: two charge exchange runs (at the start and end of data taking period) and, three times per week, a full calorimeter calibration with LED, α and Cockroft-Walton data were performed. In this chapter we show the calorimeter performances and resolutions in energy, time and position. We first show the calibration of the PMTs parameters (gains and QE) and related problems. We then show the uniformity of the calorimeter, monitoring of purification and light yield and the consequent corrections that need to be applied to the energy scale. In conclusion we discuss each resolution and present the calorimeter efficiency.

6.1 Calibrations of PMTs characteristics during 2008 run

During the 2008 run we measured gain and QE of each photomultiplier once a day using both DRS and trigger data. In this section we discuss the encountered problems.

6.1.1 Gain shift

An intensive low energy background influences the gain of PMTs. The MEG experiment works in these conditions because of a lot of low energy γ s from several sources (radiative muon decay, Xenon neutron capture, etc...). Despite the tests and the modification (see section 3.3.1) done

before the installation, some PMTs ($\approx 15\text{-}20\%$) show a gain variation when operated with normal beam (low energy background) with respect to the no-beam situation (no low energy background). This implies a slight increase ($\approx 2\text{-}4\%$) of the average gain in beam conditions. Figure 6.1 shows the average gains, using trigger data, related to the two different conditions:

1. Gains in the green zone are computed using led data acquired with the beam shutter closed (beam off);
2. Gains in the red zone are computed using led data taken with the beam shutter open, in the normal experiment beam condition ($\approx 3 \times 10^7$ muons/sec) (beam on).

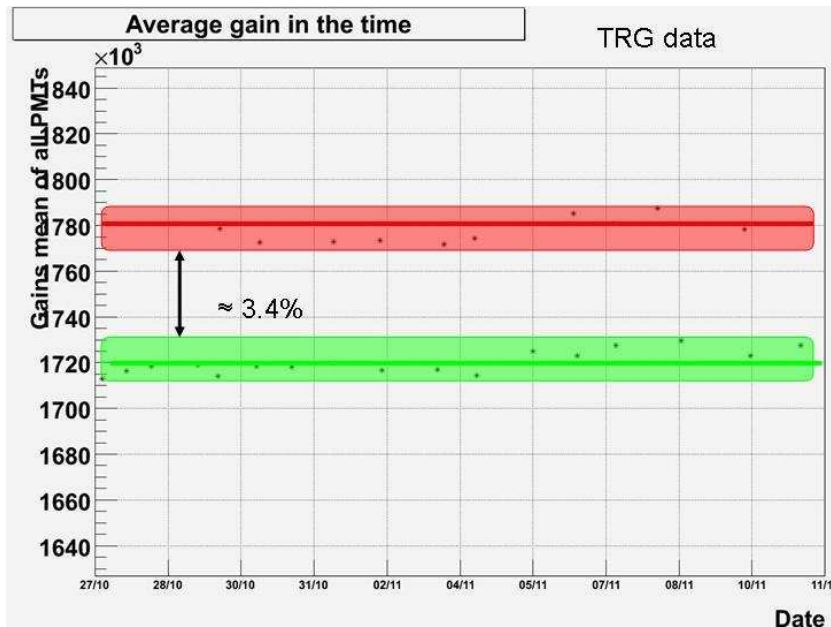


Figure 6.1: Average gain of calorimeter photomultipliers as a function of time. In the red zone, average gain with beam shutter open; in the green zone, average gain with beam shutter closed.

Furthermore we noted that the gain shift is different for the two types of electronic devices used in the experiment: in particular DRS and trigger computed gains are not compatible when computed with beam on. The variation is around 3.4% for trigger data and 1.8% for DRS (fig. 6.2).

In order to understand the gain shift origin (something in the electronic chain, PMTs, etc...) and the difference between trigger and DRS, we performed several tests. At first we studied

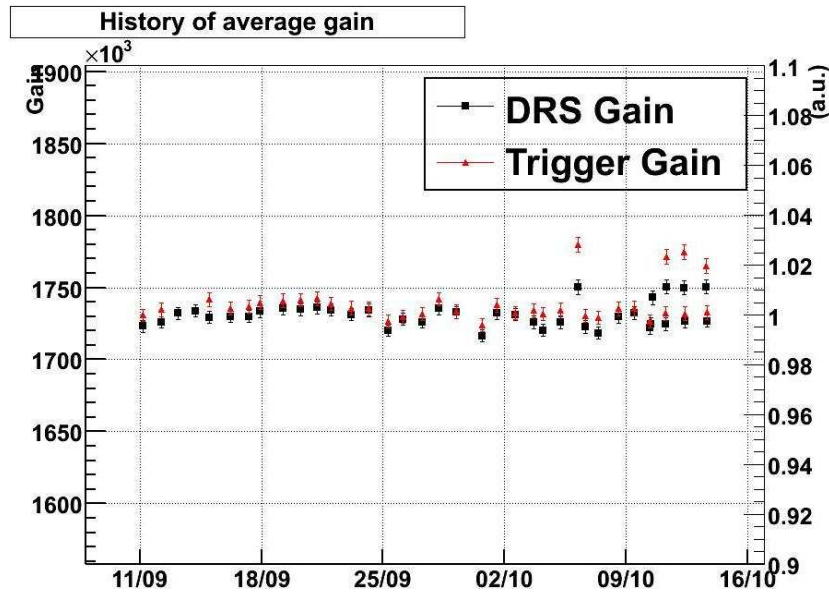


Figure 6.2: Average gain of calorimeter photomultipliers as a function of time: black squares are DRS average gains, red triangles are trigger average gains.

the charge distribution of one particular intensity step of led data and observed two different effects:

1. The charge distribution mean increases of approximately 1.8% in both devices.
2. The charge distribution σ rises and becomes non gaussian in the trigger case while it remains gaussian in the DRS case (figure 6.3).

The second effect can explain the different gain shift between the two digitizing devices: due to the method to estimate gains, the overestimate of the gain in the trigger data is due to the non gaussian distribution of the measured led light which might be explained by the slow sampling speed of the trigger electronics, which is more affected by pile-up in beam-on conditions than DRS. In order to check that the gain shift effect is not related to electronic devices but to the photomultiplier operation in beam conditions, we performed two tests monitoring physical data of alpha sources inside the calorimeter. In the beam-on condition, it is difficult to take alpha data because of the high low energy background. We tried therefore to reproduce this sort of crowding with others devices:

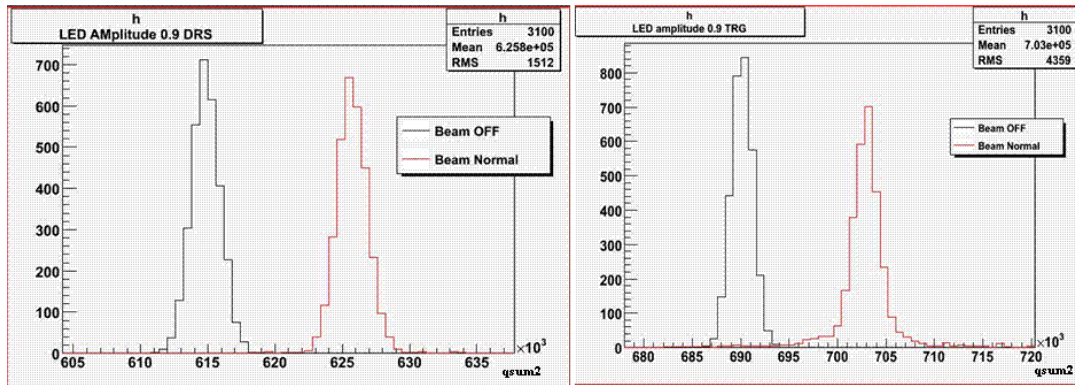


Figure 6.3: Energy distribution of 0.9 amplitude led for DRS(left) and trigger(right). In red we can see the distribution with beam on, in black with beam off. In the trigger with beam on, the distribution is not anymore a gaussian

1. **Using an internal led to simulate background equivalent to normal experimental conditions.** In order to crowd the calorimeter, we used the leds inside the calorimeter with different frequency (5 and 10 kHz) and we took alpha events.

In figure 6.4, the effect for the two frequencies is shown: there is a shift of the alpha peak around 1.6% and 2.3% with frequency equal to 5 and 10 kHz respectively. It is important to note that the alpha spectrum shape remains unchanged while only the peak seems shifted.

2. **Injecting periodic pulse directly on the splitter boards.** The splitter boards are the electronic boards that split the pmts analog signals to send them to the two different acquisition devices. We injected a periodic pulse with 0.6 Volt of amplitude and 200 ns of duration at different frequencies (5,10,20 and 40 kHz) to reproduce the crowding directly on the electronic device. Pulse is injected only in the four splitter board related to 60 photomultipliers of the calorimeter inner face. In figure 6.5 we can see the result of first test: the shift is absent. An equivalent test was performed at INFN Lecce laboratories on a spare splitter board. A periodic pulse was sent to the board and one DRS and one trigger output were checked. In figure 6.6 the amplitude of the output pulse as a function of the frequency for both devices is shown. There are no effects within 0.1%.

From these tests we conclude that the effect is related to PMTs and not to the downstream read-out electronics. We noticed the led light is very stable, more than the computed gain (figure 6.7). We decided, in order to monitor the shift and correct the data taken in experimental

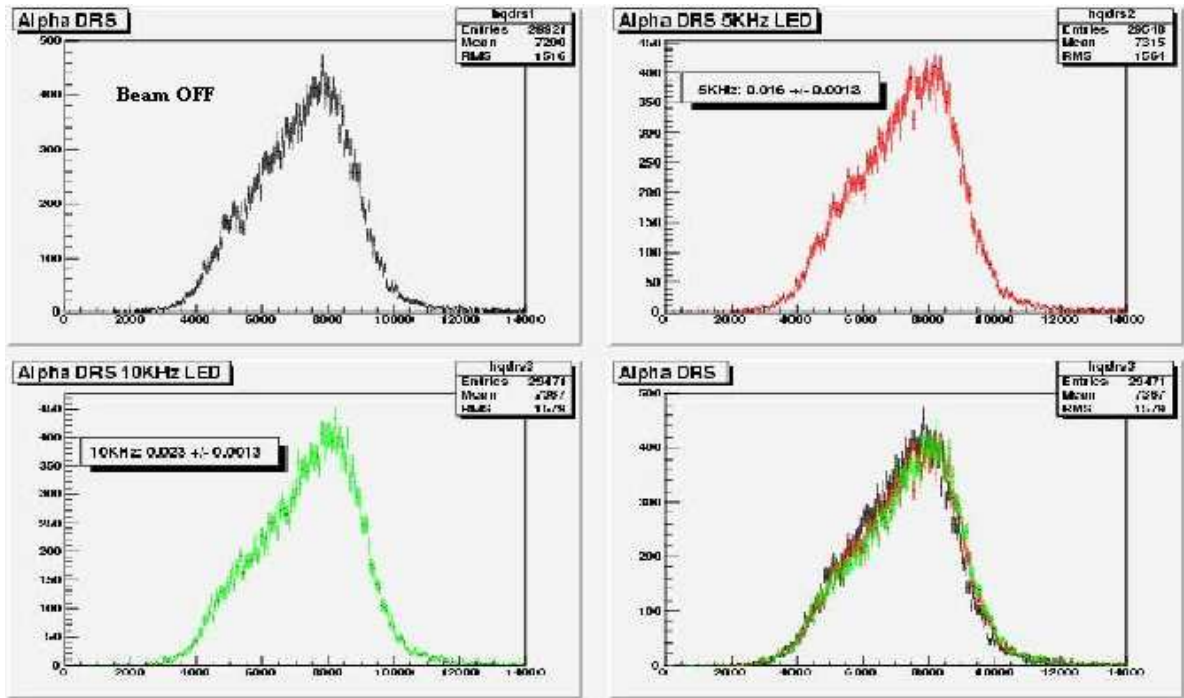


Figure 6.4: Alpha spectrum for DRS at beam off, with crowding led at 5 and 10 kHz.

condition, to add LEDs data (around 0.1 Hz) during normal MEG taking data. Figure 6.8 shows the led peak as function of the beam at different intensity (Low 10^7 , Normal 3×10^7 , High 6×10^7 muon/sec) during opening and closing of the beam shutter. For each fototube, it is possible to compute the gain correction by fitting the led shape, during the opening and the closing of beam shutter at the normal intensity; a triple exponential function is used (see fig.6.9). All the functions parameters are stored in the database and used during data analysis to compute the correct gain related to eventually beam changes, or daily beam shutter opening and closing for calibrations.

6.1.2 Quantum efficiency

As mentioned in section 4, in order to measure QEs, it is necessary to reach a very good identification of the alpha sources and make a comparison with MonteCarlo data. Reflections and absorptions on the calorimeter walls create troubles in simulating the correct light propagation inside of the calorimeter. In figure 6.10, two examples of quantum efficiency fit are shown. Each dot is an alpha source; the number of α -sources that each pmt sees depends on its position

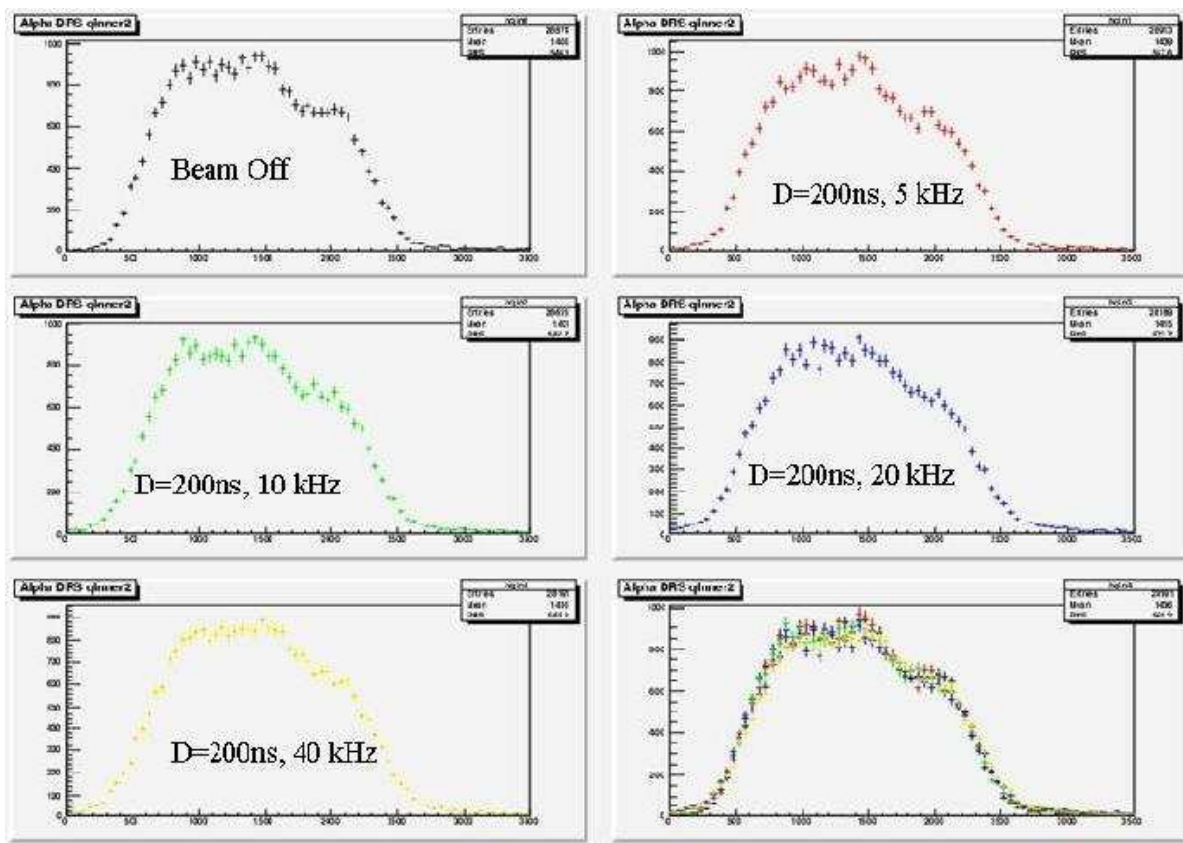


Figure 6.5: Alpha spectrum for for DRS with a periodic pulse injected in the splitter board. It is shown the distribution at different frequencies of the pulse.

in the calorimeter, but they are at least five. The figures 6.11 and 6.12 show the calorimeter uniformity and Lithium peak resolution before and after the QE application.

6.2 Uniformity of the calorimeter

The liquid xenon calorimeter shows a small non-uniformity in the energy response due to geometrical effects. In order to correct these effects, the inner face of the calorimeter is divided in (u, v) regions and the monochromatic 17.6 MeV γ from Lithium is used. Figure 6.13 shows the obtained response map. We performed the same procedure to obtain uniformity in w . The obtained correction factors for (u, v) and w are applied independently.

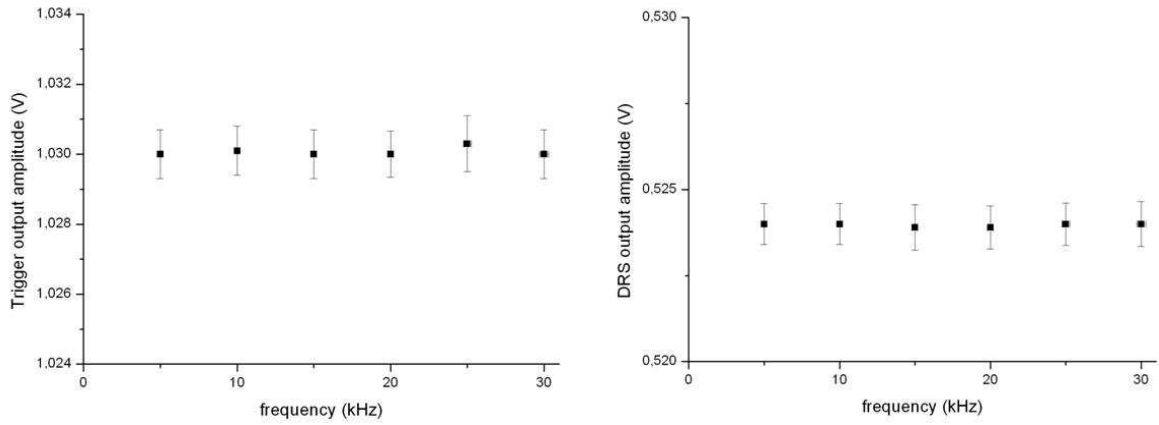


Figure 6.6: Output amplitude of a periodic pulse as a function of frequency for trigger(left) and DRS(right).

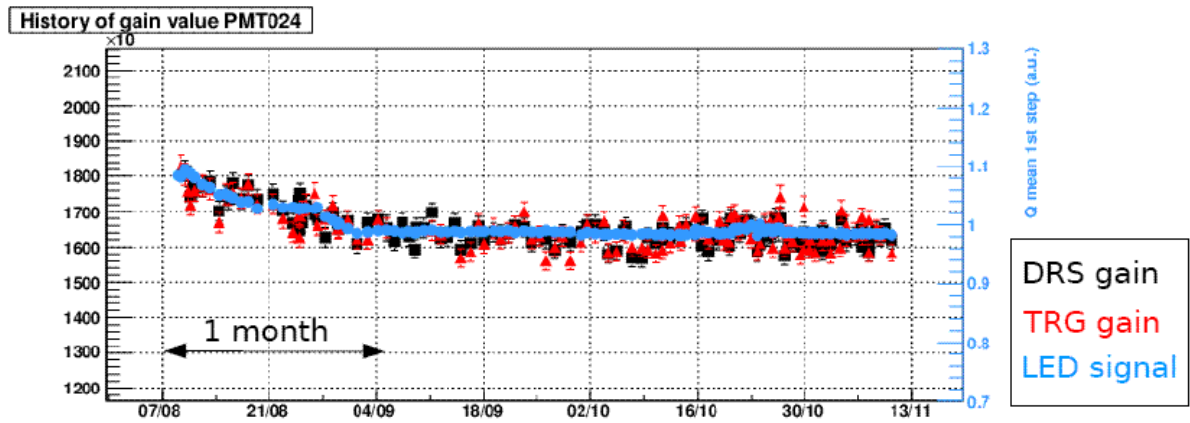


Figure 6.7: History of trigger and DRS gain and the led light for the pmt number 24.

6.3 The energy scale: purification and light yield

The energy scale is calibrated using 55 MeV γ s from π^0 decay. During the 2008 run, the light yield of the calorimeter was changing as a consequence of purification. In order to correct this effect, the LXe light yield was continuously monitored during the whole data taking, observing the position of the energy peaks of the several sources, in particular γ s from Lithium and alpha particles. In figure 6.14, we can follow the history of Lithium peak and 3 different alpha sources (top, middle and bottom of the calorimeter). It is possible to divide the plot in different zones

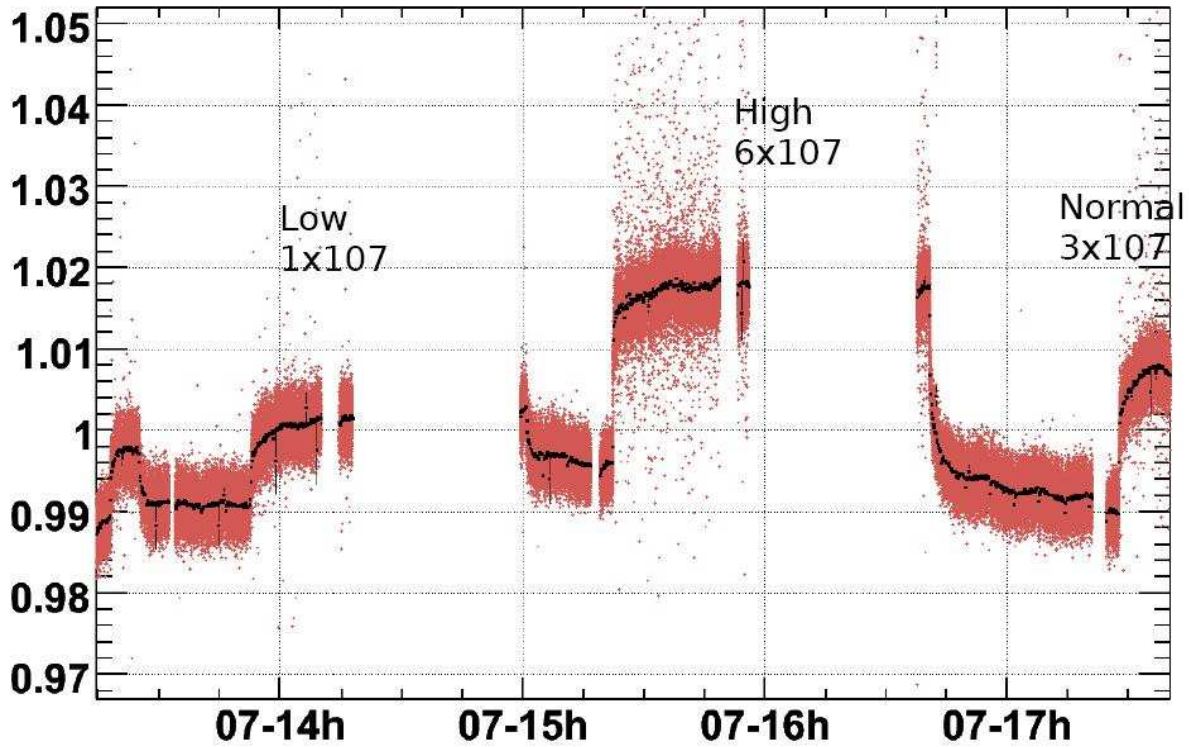


Figure 6.8: Led peak with beam at different intensity (Low 10^7 , Normal 3×10^7 , High 6×10^7 muon/sec). You notices when the beam shutter opens and closes

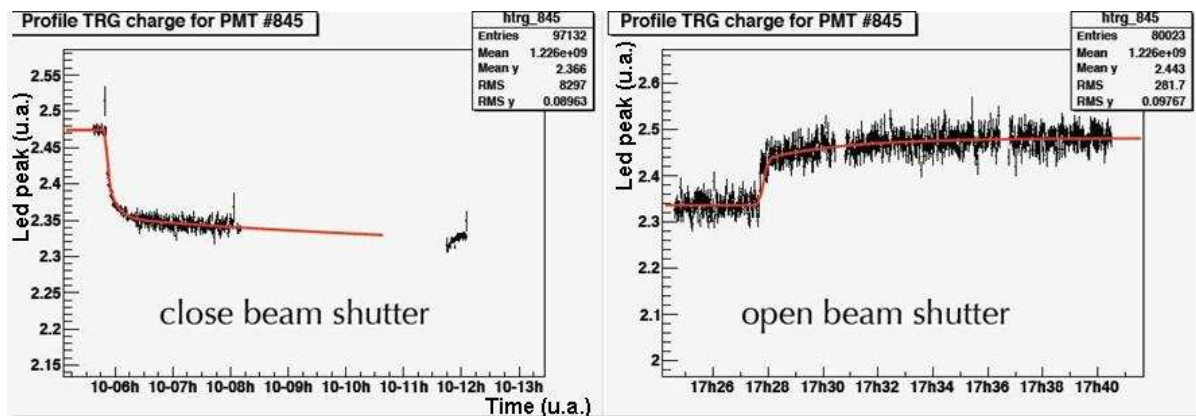


Figure 6.9: Fitting functions of beam shutter opening and closing for PMT 845.

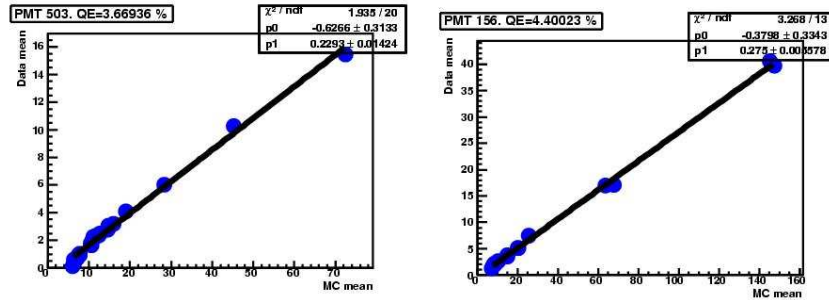
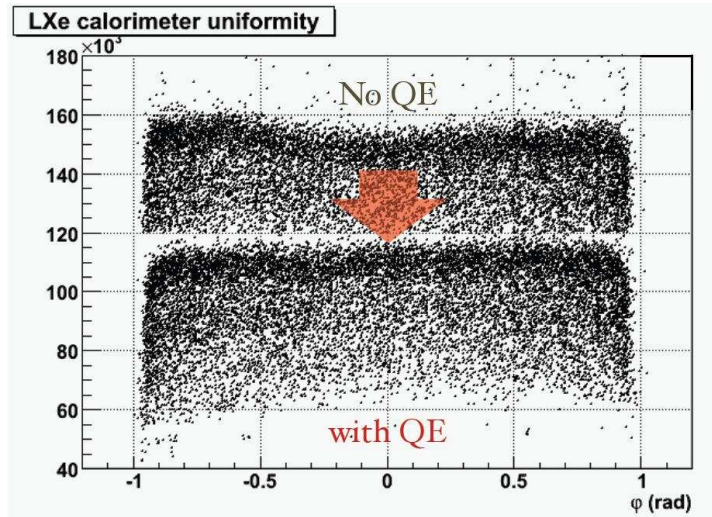


Figure 6.10: Quantum efficiency fit for two PMTs.

Figure 6.11: Uniformity of LXe calorimeter along ϕ variable, before and after the QE application.

related to different situations during the purification:

1. **Initial liquid purification (from 20/5 to 30/5).** In this period we had only Lithium peak data. We can see a very fast rise of light that reached a plateau.
2. **Light monitor (from 31/5 to 24/6).** After attaining of the plateau, we stopped liquid purification and observed a light yield decreasing of about 2% in 4 days.
3. **Gas purification (from 25/6 to 10/9).** After a fast liquid purification in order to recover the plateau condition, we kept the light yield stable within 1% with gas purification. In figure 6.14 we can see in the red circle a light drop and related recovery (with liquid purification) caused by a LXe maintenance problem.

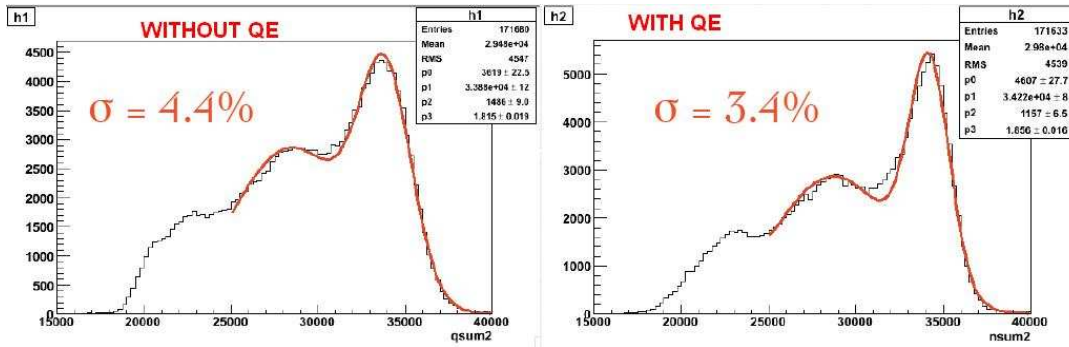


Figure 6.12: Energy resolution of LXe calorimeter on Lithium peak (17.6 MeV γ) before and after the QE application.

4. **Purification Off an light decreasing(from 11/9 to 21/10).** Because of a problem with a pump, the gas purification was stopped and a very slow decreasing was observed ($\approx 3\%$ in 40 days).
5. **Last purification period(from 22/10 to now).** After the pump was repaired, we started with liquid (during beam maintenance period) and gas purification. At first we observed an equal increasing about 10% on alpha and lithium data but later on we observed alpha light stable within 1% and Lithium light strongly increasing.

It is possible to explain these different effects on the two different light sources remembering that α -particles mostly create Xenon excited atoms that produce scintillation light according to the excitation evolution line. Instead, photons produce scintillation light either through a ionization or recombination mechanisms, so a presence of some quench-impurities inside Xenon can induce a different effects on the two light sources (see section 3). Removing impurities would then increase Lithium peak light while keeping alpha peak light stable. Using the methods explained in the chapter 4, we evaluated a $\lambda_{abs} \gg 500cm$ at 90% C.L. (fig.6.15) that confirms the absence of absorbing-impurities. A different ratio between the total charge and the maximum amplitude of their pulses ($\frac{Q}{A}$) is also measured which is in agreement with the fact that α -particles and photons have different decay time constants (see 3.1.1). This difference is an increasing function of Xenon purity: the presence of quenching-impurities reduces the light production through ionization, so it shortens the τ of the γ waveform and makes the two ratios more similar. In figure 6.16, the ratio $\frac{Q}{A}$ before and after purification is shown. In the fourth zone of the figure 6.14, it is clear that the derivative of the Lithium peak photoelectrons number was still positive: this is in agreement with the measurements done with the prototype [88]

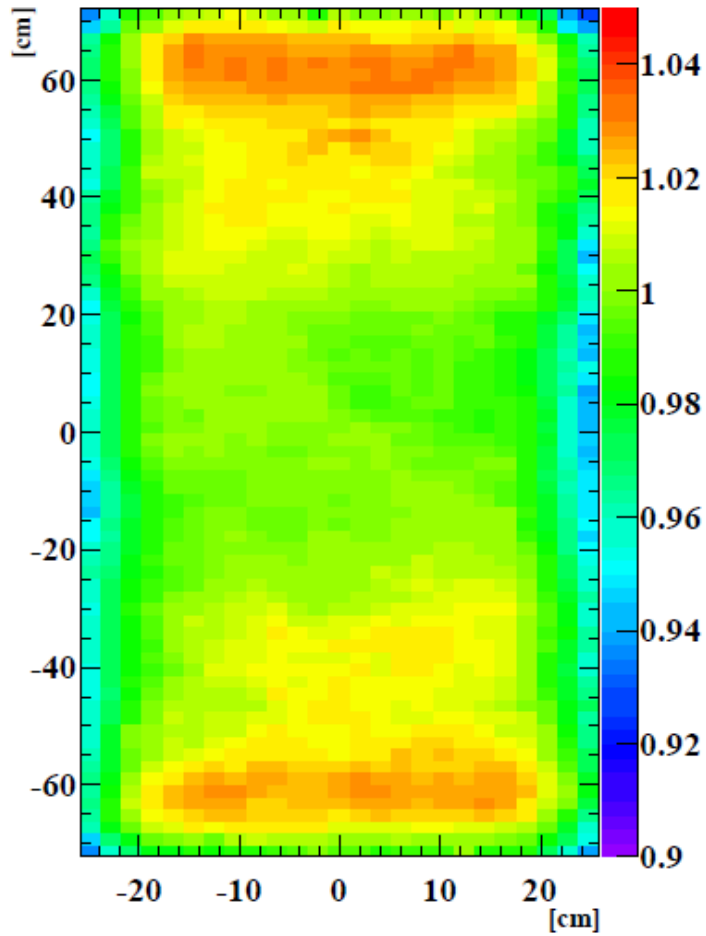


Figure 6.13: Uniformity energy response map in (u, v) -plane using 17.6 MeV from Lithium.

that provides an expected N_{phe} around 30000 at 16.7 MeV .

6.4 Energy linearity and resolution

A fundamental requirement for each calorimeter is energy linearity. The liquid Xenon calorimeter is calibrated using photons with energies from ≈ 4 MeV to ≈ 90 MeV (see 4) therefore it is possible to check the linearity in a large range around the interesting point (52.8 MeV). In figure 6.17 the total collected charge for the various gamma lines from CW (left) and for all gamma lines (right) is shown. In order to measure the calorimeter energy resolution, we used the 54.9 MeV photons from π^0 pion decay. Since CEX runs are performed only at the start or

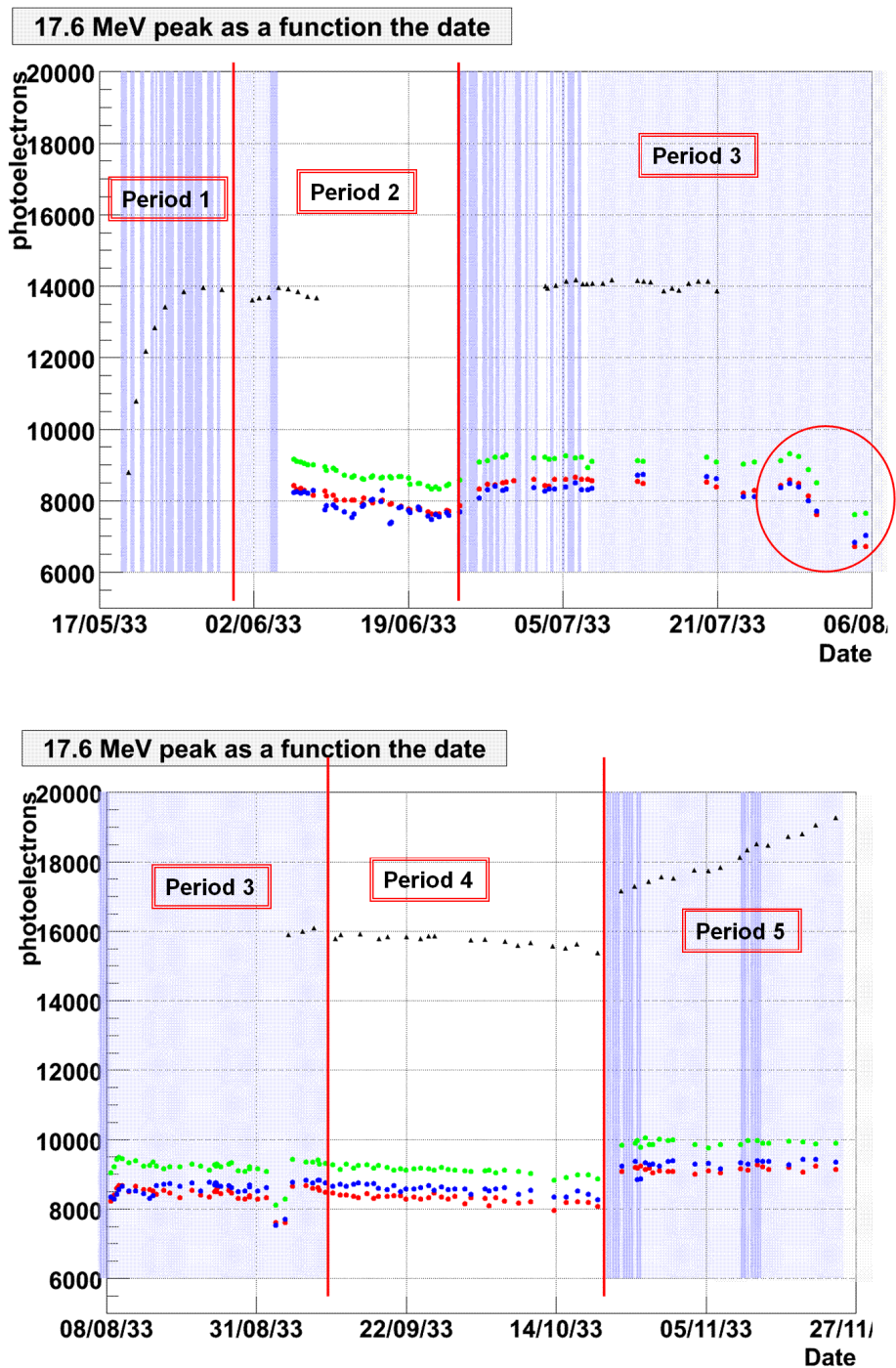


Figure 6.14: In the two picture it is shown the photoelectrons number for Lithium peak (black) and the peaks of three alpha sources (green red,blue) as function of the time to monitor xenon purification. The five periods are explained in 6.3.

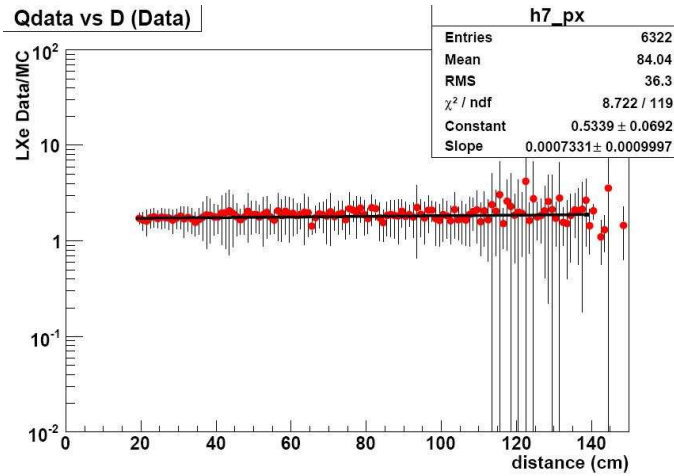


Figure 6.15: Distribution of the ratio of simulated and real photoelectrons number versus the distance of each photomultiplier to evaluate λ_{abs}

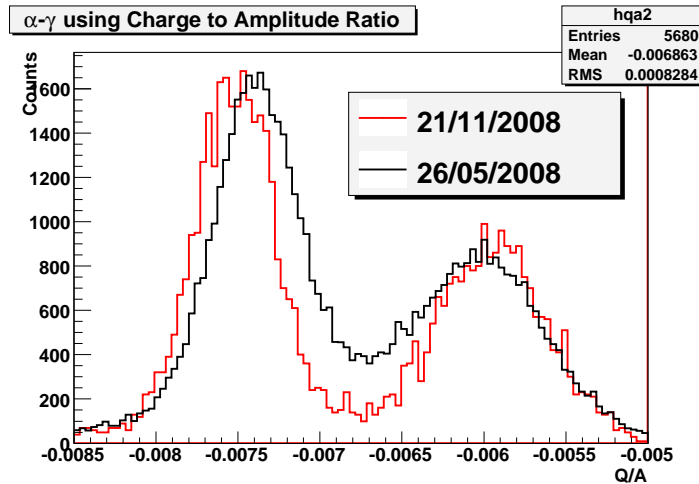


Figure 6.16: Ratio $\frac{Q}{A}$: black line is before the purification start, red line is at 21/11/08.

at the end of the physics run period, to monitor continuously the resolution we used 17.6MeV γ from Lithium and extrapolated to 52.8 MeV energy.

6.4.1 γ from Lithium

On the Lithium data we performed only three cuts:

1. A cut on Z-coordinate and ϕ angle to select a central zone in the calorimeter inner face:

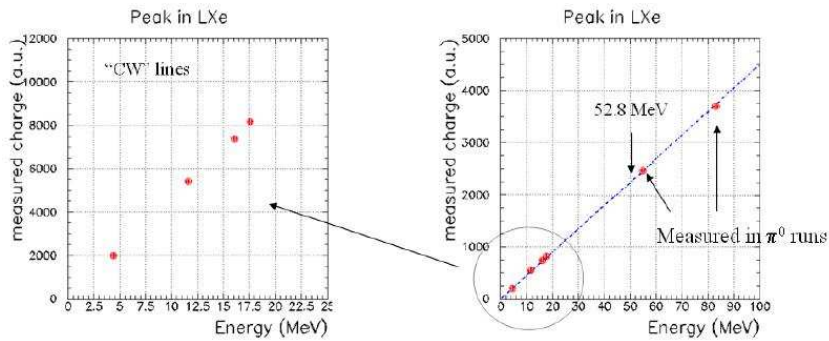


Figure 6.17: Charge at different photon energies in the calorimeter.

$$|Z| < 20 \text{ cm and } |\phi| < 0.5;$$

2. A cut of events with at least one saturated photomultiplier.

The obtained resolution is $\approx 8.9\%$ FWHM 6.18. The extrapolated calorimeter energy resolution at 52.8 MeV is $\approx 5.2\%$ FWHM.

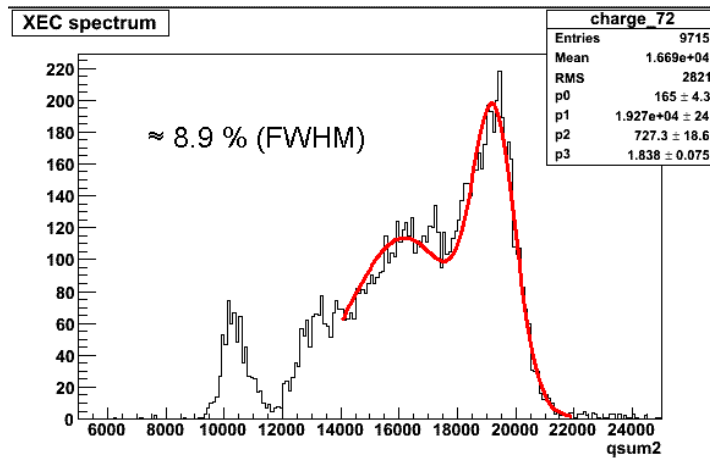


Figure 6.18: Resolution of Lithium Peak (FWHM).

6.4.2 54.9 MeV photons from π^0 decay

In order to have a measurement the resolution near the expected energy of the γ from $\mu \rightarrow e + \gamma$ decay, we used 54.9 MeV photons from π^0 decay. The inner face of the calorimeter was subdivided in 24 different regions, each with a 3x3 group of photomultipliers, and the NaI was

moved in order to select only back to back events in specific regions. For each zone, we collected $\approx 3 \times 10^5$ events and operated some cuts that reduced the events to $\approx 2 \times 10^4$. We selected:

- only events with no energy deposit in the pre-shower crystal (see section 4.5.3);
- opening angle between the two γ s $> 170^\circ$;
- energy fraction released in the central NaI crystal $> 60\%$;
- total energy released in the NaI crystal grid within 15 MeV around 83 MeV to select only 54.9 MeV γ s in the calorimeter;
- reconstructed position inside the calorimeter fiducial volume;
- depth in the calorimeter > 2 cm to remove γ s that converted too near the inner face.

The best resolution in the calorimeter central regions is 4.5% FWHM (fig. 6.19). Figure 6.20 on is 5.8% FWHM.

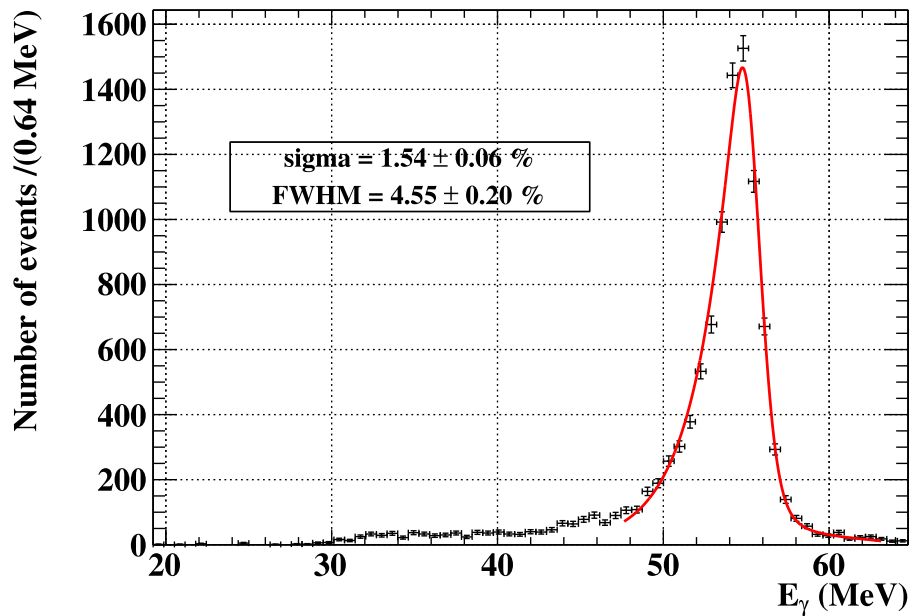


Figure 6.19: Energy resolution (FWHM) for a calorimeter central patch.

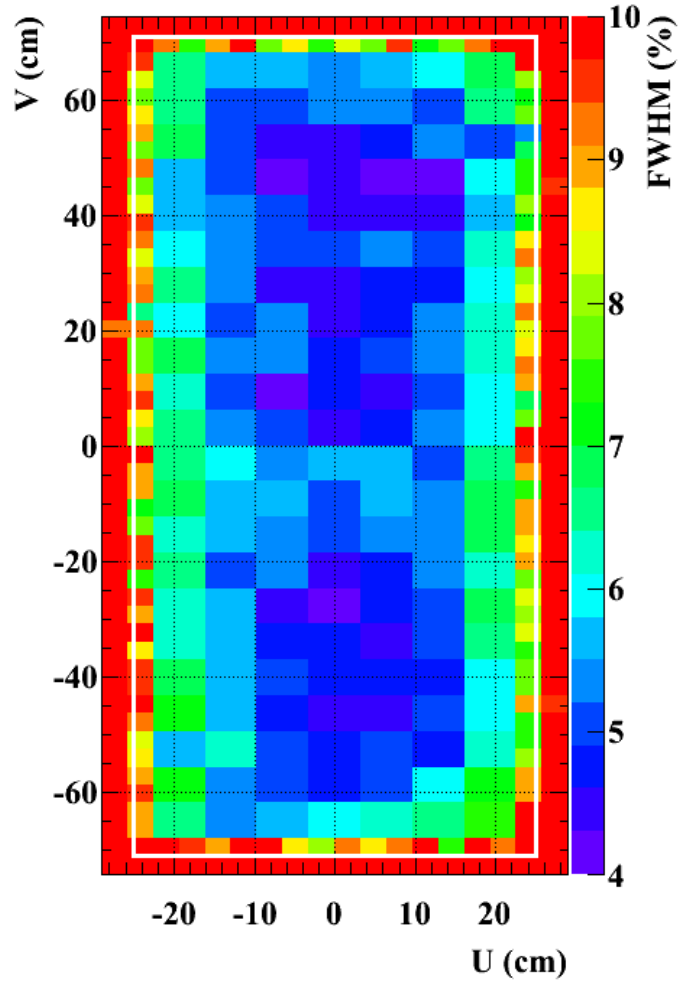


Figure 6.20: Energy resolution (FWHM) distribution.

6.5 Background spectrum

The energy distribution of photons in the calorimeter measured with beam on is shown in figure 6.21, where the comparison between MonteCarlo from proposal (black line) and data (blue markers) shows a very good agreement.

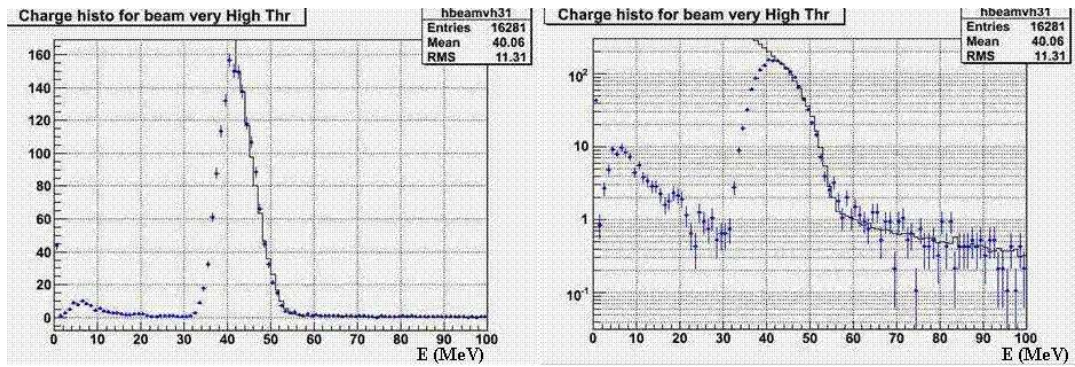


Figure 6.21: Comparison of photons spectra from muon radiative decay between MC (black line) and data (blue markers): linear scale (left) and logarithmic scale (right).

6.6 Position resolution

In order to measure the position resolution of the calorimeter, a lead collimator with holes and sharp edges was placed on the calorimeter inner face (fig. 6.22). Some special runs were taken in this condition during π^0 data taking. The position resolution found to be equal to $\sigma_u \approx 5mm$, $\sigma_v \approx 5mm$ and $\sigma_w \approx 6mm$. In figure 6.23 a view of the collimator by the variable v is shown.

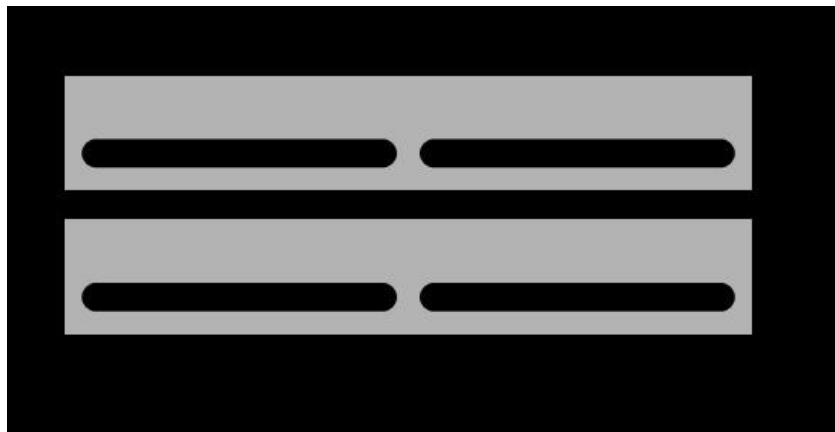


Figure 6.22: Picture of lead collimator used for position resolution measuring.

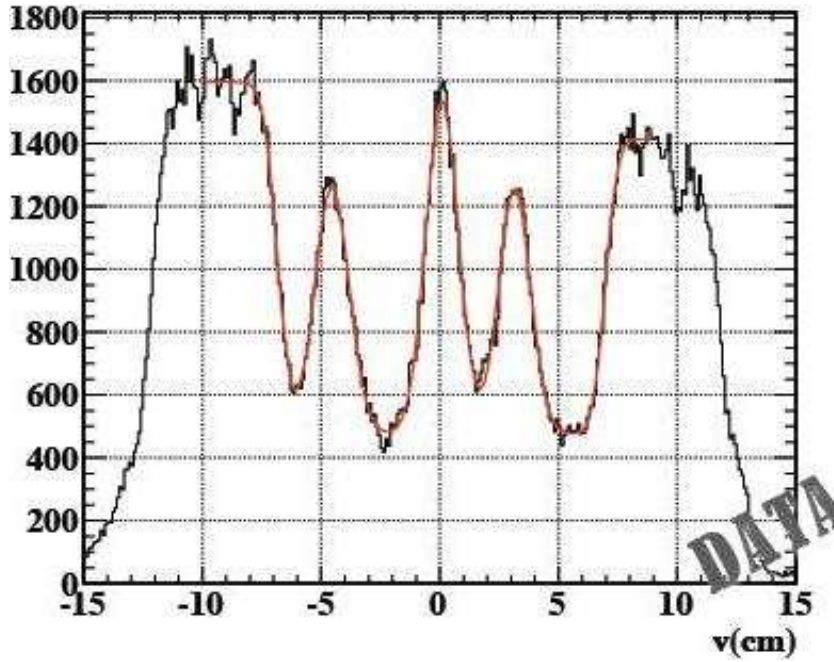


Figure 6.23: View of lead collimator data: in abscissa the variable v .

6.7 Timing resolution

In order to estimate the calorimeter time resolution, we used the γ s from CEX. One of the photons was detected by the calorimeter, the other by two auxiliary plates of a fast scintillator (pre-shower) placed in front of NaI crystal grid (see section 4.5). For timing purposes, we applied the following cuts:

- events with energy deposit in the pre-shower.
- events with reconstructed position inside the calorimeter fiducial volume.

The time difference between the calorimeter and the pre-shower detector is shown in figure 6.24. σ_t is ≈ 145 ps at 55 MeV.

The fluctuation of this difference includes different contributions:

$$\sigma_t^2 = \sigma_r^2 + \sigma_{ps}^2 + \sigma_{H2}^2 \quad (6.1)$$

where σ_r is the real resolution of the photon detector that we are looking for, σ_{ps} is the pre-shower resolution and σ_{H2} is the distribution of the pion decay points due to the not pointlike production target ($\sigma_{H2} \approx 60$ ps).

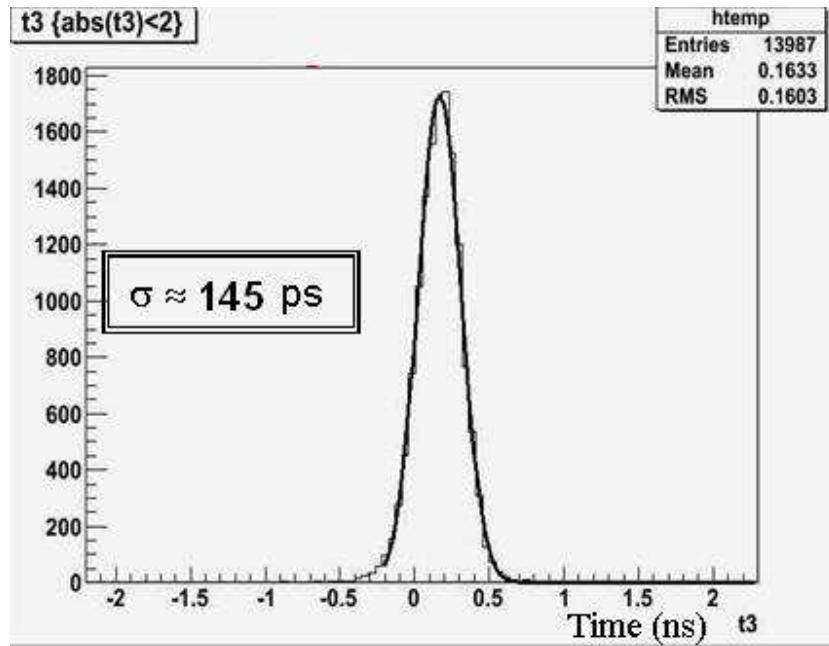


Figure 6.24: Time difference of the gamma ray detector and the preshower at 55 MeV.

In order to estimate σ_{ps}^2 , we could compute the intrinsic time resolution σ_1^{ps} and σ_2^{ps} of both scintillator plates of preshower:

$$\sigma_1^{ps} = \frac{T_1 - T_2}{2} \quad \text{and} \quad \sigma_2^{ps} = \frac{T_3 - T_4}{2} \quad (6.2)$$

where T_1 and T_2 are the times read from the pmts of the first plate and T_3 and T_4 are the times read from the pmts of the second plate. Averaging the two values, we obtained an intrinsic resolution equal to $\sigma_{ps} \approx 93$ ps (fig.6.25). Subtracting from σ_t the two contributions estimated above, we obtained $\sigma_r \approx 90$ ps. In this number contributions due to the position resolution of γ conversion point and to DRS resolution are included. An intrinsic time resolution (not affected by the resolution on the γ conversion point) could be measured by making the difference of times of odd and even phototubes of the calorimeter. We obtained at 55 MeV $\sigma_{int} \approx 50$ ps . In figure 6.26, the σ_{int} as a function of photoelectron number is shown.

6.8 Photon detection efficiency

We define the γ efficiency $\epsilon(\gamma)$ as the probability of detecting a γ at 52.8 MeV, which propagates into the geometrical acceptance of the calorimeter, given a positron of the same energy entering

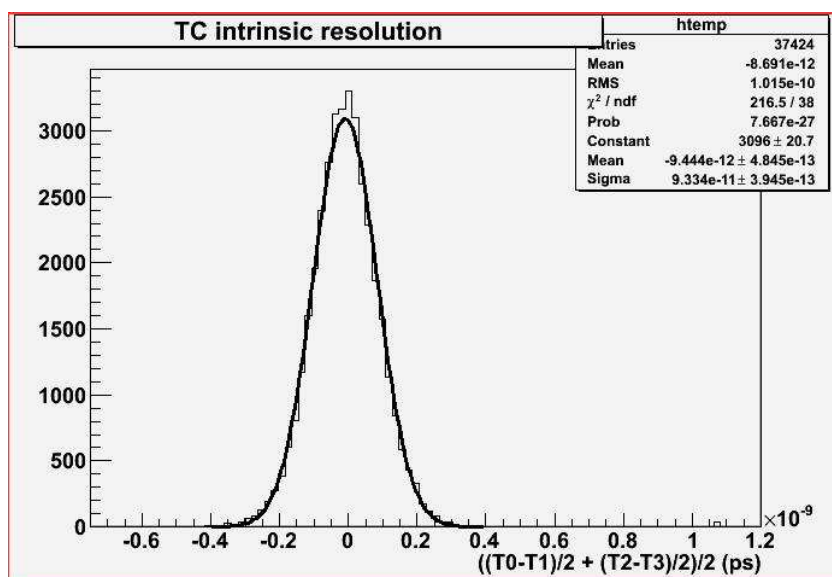


Figure 6.25: Intrinsic time resolution of preshower scintillator.

into the geometrical acceptance of the spectrometer. In order to evaluate $\epsilon(\gamma)$ we used special NaI self trigger runs during CEX run. We selected a photon with energy around 83 MeV in the NaI, so that the corresponding 55 MeV γ ray was in the calorimeter acceptance. By counting the number of photons detected by the calorimeter above 46 MeV, we obtain an estimate of the γ detection efficiency. It is important to note that the number of 83 MeV photons in the NaI is contaminated by the tail of not completely contained 126 MeV γ from $\pi^0 \rightarrow n + \gamma$. To avoid this problem, a correction to eliminate the neutron background in the LXe calorimeter was performed. In figure 6.27, we show the result which gives $\epsilon(\gamma) \approx 60 \pm 3\%$. In the green box the rejected neutron events are shown. This evaluation is confirmed by MC simulation that estimates an efficiency $\approx 61\%$ for photons with energies above 46 MeV.

6.9 Conclusion

The operation of the LXe detector in 2008 run has confirmed its capability as a superior gamma-ray detector. In table 6.9, we summarize the calorimeter resolutions.

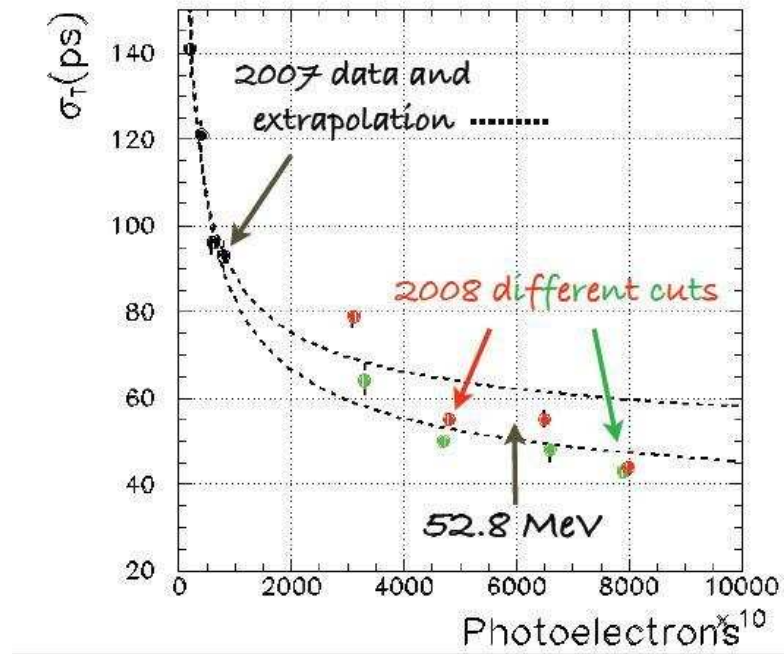


Figure 6.26: The calorimeter intrinsic time resolution as a function of the number of photoelectrons. With the black arrow, the position of 52.8 MeV γ is shown.

Measurement	Average Resolution (FWHM)
γ Energy (on 55 MeV)	$\approx 5.8\%$
γ LXe Radial direction w (mm)	≈ 6.0
γ LXe Surface direction (u,v) (mm)	≈ 5.0
γ Time (nanosecond)	≈ 0.1

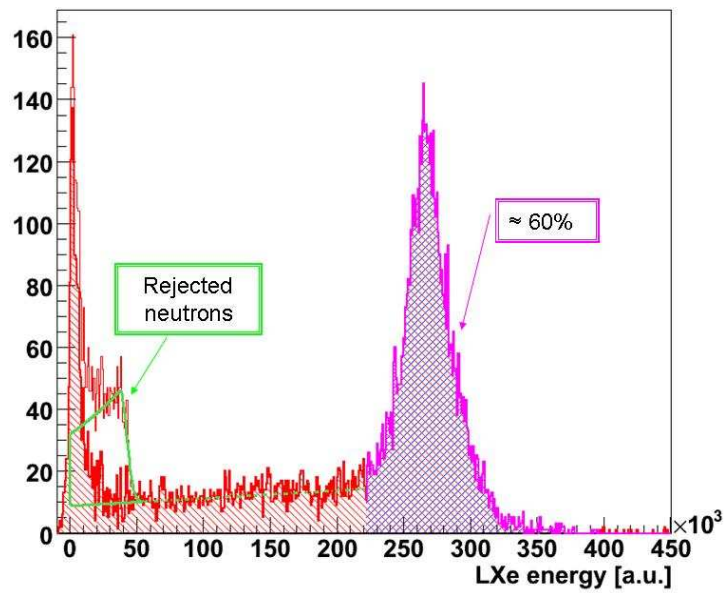


Figure 6.27: LXe γ spectrum with 83 MeV event in the NaI. In the green box rejected neutron events are shown. The events reconstructed with energy above 46 MeV are $\approx 60\%$.

Chapter 7

Other detector performances and efficiencies in MEG 2008 run

At the beginning of this chapter we show the performance of the drift-chambers system and timing counter during the MEG 2008 run. By combining the information from these detectors with the calorimeter performances from the previous chapter, we obtain and show the resolutions on the combined variables (relative angles $\theta_{e\gamma}$ $\phi_{e\gamma}$ and relative time $t_{e\gamma}$). At the end of this chapter we show estimates of the trigger and positron tracking efficiencies.

7.1 Timing Counter: positron time resolution

The TC bars operated for the whole data taking period but it was not possible to use the fibers sub-detector for triggering purposes because of hardware problems. The TC intrinsic timing resolution has been evaluated selecting Michel decay events with two adjacent bars hit, assuming the two bars having the same intrinsic resolution, and calculating the time difference between the average time measured by the two PMTs of each bar. This estimate is to be considered as an upper limit, because we don't take care of the positron incidence angle with respect to the bars. The plot in fig.7.1 shows the time resolutions as function of the second bar hit.

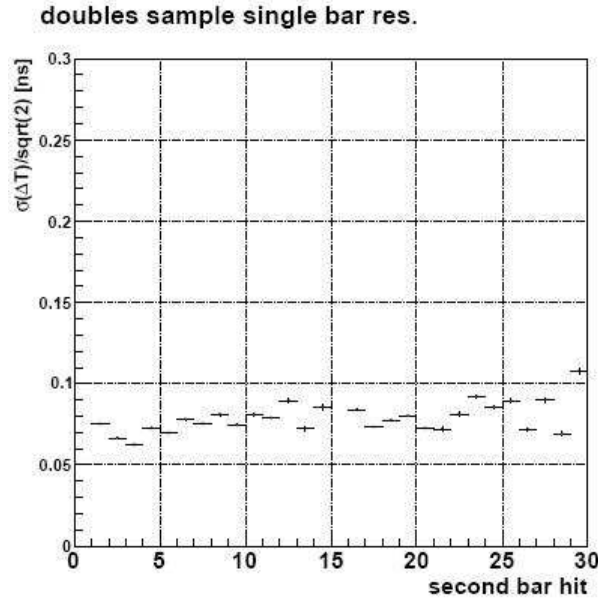


Figure 7.1: Time resolution versus bar id.

7.2 Drift chamber: positron energy and angular resolutions

The drift chambers were installed in May and started to operate in June. After about two months of operation, high voltage trips started to occur, reducing positron efficiency and resolutions. Figure 7.2 shows the DC situation in different periods during the 2008 run: the green box correspond to working chambers, orange box to switched off chambers.

The positron track was reconstructed with the Kalman filter technique [89], in order to take into account the effect of multiple scattering and energy loss in the detector materials in the variable magnetic field. The positron energy scale and resolution are evaluated by fitting the kinematic edge of the measured Michel positron energy spectrum at 52.8 MeV as shown in fig.7.3 . The fit function is formed by folding the theoretical Michel spectrum with energy-dependent detector efficiency, and the response function for mono-energetic positrons. The latter is extracted from the Monte Carlo simulation of $\mu \rightarrow e + \gamma$ decays, and is well described by a triple Gaussian function (a sum of a core and two tail components). The multi-gaussian fit of the resolution function to data yields 374 KeV, 1.06 MeV and 2.00 MeV sigma for the core component and the two tails, with corresponding fractions of 60%, 33% and 7% respectively. The uncertainty on these numbers is dominated by sistematcis effects and was determined by

Date	0	1	2	3	4	5	6	7	8	9	10	11	12	13	14	15
14 - 16 Sept	Green	Green	Orange	Green	Green	Orange	Green	Green	Green	Green	Orange	Green	Green	Orange	Green	Green
1 - 3 Oct	Green	Green	Orange	Green	Green	Orange	Green	Green	Green	Green	Orange	Green	Green	Orange	Green	Green
13 - 15 Oct	Green	Green	Orange	Orange	Green	Green	Green	Green	Green	Green	Orange	Green	Green	Green	Orange	Green
3 - 4 Nov	Green	Orange	Orange	Orange	Green	Green	Green	Green	Green	Green	Green	Green	Orange	Orange	Orange	Green
13 - 15 Nov	Green	Orange	Orange	Green	Orange	Green	Green	Green	Green	Green	Orange	Green	Orange	Orange	Green	Orange
26 - 28 Nov	Green	Orange	Orange	Green	Orange	Green	Green	Green	Green	Green	Green	Green	Orange	Orange	Orange	Green
13 - 14 Dec	Green	Orange	Orange	Orange	Orange	Green	Green	Green	Green	Green	Orange	Green	Orange	Orange	Orange	Green

Figure 7.2: The DC performances as a function of time. The orange boxes correspond to DCs which were switched off.

performing the fit in different configurations.

The positron angular resolution is evaluated by exploiting tracks that make two turns in the

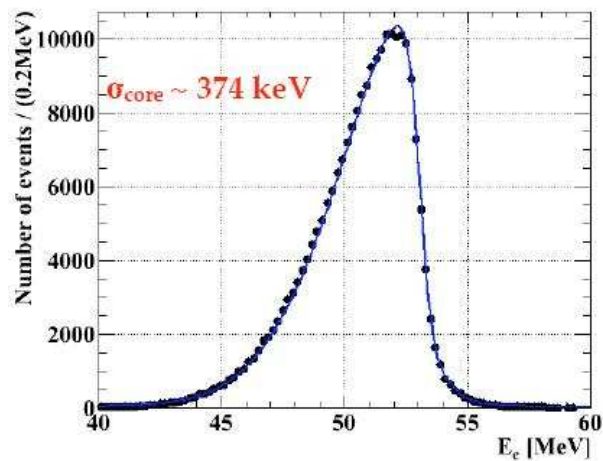


Figure 7.3: Positron energy resolution with fit resolution.

spectrometer, where each turn is treated as an independent track. The θ - and ϕ -resolutions

are extracted separately from the difference of the two track segments at the point of closest approach to the beam-axis and are measured to be $\sigma_\theta = 18$ mrad, $\sigma_\phi = 10$ mrad. The starting positron direction and decay vertex position are determined by projecting the positron back to the target. The vertex position resolutions are measured to be ≈ 3.2 mm and ≈ 4.5 mm in the vertical; and horizontal directions on the target plane respectively, by looking at the reconstructed edges of several holes made in the target, for this purpose.

7.3 Relative angles $\theta_{e\gamma}$ $\phi_{e\gamma}$

The determination of positron direction and vertex is described in the previous section. The γ -ray direction is defined by the line linking its reconstructed conversion point in the liquid Xenon detector (see section 6.6) with the vertex of the candidate companion positron. By combining the individual detector resolutions, relative average resolutions of 21 and 14 mrad for $\theta_{e\gamma}$ and $\phi_{e\gamma}$ are obtained respectively.

7.4 Relative time $t_{e\gamma}$

In order to estimate the timing resolution on the timing difference $t_{e\gamma}$ between positron and γ , we used two different type of events, both with a topology very similar to the signal events:

- Dalitz events $\pi^0 \rightarrow e^+e^-\gamma$, used also to evaluate the absolute LXe-TC time offset.
- The muon radiative decay $\mu^+ \rightarrow e^+\gamma\bar{\nu}_\mu\nu_e$, to evaluate the timing resolution closer to the photon energy of $\mu e\gamma$ event.

7.4.1 Dalitz process

The Dalitz decay ($\pi^0 \rightarrow e^- + e^+ + \gamma$) has a branching ratio $\approx 1.2\%$. We acquired Dalitz events during CEX runs. The trigger selected events with a photon in the calorimeter and an hit in TC. Furthermore it required a time coincidence and a loose angular correlation between the two particles. Offline we required also one reconstructed track in the drift chamber and cut on γ -energy ($E_\gamma > 45$ MeV). Subtracting to both particles the time of flight between target and detector, we can evaluate the mean and the width of the time difference distribution. The first one was used as LXe-TC time calibration constant, the second one gave an evaluation of $t_{e\gamma}$ resolution. We obtained a mean value ≈ 26 ns and a σ -value ≈ 238 ps (fig. 7.4).

The mean value is used as LXe-TC time calibration constant. It is important to note that

this resolution estimate is an upper limit. Indeed the LH2 target is not a thin target, so the reconstruction of the decay vertex is much less accurate.

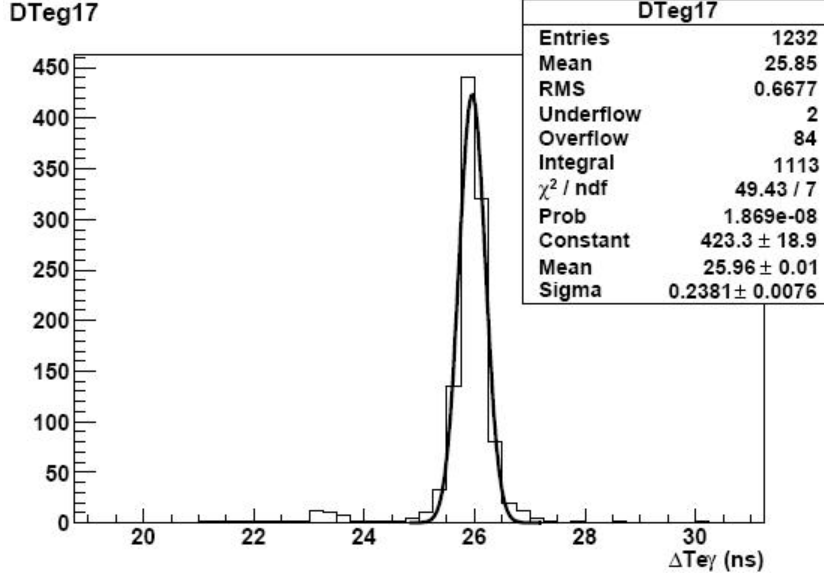


Figure 7.4: The LXe-TC time resolution from Dalitz events.

7.4.2 Radiative decay peak

The identification of the rare radiative decay is a demonstration of the quality of MEG experiment, since these events are very similar to the ones of $\mu^+ \rightarrow e^+\gamma$ decay. Since radiative decay events are time coincident, they make a peak in time distribution on top of the flat distribution of accidental background. We used events with $40 < E_\gamma < 45$ MeV, in the $E\gamma$ -sideband (see next chapter). Figure 7.5 shows the radiative decay peak. Considering the small E_{gamma} -dependence observed in the π^0 -runs, the timing resolution for the signal is estimated to be $\sigma_{e\gamma} = 140 \pm 17$ ps. This resolution was monitored over the whole data-taking period and was found to be stable to within 20 ps.

7.5 MEG detectors efficiencies

In order to reach a final result, it is essential to know the different detector efficiencies. In this section, we show the positron detection and the trigger efficiencies.

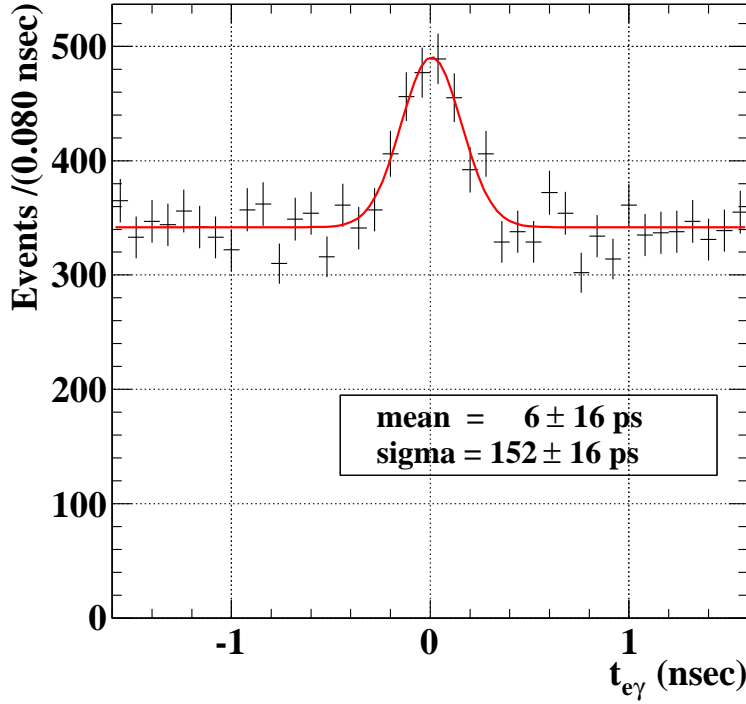


Figure 7.5: The relative time distribution $t_{e\gamma}$ showing the RMD peak obtained during physics runs, for $40 < E_\gamma < 45$ MeV.

7.5.1 Positron detection efficiency

We can write the positron detection efficiency $\epsilon(e^+)$ as:

$$\epsilon(e^+) = P(e^+ \in DC | e^+ \in A_G) \times P(e^+ \in TC | e^+ \in DC, e^+ \in A_G) = \epsilon(DC) + \epsilon(TC - DC) \quad (7.1)$$

where A_G is the geometrical acceptance for Michel positrons, estimated to be $\approx 12\%$ by using MC simulation; the first term ($\epsilon(DC)$) is the drift chambers efficiency (that is the probability that a positron is detected by the DCs when it is in their geometrical acceptance A_G) and the second term ($\epsilon(TC - DC)$) is the TC-DC matching efficiency (that is the probability that a positron is detected by the TC where it is in geometrical acceptance and is detected by the DCs). In order to estimate $\epsilon(e^+)$ we used Michel positrons with $E_{e^+} > 50$ MeV taken in the physics runs as a control sample.

TC-DC matching efficiency ($\epsilon(TC - DC)$)

The estimate of $\epsilon(TC - DC)$ was made by using a data sample of the DCH-alone trigger. This trigger requires a minimum of 4 hits in 5 consecutive chambers without any reference to the TC information. We applied only a cut to remove the tracks which are out of timing-counter digitization time because the digitization window of the drift chamber is wider than that of the timing counter. The ratio between the tracks and the matched tracks gives the efficiency. Figure 7.6 shows the efficiency as function of the positron energy: extrapolating to 52.8 MeV we obtain $\epsilon(TC - DC) = 38\%$. The inefficiency is due to a positron change of trajectory because of different interactions (multiple scattering, annihilation, energy loss, etc...) with the spectrometer material.

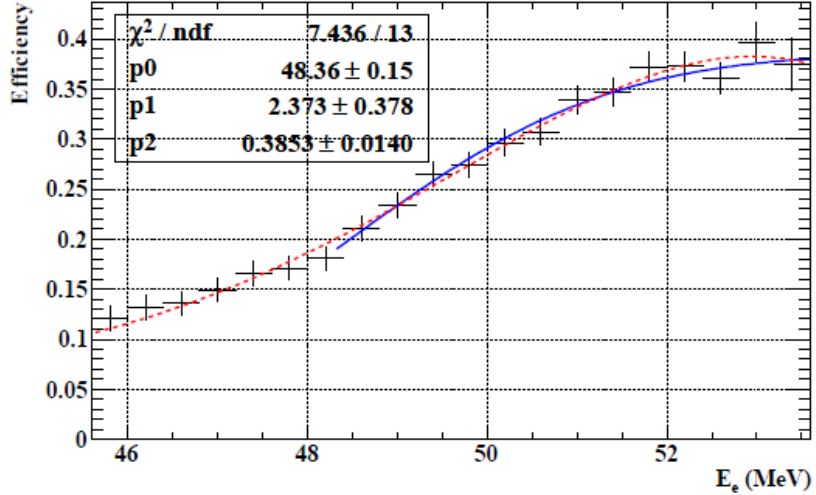


Figure 7.6: $\epsilon(TC - DC)$ as function of positron energy.

Drift chamber efficiency ($\epsilon(DC)$)

We estimated the $\epsilon(DC)$ by using two different methods:

1. **By using a data sample of pedestal trigger, identifying Michel events and counting the track multiplicity.** The track multiplicity distribution of Michel events is expected to be a Poisson:

$$p(n) = \frac{\mu^n e^{-\mu}}{n!} \quad (7.2)$$

where n is a given track multiplicity and μ is:

$$\mu = R_e \times T \quad (7.3)$$

with R_e is the positron rate investing the DC system and $T = 500$ ns is the DRS time window. We can write R_e as:

$$R_e = R_\mu \times A_G \times \bar{\epsilon}(DC) \quad (7.4)$$

where R_μ is the rate of muons stopped in the target ($\approx 3 \times 10^7$) and $\bar{\epsilon}(DC)$ is the drift chamber efficiency averaged on Michel spectrum over the momenta accepted by DC system ($p_e > 35$ MeV/c). Substituting in equation 7.3:

$$\bar{\epsilon}(DC) = \frac{\mu}{R_\mu \times A_G \times \bar{\epsilon}(DC) \times T} \quad (7.5)$$

Figure 7.7 shows the track multiplicity distribution for a data sample at the beginning of run 2008. Applying equation 7.5 to this data sample, we obtained $\bar{\epsilon}(DC) \approx 40\%$. From

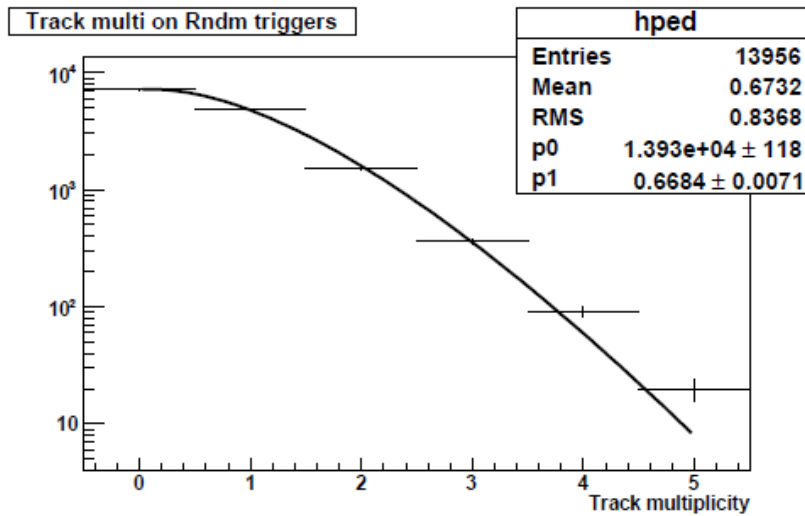


Figure 7.7: Drift chamber track multiplicity for a data sample at the beginning of the 2008 MEG Run.

simulation of Michel positrons entering the geometrical acceptance we obtained $\bar{\epsilon}(DC) \approx 38\%$ consistent with data. From MC we estimate $\epsilon(DC)$, for the MEG signal (52.8 MeV) at the beginning of the 2008 run, equal to 83% (most of chambers on). Figure 7.8 shows the MC simulated DC efficiency as function of the Michel positron momentum (at

the beginning of the 2008 run). Due to the frequent trip problems, the DC efficiency decreased during the run: at the end of 2008 run we estimate $\bar{\epsilon}(DC) \approx 10\%$ from data, $\bar{\epsilon}(DC) \approx 9\%$ from MC and $\epsilon(DC) \approx 23\%$ at the MEG signal. Averaging of the whole 2008 run we obtained $\epsilon(DC) \approx 40\%$ for 52.8 MeV.

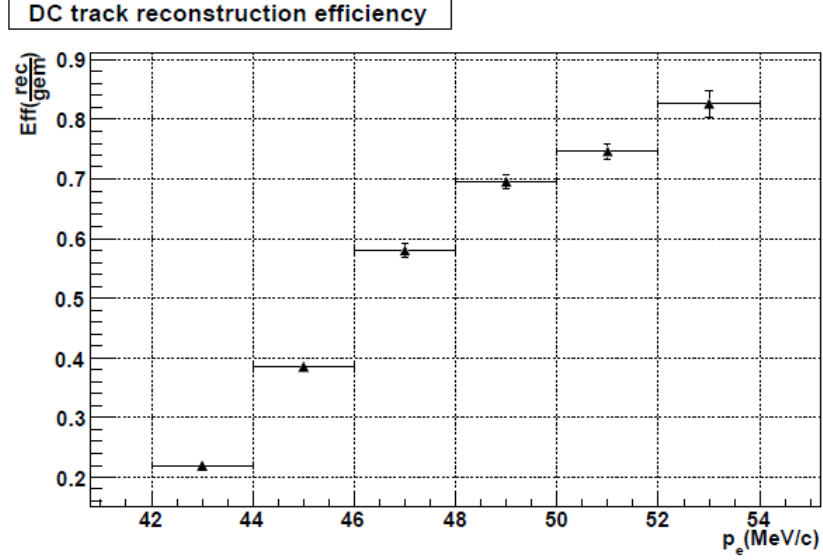


Figure 7.8: The MC simulated DC efficiency as a function of the Michel e^+ momentum at the beginning of the 2008 MEG Run.

2. **By using a data sample of TC-alone trigger.** We can write the number of observed Michel positrons on TC as:

$$N_{obs} = N_{\mu} \times f(E_e > 50MeV) \times A_G \times \epsilon(DC) \times \epsilon(TC - DC) \times \frac{1}{P} \quad (7.6)$$

where N_{μ} is the number of muons stopped in the target estimated by using R_{μ} , $f(E_e > 50MeV)$ is the fraction of Michel positrons over 50 MeV (computed ≈ 0.101), A_G geometrical acceptance and P prescaling factor of TC-alone trigger (10^7). Substituting the $\epsilon(TC - DC)$ computed in 7.5.1, we obtained an average $\epsilon(DC) \approx 37\%$ during the whole 2008 run.

Positron efficiency estimate

From the previous estimates we obtained:

1. **Using method 1.** Combining the $\epsilon(DC) \approx 40\%$ and $\epsilon(TC - DC) = 38\%$, we obtained $\epsilon(e^+) = 15\%$.
2. **Using method 2.** Without substituting the $\epsilon(TC - DC)$, we obtained an estimate of positron efficiency $\approx 14\%$.

7.5.2 Trigger efficiency

As said in section 2.4.1, to select $\mu \rightarrow e + \gamma$ the trigger uses three different variables: γ energy from calorimeter, $t_{e\gamma}$ from calorimeter and timing counter and $e-\gamma$ collinearity from calorimeter and timing counter.

- **E_γ .** In order to check the efficiency and choose the best threshold for MEG trigger, the 55 MeV γ s from CEX were used. In fig.7.9 the resolution of the online energy measure is shown: choosing a 40 MeV threshold, the γ -energy trigger efficiency is $>99\%$. Because of the unstable light yield, the energy threshold was not fixed at 40 MeV but changed during the data taking. Figure 7.10 shows the threshold as a function of run number.
- **$t_{e\gamma}$.** In order to center the time window and estimate the online time resolution, Boron events were used. We obtained an online time resolution $\approx 3-4$ ns. Figure 7.11 shows the trigger $t_{e\gamma}$ distribution (red) and the simulated signal $t_{e\gamma}$ distribution (blue): choosing a time window about 20 ns, the relative time trigger efficiency is $>99\%$.
- **$e - \gamma$ collinearity.** As explained in section 2.4.1, in order to reconstruct the angle between positrons and photons, the trigger system uses the calorimeter pmt with the maximum charge, the positron impact point on timing counter and a lookup table to correlated the two ones. To estimate the relative trigger efficiency, we selected events with a special trigger that did not require collinearity constraints. We reconstructed the track and compared the measured maximum charge pmt and TC impact point with the values in the lookup table. We obtained a collinearity efficiency $\approx 66 \pm 2\%$. This value, below expectations, was due to different factors:
 - in the simulation used to compute the lookup table for direction match, we did not use the measured QEs because they were measured with high precision only after the begin of the run;
 - a large fraction ($\approx 50\%$) of events has at least one saturated PMT of the calorimeter inner face, larger than the effect foreseen in MC;

- the direction match lookup table was build-up assuming that the z coordinate along the TC would have been provided by the TC fibers. Unfortunately the TC fibers were not available during 2008 run and the z measurements was changed to the charge asymmetry of the PMT amplitudes;
- we applied a cut at 45 MeV to the signal e^+ momentum before entering the TC. This was set to exclude events in which positrons loosed to much energy into drift chambers and the material into the COBRA magnet modifying its trajectory. This cut turned out to be too tight.

More information about trigger efficiency is given in [90].

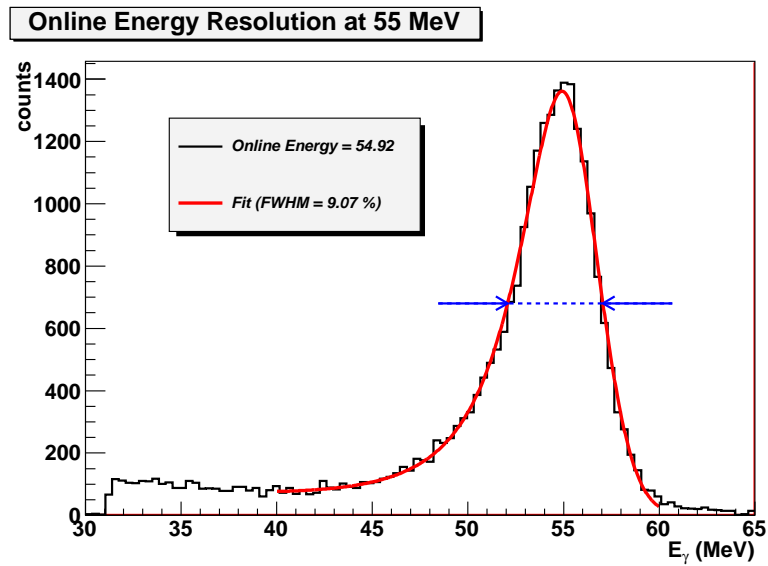


Figure 7.9: Online energy resolution on 55 MeV γ s from CEX run.

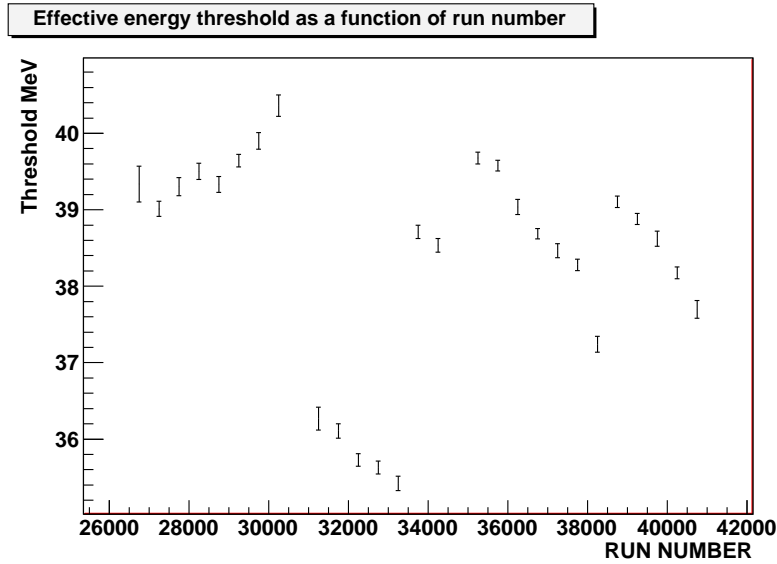


Figure 7.10: Trigger E_γ threshold as a function of run number.

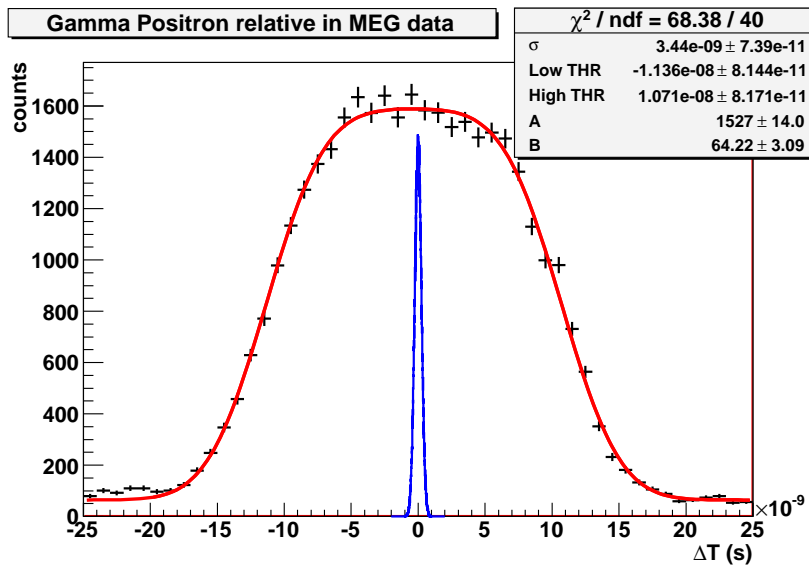


Figure 7.11: Time distribution for radiative decay (red) and simulation of signal event (blue).

Chapter 8

Final analysis of 2008 MEG run

This chapter shows all the steps of run 2008 data analysis and how the final 90% confidence level upper limit was obtained. To avoid introducing biases in analysis, we adopted a combination of blind and likelihood analysis. We defined a blind box in the $(T_{e\gamma}, E_\gamma)$ -plane in the region where signal events are expected. The number of signal events is extracted by means of a maximum likelihood fit to event distributions in e^+ and γ energy, relative angle and timing.

8.1 Data samples and selections

In 2008 we collected 9.5×10^{13} muons which stopped in the target. In a first analysis stage, a data reduction was performed by selecting events with the following conservative criteria:

- at least one positron track detected by the drift chamber system;
- $-6.9 \text{ ns} < T_{e\gamma} < 4.4 \text{ ns}$. The timing interval is asymmetric in order to acquire multi-turn events, since in this stage we don't use track length and then we don't know the number of turns before the positron hit the timing counter.

These requests reduced the data size to 16% of the recorded events. We call this group of events "preselected". Inside the preselection box, we performed further stricter selections and divide the surviving events in three subgroups (fig.8.1):

- Events in the blind box, falling into the signal region with $48 \text{ MeV} < E_\gamma < 57.6 \text{ MeV}$ and $|T_{e\gamma}| < 1 \text{ ns}$. These events are potential $\mu e\gamma$ candidates and were saved in separate hidden files as required by the blind analysis procedure. For the analysis purposes, the

likelihood fit was performed in an extended region in E_γ ($46 \text{ MeV} < E_\gamma < 60 \text{ MeV}$): we called this fit region “analysis box”;

- Events in E_γ sideband, falling into the region with $44 \text{ MeV} < E_\gamma < 48 \text{ MeV}$, just below the blind box. In this region most of the radiative decay events used to optimize the analysis parameters, define the selection criteria and give an estimate of the radiative events in the analysis region, lie;
- Events in $T_{e\gamma}$ side-bands, falling into the region with $48 \text{ MeV} < E_\gamma < 58 \text{ MeV}$, and $[-3.5 < T_{e\gamma} < -1.5 \text{ ns (left)}]$ or $[1.5 < T_{e\gamma} < 3.5 \text{ ns (right)}]$, needed to estimate sensitivity and check the maximum likelihood fit algorithms;

The blind box was opened after completing the optimization of the analysis algorithms and the background studies (see previous chapters).

The analysis selection criteria are listed below:

- XEC pileup and cosmic rejection cuts;
- Photon conversion point reconstructed into the calorimeter fiducial volume;
- $50 \text{ MeV} < E_e < 56 \text{ MeV}$;
- $46 \text{ MeV} < E_\gamma < 60 \text{ MeV}$;
- $|\Delta\phi| < 0.1 \text{ rad}$;
- $|\Delta\theta| < 0.1 \text{ rad}$;
- Match DCH-TC;
- $t_{e\gamma} < 1 \text{ ns}$.

8.2 Likelihood analysis

An extended likelihood function was constructed as:

$$L(N_S, N_{RMD}, N_{BG}) = \frac{N^{N_{obs}} e^{-N}}{N_{obs}!} \prod_{i=1}^{N_{obs}} \left[\frac{N_S}{N} S + \frac{N_{RD}}{N} RD + \frac{N_B}{N} B \right] \quad (8.1)$$

where N_S , N_{RD} , N_B are the number of signal, radiative decay and accidental background events respectively, S , RD and B are the probability density functions (PDF) (see next sections) for the three components, N is the sum of $N_S + N_{RD} + N_B$ and N_{obs} is the number of observed events in the analysis box region.

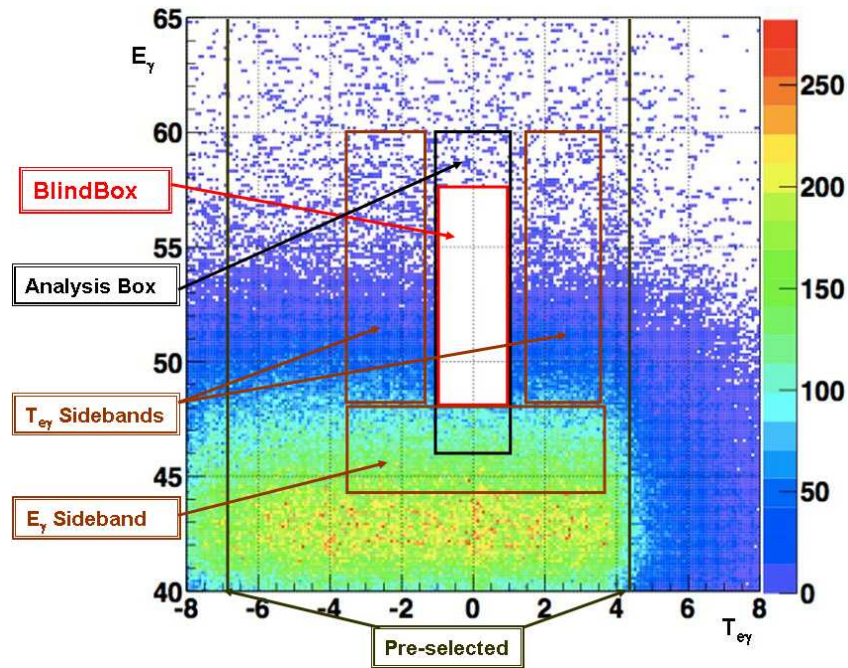


Figure 8.1: Preselection box, side bands, blind and analysis boxes in the $(T_{e\gamma}(\text{ns}), E_{\gamma}(\text{MeV}))$ -plane.

8.2.1 Signal PDF

The signal PDF, S , can be written as a product of statistically independent PDFs for the five variables:

$$S(E_{\gamma}, E_e, T_{e\gamma}, \theta_{e\gamma}, \phi_{e\gamma}) = S_1(E_{\gamma})S_2(E_e)S_3(T_{e\gamma})S_4(\theta_{e\gamma})S_5(\phi_{e\gamma}) \quad (8.2)$$

- $S_1(E_{\gamma})$ is extracted from 55 MeV γ events in the CEX run;
- $S_2(E_e)$ is a sum of three gaussian functions as measured in Michel events (see section 7.2);
- $S_3(T_{e\gamma})$ is a single gaussian function with the resolution measured from radiative decay events;
- $S_4(\theta_{e\gamma}), S_5(\phi_{e\gamma})$ are built with a toy Monte Carlo, computing the polar and azimuthal angle resolutions as combination of gamma position, positron emission angle and muon decay vertex resolutions.

Fig. 8.2 shows the PDFs for signal events.

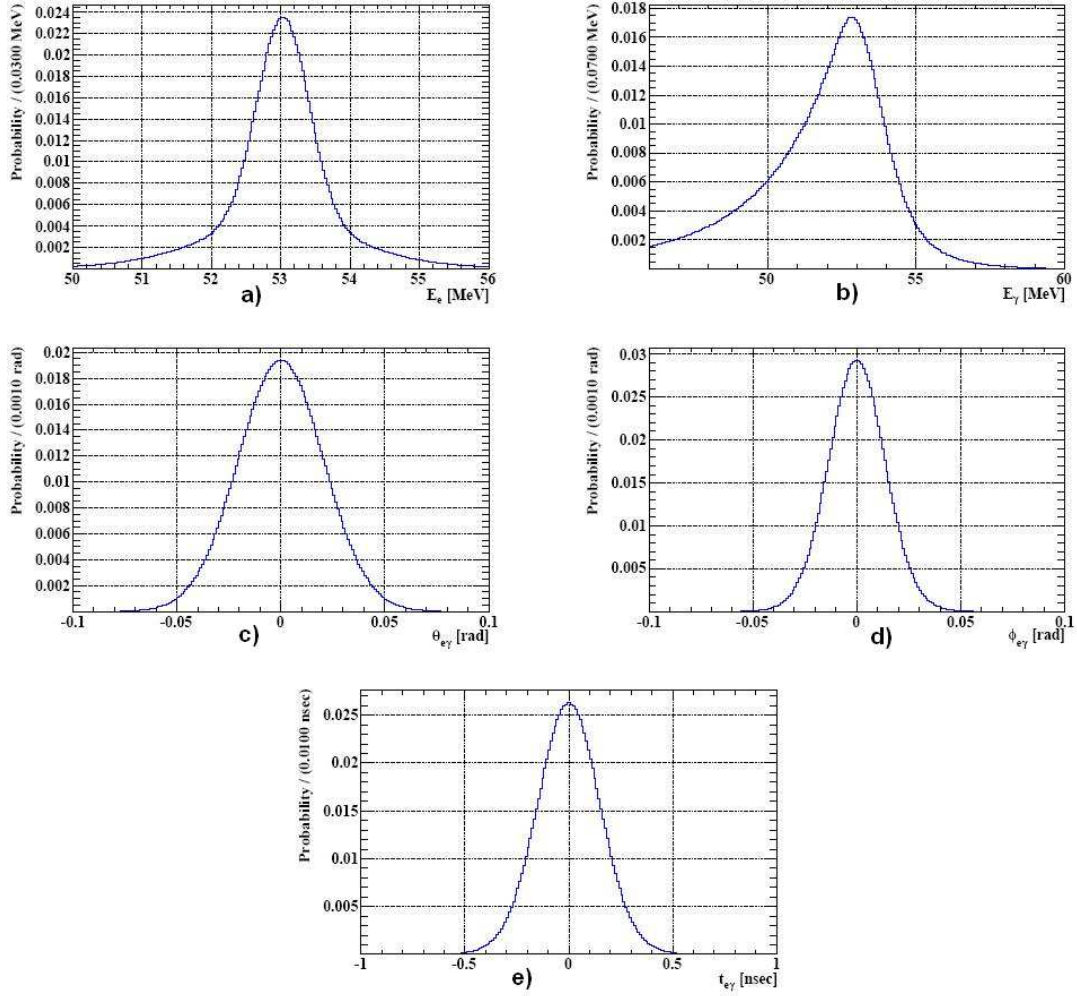


Figure 8.2: PDFs for signal events: a) positron energy; b) photon energy; c) relative angle $\theta_{e\gamma}$; d) relative angle $\phi_{e\gamma}$; e) relative time.

8.2.2 Radiative decay PDF

The radiative decay PDF, RD , is more complicated because the energy and spatial variables are correlated:

$$RD(E_\gamma, E_e, T_{e\gamma}, \Theta_{e\gamma}) = RD_1(E_\gamma, E_e, \theta_{e\gamma}, \phi_{e\gamma})RD_2(T_{e\gamma}) \quad (8.3)$$

- $RD_1(\mathbf{E}_\gamma, \mathbf{E}_e, \theta_{e\gamma}, \phi_{e\gamma})$ is a 4-dimensional function obtained from the Kuno-Okada theoretical spectrum [91], weighted with the detector acceptance and smeared with experimental resolutions;

- $\text{RD}_2(T_{e\gamma})$ is as the signal.

Fig.8.3 shows the PDFs for radiative decay events. The RD_1 PDF is projected on each of its four variables by integrating over the others.

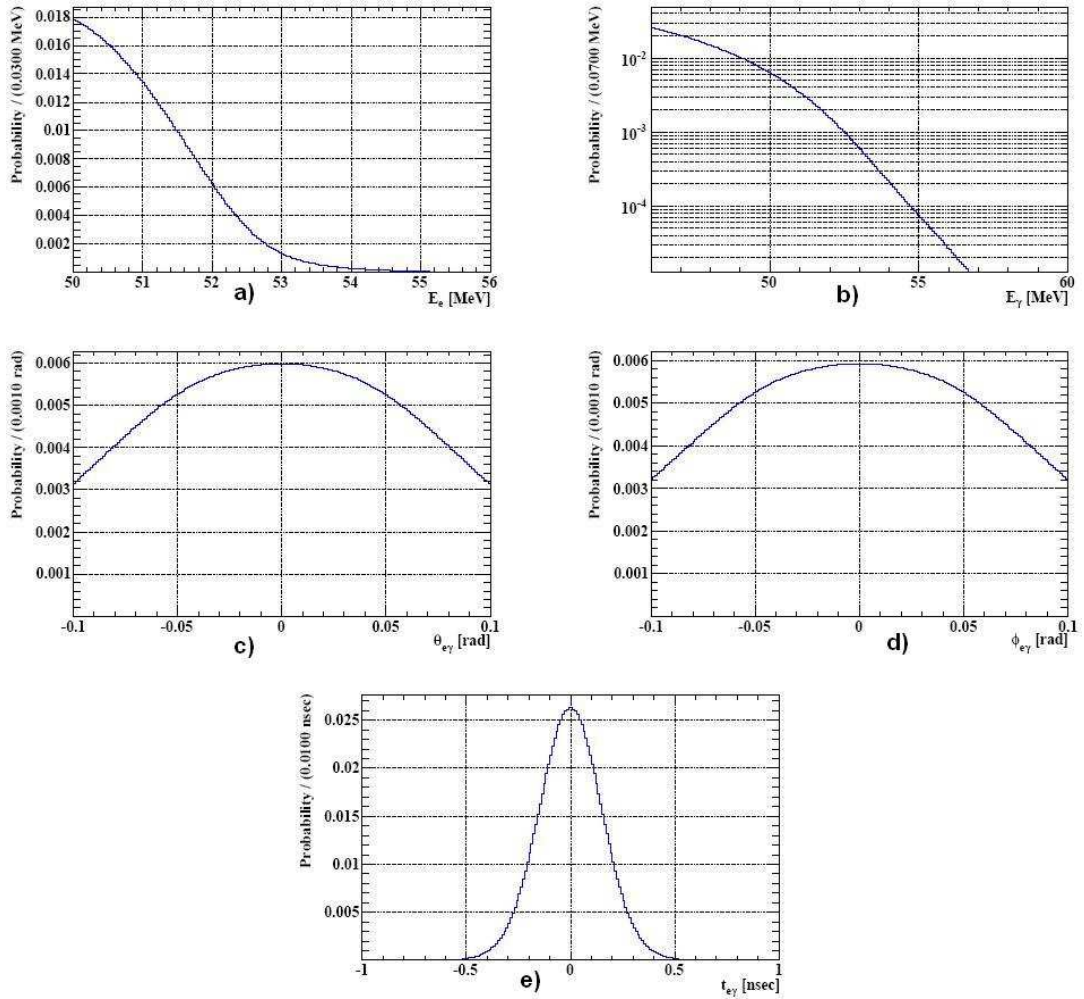


Figure 8.3: PDFs for radiative decay event: a) positron energy; b) photon energy; c) relative angle $\theta_{e\gamma}$; d) relative angle $\phi_{e\gamma}$; e) relative time. Energies and spatial variables are correlated.

8.2.3 Accidental background PDF

The accidental background PDF, B , is :

$$B(E_\gamma, E_e, T_{e\gamma}, \Theta_{e\gamma}) = B_1(E_\gamma)B_2(E_e)B_3(T_{e\gamma})B_4(\theta_{e\gamma})B_5(\phi_{e\gamma}) \quad (8.4)$$

Window	N_{obs}	Fit Values (N_S, N_{RD}, N_{BG})
Right Sideband	1197	$(1.6^{+3.4}, 26_{-16}^{+17}, 1169_{-37}^{+38})$
Left Sideband	1209	$(0^{+1.2}, 9.6^{+16}, 1199_{-38}^{+38})$
Blind Box	1189	$(4.3_{-2.9}^{+3.9}, 25_{-16}^{+17}, 1159_{-37}^{+38})$

Table 8.1: N_S , N_{RD} , N_{BG} from likelihood fit in the analysis box and in the side-bands.

- $\mathbf{B}_1(\mathbf{E}_\gamma)$ is an empirical function, fitted in the sidebands. The function is polynomial below a boundary value and an exponential shape, which describes the residual pileup, above it;
- $\mathbf{B}_2(\mathbf{E}_e)$. It is the theoretical Michel spectrum multiplied by the acceptance and convoluted with the resolution; it is obtained by a fit in the sidebands;
- $\mathbf{B}_3(\mathbf{T}_{e\gamma})$. Since the positron and gamma are uncorrelated, we obtained the $T_{e\gamma}$ PDF by fitting a flat distribution in the analysis box;
- $\mathbf{B}_4(\theta_{e\gamma}), \mathbf{B}_5(\phi_{e\gamma})$ are third order polynomials fit on sideband events.

Fig.8.4 shows the PDFs for accidental background events.

8.3 Likelihood fit results

Before opening the box, we applied the analysis cuts and performed the likelihood fit in the side-bands. We do not expect any signal or radiative events in these windows, so a likelihood fit in those intervals is an estimate of our sensitivity and a check of the fitting algorithm. We then opened the blind box and 1189 events survived the analysis cuts. Table 8.3 gives the results of likelihood fit in the analysis box and in the side-bands. Fig. 8.5 shows the result of the fit for the five variables in the blind box.

8.4 Confidence interval

In order to compute a 90% Confidence interval (CL) we followed the Feldmann-Cousins (F.C.) approach [92]:

- we chose a point in the (N_S^j, N_{RD}^j, N_B^j) -space, where N_B^j and N_{RD}^j are poissonian fluctuations of expected values extracted from the sidebands (N_{RD}^{exp}, N_B^{exp}), and N_S^j is the number of signal events ranging 0 to 20 (we scan all the values in a conservative interval);

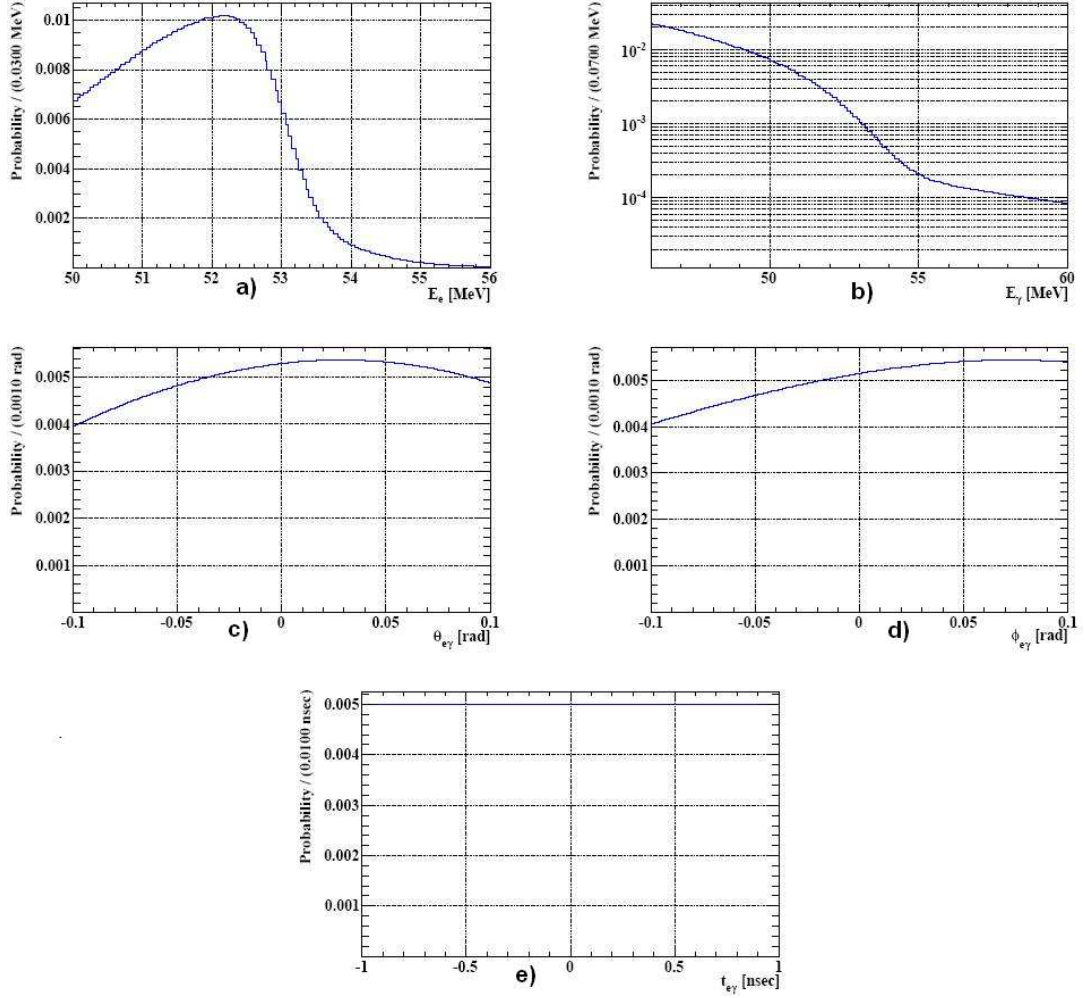


Figure 8.4: PDFs for accidental background event: a) positron energy; b) photon energy; c) relative angle $\theta_{e\gamma}$; d) relative angle $\phi_{e\gamma}$; e) relative time.

- we generated N_S^j signal, N_{RD}^j radiative and N_B^j background events in the analysis region (or in the sidebands by sampling the corresponding PDFs);
- we repeated the last point for 10^3 simulated experiments, with N_B^j and N_{RD}^j always poissonian fluctuations of expected values from the sidebands and N_S^j fixed in the first stage. For each experiment we calculated the F.C. likelihood ratio:

$$R(MC) = \frac{\mathcal{L}_{MC}(N_S^j, N_{RD}^j, N_B^j)}{\mathcal{L}_{MC}(best)} \quad (8.5)$$

and obtain the distribution of R ;

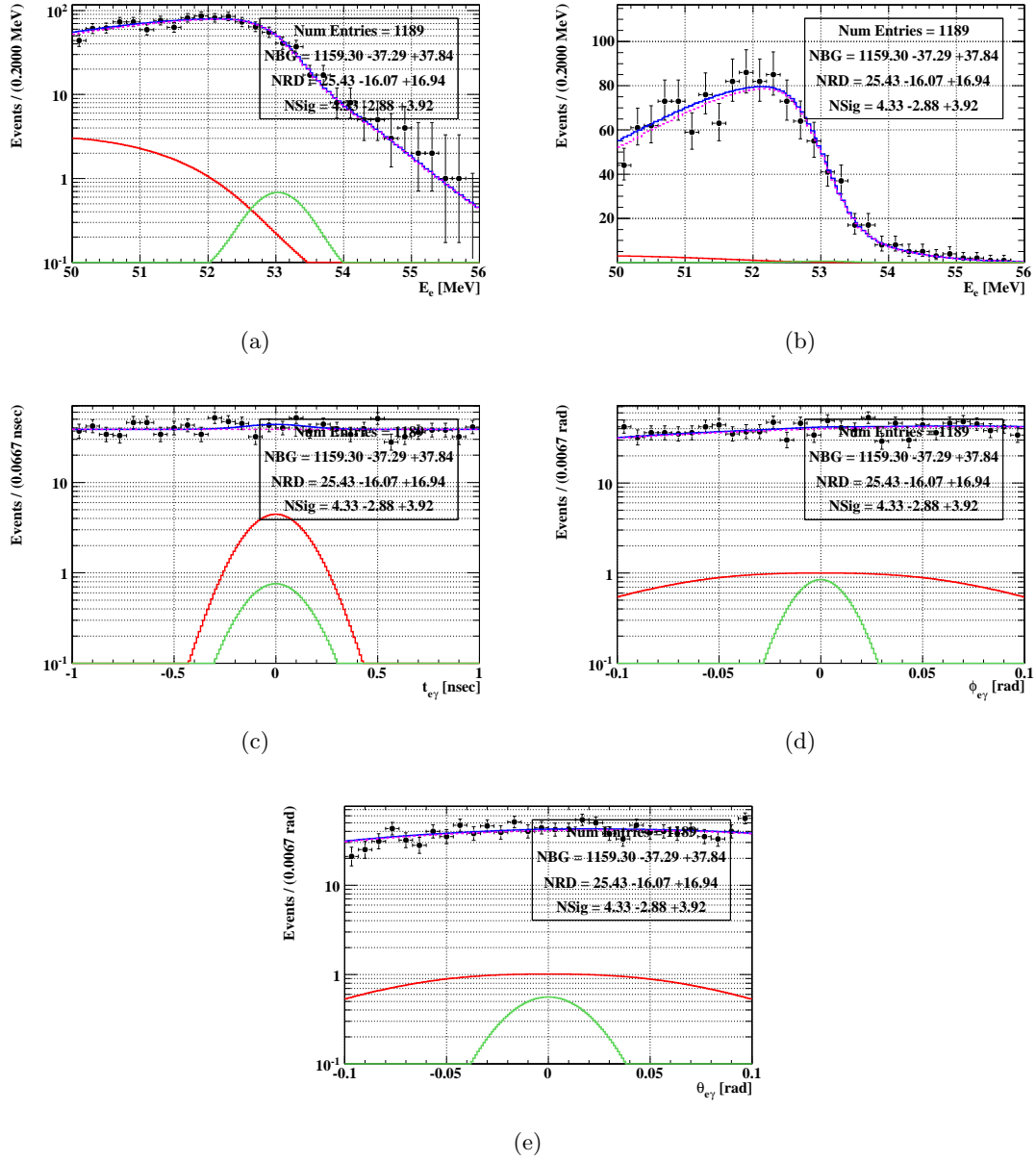


Figure 8.5: Data distribution superimposed with the S (green line), R (red line) and B (light purple) PDFs resulting from the Likelihood fit: (a) E_γ distribution, (b) E_e , (c) $\Delta T_{e\gamma}$, (d) $\phi_{e\gamma}$ and (e) $\theta_{e\gamma}$.

- we computed the ratio $R(data)$ at the point $(N_S^j, N_{RD}^{exp}, N_B^{exp})$ as

$$R(data) = \frac{\mathcal{L}(N_S^j, N_{RD}^{exp}, N_B^{exp})}{\mathcal{L}(best)} \quad (8.6)$$

where $\mathcal{L}(best)$ is the maximum value of likelihood from the fit to the data. It is important to note that there is a constraint on physically allowed region ($N_S \geq 0, N_{RD} \geq 0, N_B \geq 0$). If $R(MC)$ is smaller than $R(data)$ in at least 90% of the cases, the point N_S^j is in the 90% C.L. band; if $R(MC)$ is higher than $R(data)$ in at most 10% of the cases, N_S^j is out of 90% C.L. band.

We repeated this procedure for all values of N_S^j . The value 0 is included in the band and the upper limit is:

$$N_s \leq 14.7 @ 90\% C.L. \quad (8.7)$$

8.5 Normalization

The number of $\mu \rightarrow e\gamma$ events is given by:

$$N_{\mu e\gamma} = R_\mu \cdot T \cdot BR(\mu e\gamma) \cdot A_{e\gamma}^{DCH} \cdot \varepsilon_{e\gamma}^{TC-DC} \cdot (A_{e\gamma}^{XEC} | A_{e\gamma}^{DCH}) \cdot \varepsilon_{e\gamma}^{DCH} \cdot \varepsilon_{e\gamma}^{XEC} \cdot \varepsilon_{e\gamma}^{Trg} \quad (8.8)$$

where

- R_μ is the rate of stopping muons in the target;
- T is the live time;
- $BR(\mu e\gamma)$ is the branching ratio of $\mu e\gamma$ decay;
- $A_{e\gamma}^{DCH}$ is the positron geometrical acceptance of the drift chambers;
- $\varepsilon_{e\gamma}^{TC-DC}$ is the DCH-TIC matching efficiency ;
- $(A_{e\gamma}^{XEC} | A_{e\gamma}^{DCH})$ is the probability that the gamma ray from $\mu \rightarrow e\gamma$ decay is detected in the calorimeter fiducial volume when the accompanied positron is detected in the DCH acceptance;
- $\varepsilon_{e\gamma}^{DCH}$ is the tracking efficiency, including the selection criteria;
- $\varepsilon_{e\gamma}^{XEC}$ is gamma-ray detector and reconstruction efficiency, including selection criteria;

- $\varepsilon_{e\gamma}^{Trg}$ is the $\mu \rightarrow e\gamma$ trigger efficiency.

Merging together all the terms in a single normalization term k , we can write:

$$BR(\mu e\gamma) = \frac{N_{\mu e\gamma}}{k}. \quad (8.9)$$

For a direct measurement of the normalization factor a precise knowledge of all of the parameters is mandatory. In run 2008 the computation of all factors related to the positron was very difficult, since the working conditions of the drift chambers were drastically changing with time. In order to compute the branching ratio in a way nearly insensitive to the positron acceptance and efficiency factors, we developed an alternative method by using the Michel positrons collected simultaneously, during MEG runs, with the same analysis cuts. Using the TC alone trigger data mixed in the physics data taking as Michel data sample, we can write an analogous formula:

$$N_{\mu e\nu\bar{\nu}} = R_{\mu} \cdot T \cdot BR(\mu e\nu\bar{\nu}) \cdot f_{e\nu\bar{\nu}} \cdot P_{e\nu\bar{\nu}}^{Trg} \cdot A_{e\nu\bar{\nu}}^{DCH} \cdot \varepsilon_{e\nu\bar{\nu}}^{TC-DC} \cdot \varepsilon_{e\nu\bar{\nu}}^{DCH} \cdot \varepsilon_{e\nu\bar{\nu}}^{Trg} \quad (8.10)$$

where

- R_{μ} and T are the same as for signal;
- $BR(\mu e\nu\bar{\nu})$ is the branching ratio of Michel decay;
- $f_{e\nu\bar{\nu}}$ is the fraction of Michel spectrum above 50 MeV (analysis cut);
- $P_{e\nu\bar{\nu}}^{Trg}$ is the inverse of the pre-scale factor of TIC self-trigger;
- $A_{e\nu\bar{\nu}}^{DCH}$, $\varepsilon_{e\nu\bar{\nu}}^{TC-DC}$, $\varepsilon_{e\nu\bar{\nu}}^{DCH}$ and $\varepsilon_{e\nu\bar{\nu}}^{Trg}$ are the Michel decay equivalent of the previous ones.

By taking the ration of 8.8 and 8.10, we obtain:

$$\frac{BR(\mu e\gamma)}{BR(\mu e\nu\bar{\nu})} = \frac{N_{\mu e\gamma}}{N_{\mu e\nu\bar{\nu}}} \cdot f_{e\nu\bar{\nu}} \cdot P_{e\nu\bar{\nu}}^{Trg} \cdot \frac{A_{e\nu\bar{\nu}}^{DCH}}{A_{e\gamma}^{DCH}} \cdot \frac{\varepsilon_{e\nu\bar{\nu}}^{TC-DC}}{\varepsilon_{e\gamma}^{TC-DC}} \cdot \frac{\varepsilon_{e\nu\bar{\nu}}^{DCH}}{\varepsilon_{e\gamma}^{DCH}} \cdot \frac{\varepsilon_{e\nu\bar{\nu}}^{Trg}}{\varepsilon_{e\gamma}^{Trg}} \cdot \frac{1}{(A_{e\gamma}^{XEC}|A_{e\gamma}^{DCH})} \cdot \frac{1}{\varepsilon_{e\gamma}^{XEC}} \quad (8.11)$$

- $BR(\mu e\nu\bar{\nu})$. The Michel branching ratio is ≈ 1 because for the muon it nearly saturates the total decay rate.
- $N_{\mu e\nu\bar{\nu}}$. The number of detected Michel positrons in the analysis range is 11414.
- $f_{e\nu\bar{\nu}}$. The fraction of Michel spectrum included in the analysis range is computed to be 0.101 ± 0.006 by integrating the theoretical spectrum.

- $\mathbf{P}_{e\nu\bar{\nu}}$. The pre-scale factor of TC alone trigger is 10^{-7} . For the $\mu e\gamma$ trigger is 1.
- $\mathbf{A}_{e\nu\bar{\nu}}^{\text{DCH}}/\mathbf{A}_{e\gamma}^{\text{DCH}}$. The ratio of drift chamber geometrical acceptances is 1. Differences in acceptance due to different energy of Michel and signal events are included in the reconstruction efficiency ratio.
- $\varepsilon_{e\gamma}^{\text{TC-DC}}/\varepsilon_{e\nu\bar{\nu}}^{\text{TC-DC}}$. DCH-TIC matching efficiency ratio: it is calculated using the DCH-self trigger data. It is evaluated as a function of positron momentum. The ratio is 1.11 ± 0.02 by comparing the value at end point of Michel spectrum with that obtained by averaging above 50 MeV.
- $\varepsilon_{e\gamma}^{\text{DCH}}/\varepsilon_{e\nu\bar{\nu}}^{\text{DCH}}$. The tracking efficiency ratio is calculated using random trigger data samples. The ratio of detected events to the full Michel spectrum is calculated as a function of positron momentum. The efficiency ratio is 1.020 ± 0.005 by comparing the value at end-point of the Michel spectrum with that obtained by integrating above 50 MeV.
- $\varepsilon_{e\gamma}^{\text{Trg}}/\varepsilon_{e\nu\bar{\nu}}^{\text{Trg}}$. The efficiency of MEG signal trigger is discussed in section 7.5.2. We need to evaluate the TC alone trigger efficiency. An unbiased sample of events were acquired with DC-Alone trigger, which requires that at least 4 out of 5 consecutive DC modules are hit. The TC signals are not used at all. The entire TC waveforms are recorded for these events. The collected events are reconstructed and a subsample of positrons tracks matching a TC hit is derived. On this subsample of positrons hitting the TC, the presence of TC alone trigger is searched for. The number of events in which the TC alone trigger is fired divided by the total number of events in the subsample is the online selection efficiency. Thus $\varepsilon_{e\nu\bar{\nu}}^{\text{Trg}}$ is measured to be $97.3\% \pm 0.6\%$. The ratio is 0.66 ± 0.03 .
- $(\mathbf{A}_{e\gamma}^{\text{XEC}}|\mathbf{A}_{e\gamma}^{\text{DCH}})$. The gamma-ray acceptance is the fraction of signal photons that enter into the calorimeter when the accompanied positron is detected in the DCH acceptance. It is evaluated by MC simulation using measured angle and position resolutions. It is 0.98 ± 0.005 .
- $\varepsilon_{e\gamma}^{\text{XEC}}$. The gamma ray efficiency is 0.63 ± 0.04 (see section 6.8).

Multiplying all the factors we obtain the normalization factor:

$$k = (5.2 \pm 0.5) \times 10^{11}. \quad (8.12)$$

8.6 Result and 2008 sensitivity

The fit result is zero-consistent, so an upper limit on $\mu \rightarrow e\gamma$ is given. Using the normalization factor k from section 8.5 the upper limit is:

$$BR(\mu \rightarrow e\gamma) < 2.8 \times 10^{-11} \text{ @ 90\% C.L.} \quad (8.13)$$

The sensitivity is the 90% C.L. upper limit in absence of signal. It describes the accuracy of the experiment, and is independent of the data fluctuations. We define the 90%-confidence level sensitivity, as the average 90 % C.L. upper limit over the ensemble of the simulated toy experiments with $N_{RD} = 25$, $N_B = 1159$ and $N_s = 0$. Fig. 8.6 shows the distribution of N_s 90% C.L. upper limits for 10^3 toy experiments. The mean value of the distribution is at 6.5, so the branching-ratio sensitivity of run 2008 is calculated to be 1.3×10^{-11} , comparable with the limit set by MEGA experiment. It is important to note that the probability to obtain an upper limit greater than 2.8×10^{-11} is $\approx 5\%$, if systematic uncertainties are taken into account in the analysis.

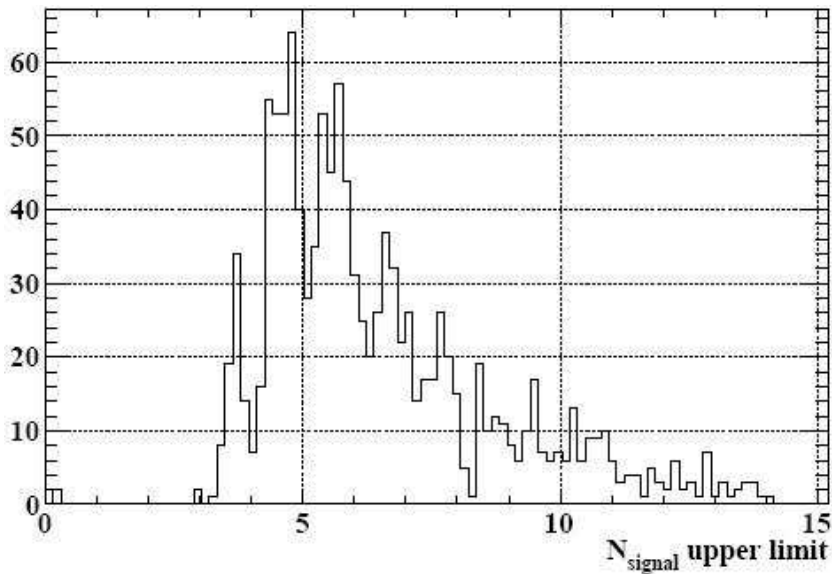


Figure 8.6: Distribution of 90% upper limits of toy experiments.

Chapter 9

First results from 2009 run

2009 run was the second physics run of the MEG experiment; it started on 29 October and ended on December 22. During the 2008-2009 shutdown period the trip problem with the DCs was identified and solved, all DCs were modified and have since been successfully in operation throughout the 2009 run (figure 9.1). This increased the positron detector efficiency (including TC-DC matching) from $\approx 15\%$ of 2008 run to $\approx 40\%$ of 2009 run. Thus, despite the 2009 data taking last only half with respect to the 2008 one, the statistics collected was in total twice much. Meanwhile the xenon was also purified during the shutdown period by using a series of purification cartridges and a new purification pump was installed (see next section). This resulted in a 45% increase in light yield compared to 2008 and led to a more stable detector. The front-end electronics read-out boards were also upgraded with a new version of the digitizing chip (DRS4) which doubles the linearity range and eliminates unwanted “ghost” pulses. The first sections of this chapter will show the new xenon purification and a summary of detector performances in 2009 run. We will end showing a preliminary analysis result.

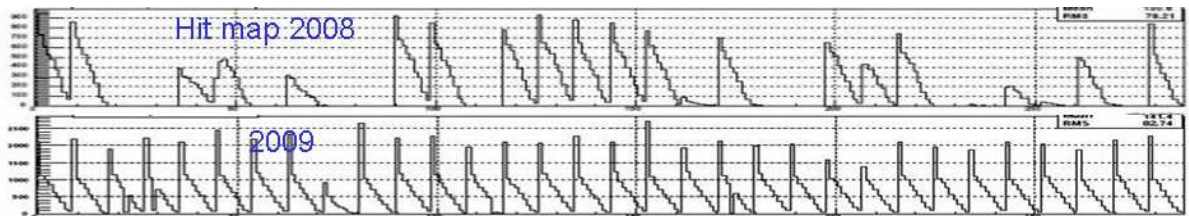


Figure 9.1: Comparison of drift chambers hitmaps of 2008 and 2009 runs: each plot is related to a chamber plane (half of chamber).

9.1 Liquid xenon purification

During the 2008 data taking run, the light yield increased and had two different behaviors for α -sources and Lithium peak: at the end of the run, the α -peak was stable while the Lithium peak continued to increase (see section 6.3). We interpreted this as the presence of quenching impurities that influence in different ways the two sources. In order to remove all contaminants, at the end of 2008 run, Xenon was recovered to gas storage tanks through the gaseous phase purification cartridge, more effective on electronegative impurities. At the beginning of August 2009, a new circulation pump and a new cartridge, able to remove electro-negative impurities also in liquid phase, were installed. In addition, circulation speed was increased (≈ 180 l/hour with respect to ≈ 35 l/hour) and the pump worked at ≈ 60 cycles per minute without inducing noise on the detectors making possible to perform liquid phase purification also during data taking. Figure 9.2 shows the new system. After a short period of liquid purification (≈ 45 hours) at the start of the data taking, the light yield reached the plateau both in α and Lithium peaks. Figure 9.3 shows the history of Lithium peak and three different α -sources: the light yield was stable at 1%. It is important to note that Lithium peak N_{phe} increased by $\approx 45\%$ (from 22000 to 32000) reaching the value expected. The improvement to the purification influenced also the waveform τ : figure 9.4 shows the comparison of the γ -waveforms between 2008 and 2009 data taking with both the digitizers. Figure 9.5 shows the comparison of the waveform τ for α and Lithium events for 2008 and 2009 runs: α waveform tau remained stable while γ waveform tau increased until 45 ns as expected. This behavior confirms the hypothesis of electronegative impurities in xenon during the 2008 run.

9.2 Performances of detectors

During the 2009 run all monitoring and calibration devices were operational. By means of LEDs and α -sources immersed in the liquid xenon, daily calibrations of the calorimeter photomultipliers were performed. The xenon detector energy scale and resolutions were measured over the energy range of 4 MeV to 129 MeV using γ s from radioactive sources, from a dedicated Cockcroft-Walton accelerator (weekly), and charge exchange and radiative capture reactions (at the beginning of the data taking). Timing counter performances were measured using Michel positron and CW boron dedicated runs. Drift chambers angular and energy resolutions were measured using Michel positrons and the two full turn track method described in section 7.2. Due to the fully operational spectrometer drift chambers and to an improvement of DC

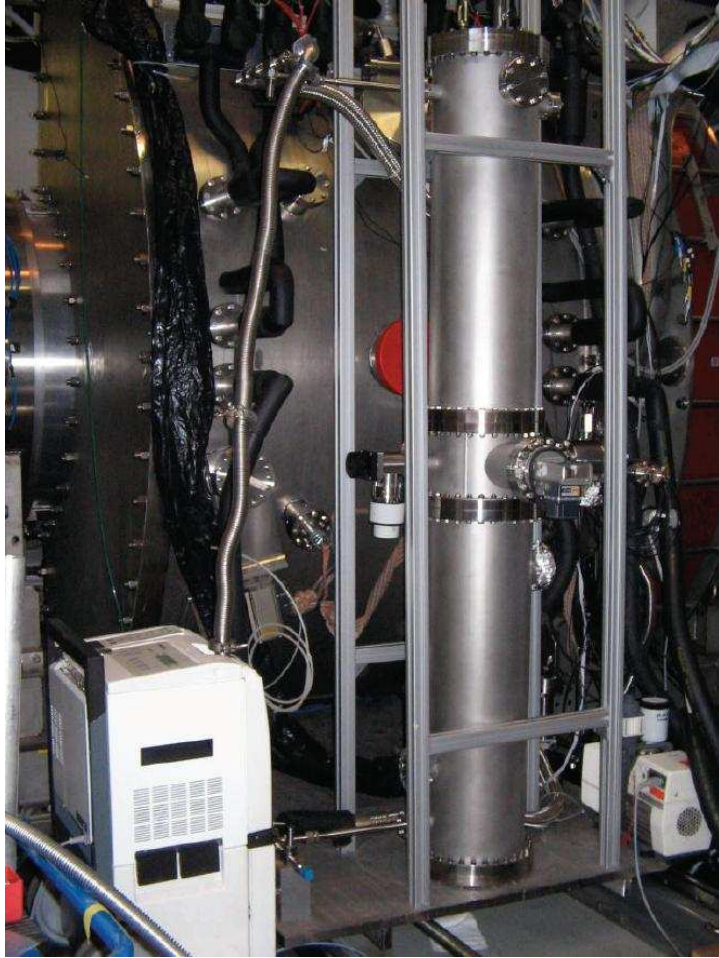


Figure 9.2: The new liquid xenon purification system.

analysis software, we obtained a large increase of positron angular and energy resolutions. The positron energy resolution is well described by a double Gaussian function (with respect to a triple gaussian used in 2008 run) with resolutions of 0.39MeV and 1.71MeV for the core (79%) and tail (21%) components, respectively. The positron angular resolutions are evaluated by the two-turn method to be $\sigma_{\theta_e} = 11.2$ mrad and $\sigma_{\phi_e} = 7.4$ mrad. The improvement in the purification system, and the consequent scintillation light increasing, slightly improved the γ energy and position resolution: average $\sigma_{E_\gamma} = 5\%$ FWHM for events with $w > 2$ cm (6.6% for $1 < w < 2$ cm and 7.8% for $0 < w < 1$ cm), $\sigma_u \approx 5$ mm, $\sigma_v \approx 5$ mm and $\sigma_w \approx 6$ mm. There was not significant improvement in timing resolution for TC and calorimeter due to an unexpected problem in the synchronization between DRS4 chips in different VME boards. It

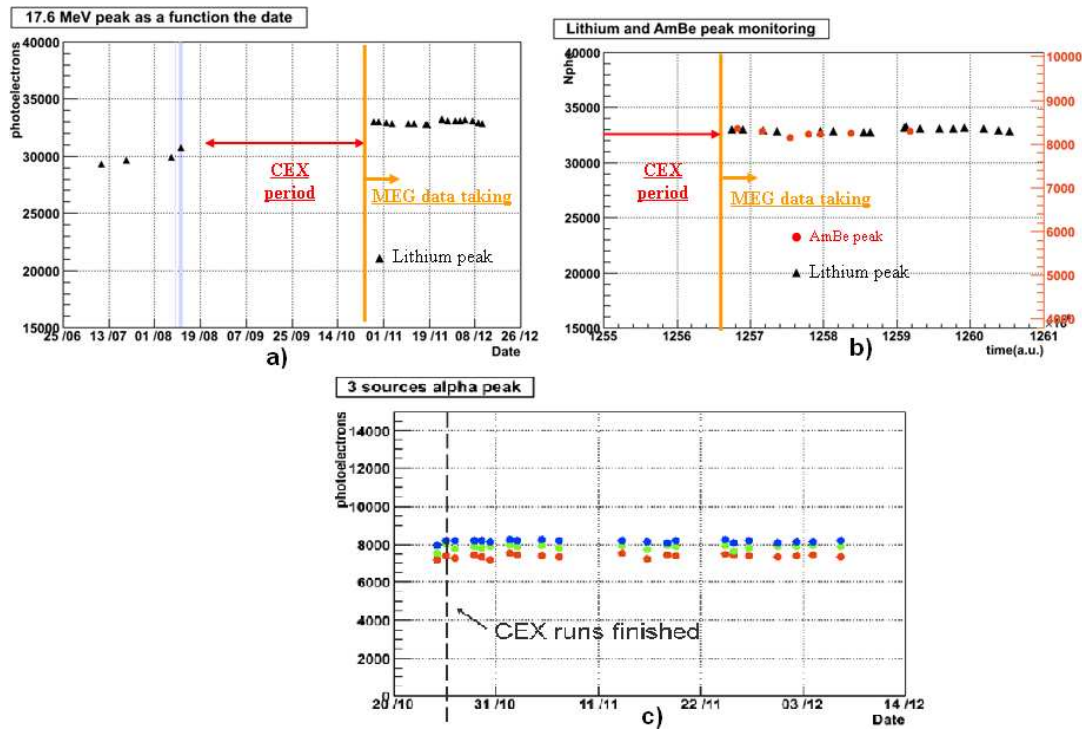


Figure 9.3: N_{phe} for Lithium peak (picture a and b) and the peaks of three alpha sources (picture c) as function of the time to monitor xenon purification. In the picture b (zoom of last region of picture a) the red dots are the 4.4 MeV γ s from AmBe source.

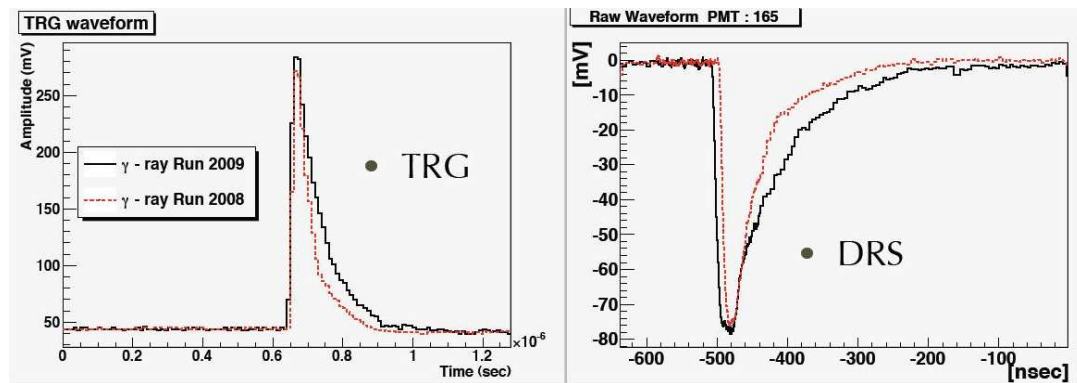


Figure 9.4: γ waveform tau comparison between 2008 and 2009: left, trigger digitizer; right, DRS digitizer.

has now been solved in the 2010 data taking run. For the combined detector, the resolutions for the relative angle measurements are estimated to be 14.7 mrad and 12.7 mrad for $\theta_{e\gamma}$ and

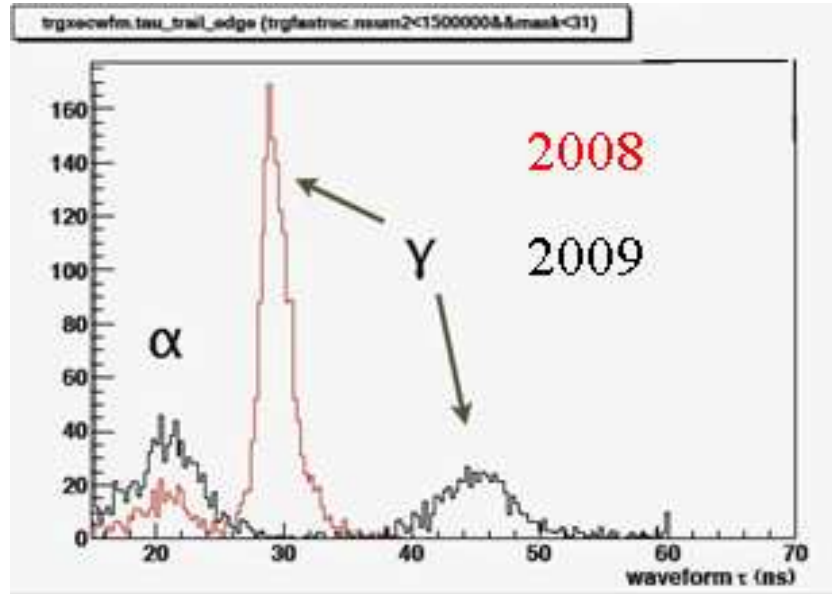


Figure 9.5: Comparison of the waveform τ for α and Lithium events for 2008 and 2009 runs.

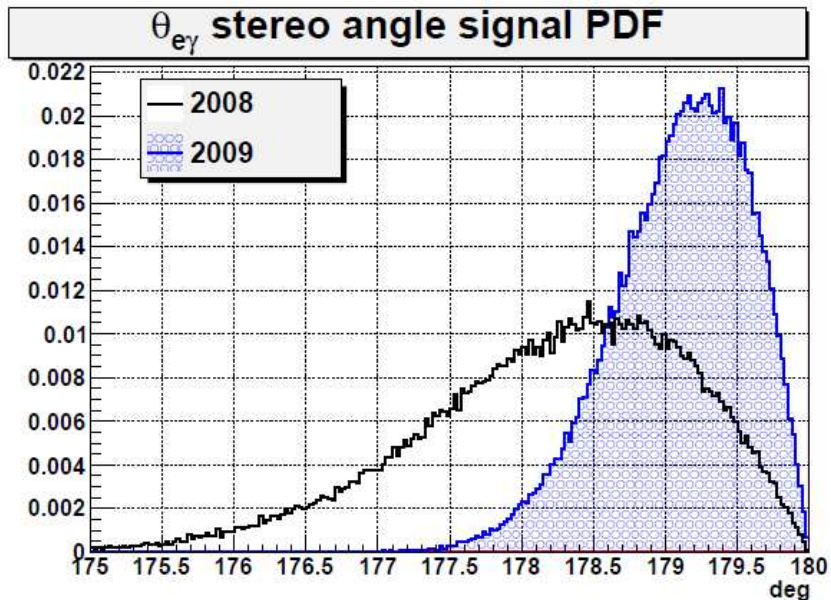
$\phi_{e\gamma}$, respectively. Figure 9.6 shows the clearly improvement of stereo angle ($\Theta_{e\gamma}$) signal PDF with respect to 2008. The relative time resolution at the signal energy is estimated to be 142 ps from the spread of the radiative decay peak observed in the energy sideband in the physics data with a small correction that takes into account a dependence on γ -energy measured in the CEX calibration runs. Figure 9.7 shows the radiative decay peak. The experience of the run 2008 leads to an improvement of the trigger efficiency up to 85.4%. The extreme stability of the LXe light yield allows us to increase the E_γ threshold up to 44 MeV, improving the livetime and DAQ efficiency of the experiment. Table 9.1 summarizes analysis variables resolutions with respect to 2008.

9.3 Preliminary result of 2009 data analysis

A procedure similar to that employed for 2008 data was performed on the physics data taken in 2009. We performed a pre-selection on collected data and then a stricter selection dividing the survived events in four groups (analysis box, time and energy sidebands) (see chapter 8). Events in the analysis region are saved in separate hidden files and unblinded after calibrations, optimization of the analysis algorithms and background study in the sidebands are completed. The normalization factor was evaluated from the number of Michel-positrons, with a procedure

Variables	RUN 2008	RUN 2009
E_γ	5.8% (FWHM)	5.0% (FWHM)
E_e	3.5% (FWHM)	1.75% (FWHM)
$\theta_{e\gamma}$	21 mrad	14.7 mrad
$\phi_{e\gamma}$	14 mrad	12.7 mrad
$T_{e\gamma}$	350 ps (FWHM)	335 ps (FWHM)
ϵ_{Trg}	66%	84.5%

Table 9.1: Analysis parameters comparison between 2008 and 2009.

Figure 9.6: Stereo $\Theta_{e\gamma}$ signal PDF in 2008 (black plain) and 2009 (blue filled).

equal to that employed for 2008 data. It was estimated to be:

$$k = 9.9 \pm 0.2 \times 10^{11} \quad (9.1)$$

As in 2008, the sensitivity of the experiment with a null signal hypothesis is evaluated by averaging the upper limit on the branching fraction over an ensemble of simulated experiments by means of a toy MC simulation based on the likelihood function. The rates of radiative decay and accidental background events, as measured in the side-bands, are assumed in each simulated experiment and the upper limit is calculated using the likelihood ratio ordering

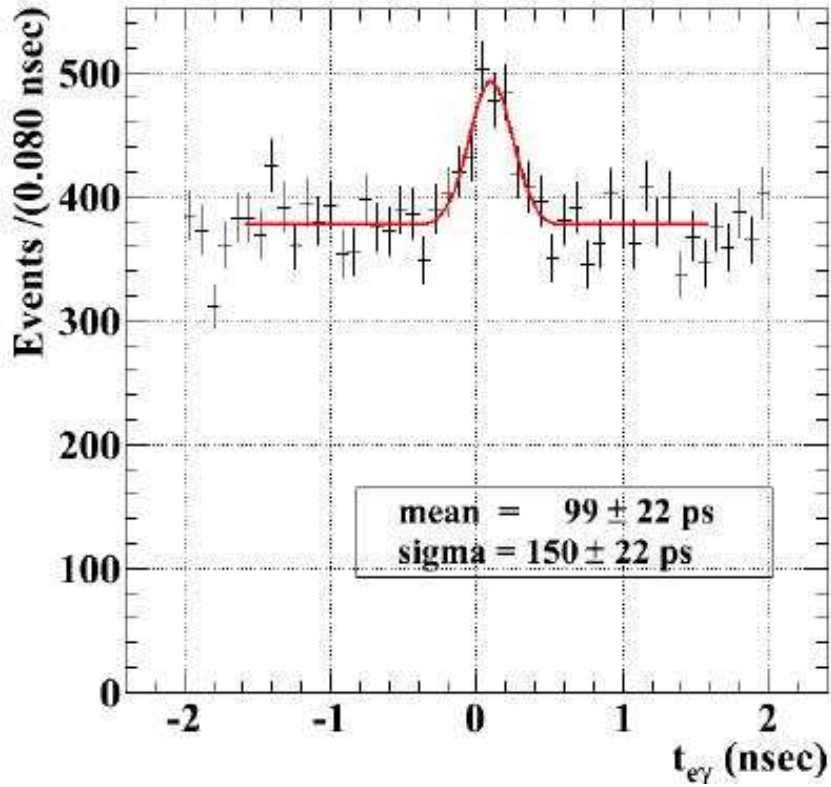
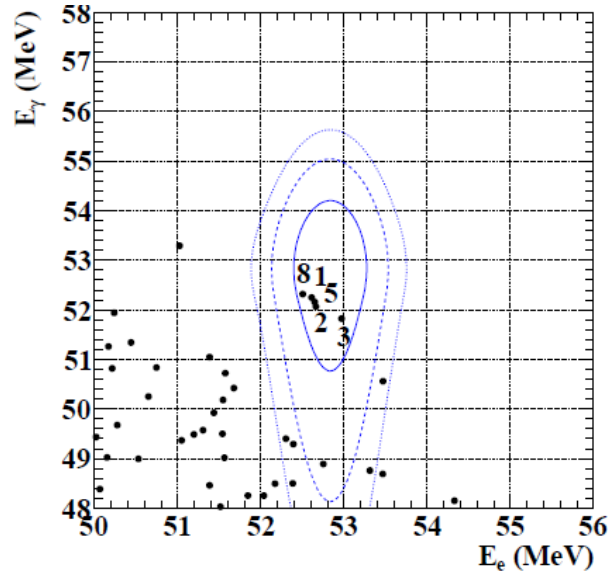


Figure 9.7: The relative time distribution $T_{e\gamma}$ showing the radiative decay peak obtained during physics runs, for $40 < E_\gamma < 45$ MeV.

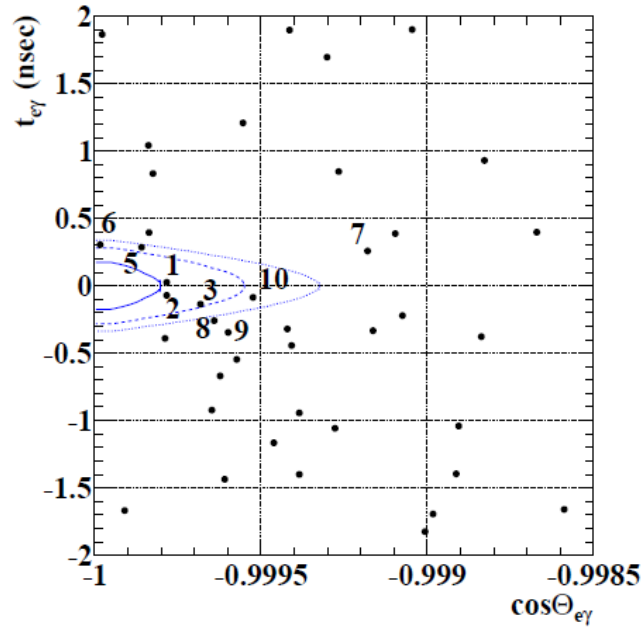
principle The branching fraction sensitivity at 90% C.L. is thus obtained to be 6.1×10^{-12} , using the calculated normalization factor. The obtained sensitivity is consistent with the upper limits of $(4-6) \times 10^{-12}$ obtained by likelihood fits in several comparable analysis windows in the $T_{e\gamma}$ side-bands. Figure 9.8 shows the distribution of the events around the signal region projected in the (E_e, E_γ) and $(\cos \Theta_{e\gamma}, T_{e\gamma})$ planes. The contours of the signal PDF are also drawn and the same events in the two plots are numbered correspondingly. The quality of the events was thoroughly checked. All the events are uniformly distributed in both time and detector acceptance. The detector was in good condition when all events were recorded. One to two background events are expected to fall around this signal region according to the background rate evaluated in the side-bands. The best estimates from the maximum likelihood fit to the $N_{obs} = 370$ events observed in the analysis window are $N_S = 3.0$ and $N_{rad} = 35_{-22}^{+24}$. The best estimate of N_{rad} is consistent with the expectation from sidebands. The 90% C.L. upper limit

for N_S is calculated to be 14.52, with $N_{\text{sig}} = 0$ inside the 90% confidence interval. The related BR upper limit is:

$$BR(\mu \rightarrow e\gamma) < 1.5 \times 10^{-11} \text{ at 90\% C.L.} \quad (9.2)$$



(a)



(b)

Figure 9.8: Event distribution in (a) (E_e, E_γ) -plane and (b) $(\cos \Theta_{e\gamma}, T_{e\gamma})$ -plane around the signal region. The contours of the PDFs (1-, 1.64- and 2- σ) are shown and the same events in the two plots are numbered correspondingly.

Conclusion

The MEG experiment at PSI searches for the muon decay in one electron plus a photon ($\mu \rightarrow e + \gamma$) with a sensitivity around 10^{-13} , aiming therefore at improving the present best experimental limit by two orders of magnitude.

In order to reach this goal, the experiment uses the most intense continuous beam available and aims at reaching optimal energy, time and space resolutions for both particles (photon and positron) detection.

In particular for the photon kinematic variables, a new kind of large acceptance, large mass (roughly 2.2 Tons) detector based on liquid xenon scintillation light was developed. In this thesis particular attention is devoted to the liquid xenon calorimeter, its structure and operation. The MEG experiment is operative since 2007, while the first physics data taking period started on September 12th and ended on December 22th 2008. During 2008 run several complementary and redundant calibration methods were operative to monitor the calorimeter. The LXe detector suffered during this period from light yield instability: purity was increased during the run slightly modifying the response of the detector. Despite this problem, the photon detector confirmed its capability as a superior gamma-ray detector with unprecedented energy, position and time resolutions. Other issues affected the MEG 2008 run: the DC system suffered from several HV trips leading to a loss in the tracking reconstruction capability and the trigger efficiency ($\approx 66\%$) was less than the expected one due to a problem on the direction match lookup table.

The effective running time was around 50 days corresponding to 9.5×10^{13} muons stopped on target corresponding to a sensitivity of 1.3×10^{-11} . By performing a blind likelihood analysis, we were able to give an upper limit on the branching ratio $\text{BR}(\mu \rightarrow e\gamma) < 2.8 \times 10^{-11}$ (90% C.L.), comparable to the current best limit, coming from the MEGA experiment (1.2×10^{-11}). The 2009 run was the second MEG physics run; it started on 29th October and ended on December 22th. During the 2008-2009 shutdown period the trip problem with the DCs was

identified and solved, all DCs were modified and have since then been in operation throughout the 2009 run with no mayor problems. Thus, despite the 2009 data taking lasted only one half of the 2008 one, the statistics collected was in total twice. Meanwhile xenon was also purified during the shutdown period by using a series of purification cartridges and a new purification pump. This resulted in a 45% increase in light yield compared to 2008 and led to a more stable detector. The front-end electronics read-out boards were also upgraded with a new version of the digitizing chip (DRS4) which doubles the linearity range and eliminates unwanted “ghost” pulses. The trigger direction match lookup table was updated reaching a trigger efficiency $\approx 85.4\%$. Due to an unexpected problem in the synchronization between DRS4 chips in different VME boards, the timing resolution did not improve as expected. An analysis procedure similar to 2008 was performed on the physics data taken in 2009 reaching a sensitivity of 6.1×10^{-12} , and giving a preliminary result of $BR(\mu \rightarrow e\gamma) < 1.5 \times 10^{-11}$ at 90% C.L.

The MEG experiment will collect data until the year 2012 to reach the sensitivity goal. In 2010 run two new calibrations systems were installed. A neutron generator is used to induce neutron capture on Ni followed by the emission of 9 MeV photons for the calorimeter calibration. The 9 MeV line is the only possibility for having a physical γ -line in the physics data taking condition. A mobile polyethylene target was installed inside the apparatus in order to obtain monochromatic elastic Mott scattered positrons with a dedicated positron beam. This calibration can be used to better measure the tracker momentum resolution and study efficiency and systematic uncertainties in the positron track reconstruction.

Two major hardware upgrades are also foreseen: the TC fiber signals will be introduced both in the trigger system and in the offline reconstruction. This will lead to a further improvement in the DAQ efficiency and in the analysis adding a refined measurement of the positron impact point in the TC detector. The DRS chip synchronization problem has been solved and a substantial improvement in the timing resolution is therefore expected. Finally a multiple buffer read out scheme will be implemented in the DAQ leading to a dramatic improvement of the DAQ live time.

Bibliography

- [1] A.Di Giacomo *Lezioni di Fisica Teorica* edizioni ETS (1992), riferimenti interni
- [2] F.Halzen and A.D.Martin *Quarks & Leptons: an introductory course in modern particle physics* Edition Wiley (1984), riferimenti interni
- [3] W.-M.Yao et al. *Journal of Physics* G33, 1 (2006) <http://pdg.lbl.gov>
- [4] R. R. Crittenden et al., *Phys. Rev.* 121 (1961) 1823
- [5] W. Bertl et al., *Phys. Lett.* B140 (1984) 299.
W. Bertl et al., *Nucl. Phys.* B260 (1985) 1.
- [6] Y. Fukuda et al. (Super-Kamiokande Collaboration), *Phys. Rev. Lett.* 85 (2000) 3999.
- [7] M. Ambrosio et al. (MACRO Collaboration), *Phys. Lett.* B434 (1998) 451.
- [8] W. W. M. Allison et al. (Soudan Collaboration), *Phys. Lett.* B391 (1997) 491.
- [9] Y. Fukuda et al. (Super-Kamiokande Collaboration), *Phys. Rev. Lett.* 86 (2001) 5656.
- [10] Q. R. Ahmad et al. (SNO Collaboration), *Phys. Rev. Lett.* 89 (2002) 011302.
- [11] B. Cleveland et al., *Ap. Jour.* 496 (1998) 505.
- [12] W. Hampel et al. (Gallex Collaboration), *Phys. Lett.* B447 (1999) 127.
- [13] J. N. Abdurashitov et al. (SAGE Collaboration), *Phys. Rev. Lett.* 83 (1999) 4686.
- [14] M. Altmann et al. (GNO Collaboration), *Phys. Lett.* B490 (2000) 16.
- [15] K. S. Hitara et al. (Kamiokande Collaboration), *Phys. Rev. Lett.* 65 (1990) 1297.
- [16] K.Eguchi et al., The KamLAND Collaboration *First Result from KamLAND: Evidence for reactor anti-neutrinos disappearance* *Phys. Rev. Lett.* **90**, 021802,2003

- [17] The K2K Collaboration, E.Aliu et al., *Evidence for muon neutrino oscillation in an accelerator-base experiment* Phys. Rev. Lett. **94**, 081802,2005
- [18] C. Kraus et al., Eur. Phys. J. C40 (2005) 447.
- [19] V. M. Lobashev et al., Phys. Lett. 460 (1999) 227.
- [20] K. A. Assamagan et al., Phys Rev. D53 (1996) 6065.
- [21] R. Barate et al. (ALEPH Collaboration), Eur. Phys. J. C2 (1998) 395.
- [22] F.Bohem and P.Vogel *Physic of massive neutrinos* Cambridge University Press (1992)
- [23] R.N.Mohapatra *Unification and Supersymmetry*, 2nd edition, Springer-Verlag, New York (1992)
- [24] D.I.Kazakov *Beyond the Standard Model*, Caramulo 2000, High-energy physics conference, 125-199
- [25] J.Hisano, T.Moroi, K.Tobe and M.Yamaguchi, Phys. Lett. **B391** (1997) 341 and Erratum, Phys. Lett. **B391** (1997) 357
- [26] H.Georgi, *Particles and Fields*, ed. C.E.Carlson, AIP (1975)
- [27] M. L. Brooks et al. [Mega Collaboration], New limit for the lepton-family-number non-conserving decay $\mu^+ \rightarrow e^+\gamma$, Phys. Rev. Lett. D **83**, 1521-1524 (1999)
- [28] T.Yanagida, *Proceedings of the workshop on Unified Theory and Baryon Number of the Universe*, Tsukuba, Japan, 1979 edited by O.Sawada and A.Sugamoto (KEK, Tsukuba, 1979), p.95
- [29] J.Hisano and D.Nomura, *Solar and atmospheric neutrino oscillations and lepton flavor violation in supersymmetric models with the right-handed neutrinos*, Phys. Rev. D **59**, 116005, (1999)
- [30] E.P.Hincks and B.Pontecorvo *Phys. Rev. Lett.*, Vol.73, 246 (1947)
- [31] Lokonathan. S. and J.Steinberg *Search for Improbable Muon Decays*, Phys. Rev. **98**, 240 (1955)
- [32] G.Feinberg *Phys. Rev. Lett.*, Vol.116, 1482 (1958)

- [33] B.Pontecorvo *ZhEFT*, Vol.39, 1166 (1960)
- [34] Danby, J.M.Gaillard, K.Goulios, L.M.Lederman, N.Mistry, M.Schwartz and J.Steinberger, *Phys. Rev. Lett.* **9**, 36 (1962)
- [35] MEGA Collaboration, "Search for the lepton-family-number nonconserving decay $\mu^+ \rightarrow e^+\gamma$ ", *Phys. Rev. D* **65** (2002) 112002.
- [36] P. Depommier et al., "A New Limit On The $\mu^+ \rightarrow e^+\gamma$ Decay", *Phys. Rev. Lett.* **39**, 1113 (1977)
- [37] A. van der Schaaf et al., "A Search For The Decay $\mu^+ \rightarrow e^+\gamma$ ", *Nucl. Phys. A* **340**, 249 (1980)
- [38] W. W. Kinnison et al., "A Search For $\mu^+ \rightarrow e^+\gamma$ ", *Phys. Rev. D* **25**, 2846 (1982)
- [39] R. D. Bolton et al., "Search For The Decay $\mu^+ \rightarrow e^+\gamma$ ", *Phys. Rev. Lett.* **56**, 2461 (1986)
- [40] Y.Kuno and Y.Okada *Reviews of Modern Physics* Vol. 73, 151 (2001)
- [41] MEG Collaboration, *The MEG experiment: search for the $\mu^+ \rightarrow e^+\gamma$ decay at PSI* (2002), available on site: meg.pi.infn.it, internal references
- [42] H-W. Reist et al., *Development of a low-momentum "''surface''" muon beam for LAMPF* *NIM* 153 (1978) 61
- [43] MEG Collaboration, *Test measurements for the MEG drift chambers* in PSI Annual Report (2003), also at <http://meg.pi.infn.it/docs/index.html>
- [44] K.Watanabe and M.Zelikoff, *Absorption coefficients of water vapor in the vacuum ultraviolet* *J.Opt. Soc. Am.* **43** (1953) 753
- [45] K.Watanabe, E.Inn and M.Zelikoff, *Absorption coefficients of oxygen in the vacuum ultraviolet* *J.Chem. Phys.* **21** (1953) 1026
- [46] A.Baldini et al., MEG internal note TN018, January 2001
- [47] http://wwwasdoc.web.cern.ch/wwwasdoc/zebra_html3/zebramain.html
- [48] *The GEANT physics simulation reference manual*, v.3.21 (1994) CERN Library Long Writeup W5013 <http://wwwasdoc.web.cern.ch/wwwasdoc/geant/>

- [49] <http://root.cern.ch>
- [50] <http://wwwasdoc.web.cern.ch/wwwasdoc/>
- [51] MIDAS home page, <http://midas.psi.ch>
- [52] MYSQL home page, <http://www.mysql.com/>
- [53] Handbook of Chemistry & Physics, The Chemical Rubber Company.
- [54] A. C. Sinnock and B. L. Smith, Phys. Rev. 181 (1969) 1297.
- [55] T. Doke and K. Masuda, Nucl. Instr. Meth., A420 (1999) 62.
- [56] Particle Data Book.
- [57] A. Baldini et al., Nucl. Instr. Meth. A545 (2005) 753.
- [58] L. M. Barkov et al., Nucl. Instr. and Meth. A379 (1996) 482.
- [59] J. L. Subtil et al., Phys. Stat. Sol. B143 (1987) 783.
- [60] J. Jortner et al., J. Chem. Phys. 42 (1965) 4250.
- [61] N. Schwenter, E.E. Koch and J. Jortner, *Electronic Excitations in Condensed Rare Gases*, Springer-Verlag, Berlin 1985.
- [62] Takahashi et al., *Average energy expended per ion pair in liquid xenon*, Phys. Rev. A 12, 1771 (1975)
- [63] T. Doke and K. Masuda, *Present status of liquid rare gas scintillation detectors and their new application to gamma-ray calorimeters*, Nucl. Instr. Meth. A420 (1999) 62
- [64] L. D. Landau and E. M. Lifshitz, *Electrodynamics of continuous media*, Pergamon Press.
- [65] G. M. Seidel, R. E. Lanou and W. Yao, *Rayleigh scattering in rare-gas liquids*, Nucl. Instrum. Meth. A 489 (2002) 189
- [66] A. Braem et al., Nucl. Instr. and Meth. A 320, 228 (1992).
- [67] V. Y. Chepel, M. I. Lopes, R. Ferreira Marques, and A. J. P. L. Policarpo, Nucl. Instr. and Meth. A 349, 500 (1994).

- [68] N. Ishida et al., Nucl. Instr. and Meth. A 384, 380 (1997)
- [69] T. Iwamoto et al., *Development of a large volume zero boil-off liquid xenon storage system for muon rare decay experiment (MEG)*, Cryogenics 49, 254-258 (2009).
- [70] T. Haruyama, *A pulse-tube refrigerator for the PSI MUEGAMMA experiment*, MUEGAMMA (2000) <http://meg.pi.infn.it>, and KEK-PREPRINT-2002-102
- [71] R. Sawada et al., Cryogenic 43 (2003) 449.
- [72] S. Mihara et al., Cryogenics 46, 688 (2006).
- [73] G. Signorelli, *A Sensitive search for lepton-flavour violation: the MEG experiment and the new LXe calorimetry*, unpublished, available at <http://meg.web.psi.ch/docs/theses/>
- [74] A. Baldini et al., *A cryogenic facility for testing the PMTs of the MEG liquid xenon calorimeter* NIM A, p. 294 (2006)
- [75] Hamamatsu Photonics K.K., Photomultiplier tube, principle to application, 1994.
- [76] A. Baldini et al., *A Radioactive point-source lattice for calibrating and monitoring the LXe calorimeter of MEG experiment*, NIM A, 565 (2006), 589-598
- [77] S. Bazzarri, G. Cicoli, P. De Felice, G. Rossi and F. Sedda, *Leakage Tests for Am-241 Solid Sources Used for Liquid Xenon Detector Monitoring*, Nucl. Instr. Meth. A560 (2006) 640.
- [78] Thermo Scientific, *D211 Neutron Generator Operation Manual*.
- [79] F. Tenchini *Calibrazioni e Monitoraggio dell'Esperimento MEG* unpublished, available at <http://meg.web.psi.ch/docs/theses/>
- [80] A. Papa *Search for the lepton flavour violation in $\mu^+ \rightarrow e^+ + \gamma$. The calibration methods for the MEG experiment* unpublished, available at <http://meg.web.psi.ch/docs/theses/>
- [81] NACRE - European Compilation of Reactions Rates for Astrophysics;
<http://pntpm.ulb.ac.be/nacre.htm>
- [82] Panofsky et al., *The Gamma Ray Spectrum Resulting from Capture of Negative π -Mesons in Hydrogen and Deuterium*, Phys. Rev. 81, 565-574 (1951)

- [83] A.Papa, *Misura del fotone di decadimento nell'esperimento $\mu \rightarrow e + \gamma$ mediante la nuova calorimetria a Xenon liquido* unpublished, available at <http://meg.web.psi.ch/docs/theses/>
- [84] A.Baldini et al., Meg internal note TN030, January 2006
- [85] G.Signorelli, *A Sensitive search for lepton-flavour violation: the MEG experiment and the new LXe calorimetry* PhD Thesis, unpublished, available at <http://meg.web.psi.ch/docs/theses/>
- [86] Y.Uchiyama, *Analysis of the First MEG Physics Data to Search for the Decay $\mu \rightarrow e + \gamma$* PhD Thesis, unpublished, available at <http://meg.web.psi.ch/docs/theses/>
- [87] G.Gallucci, *Studio della prestazioni del calorimetro elettromagnetico dell'esperimento MEG per la ricerca del decadimento $\mu \rightarrow e + \gamma$* unpublished, available at <http://meg.web.psi.ch/docs/theses/>
- [88] Baldini et al, *Transparency of a 100 liter liquid xenon scintillation calorimeter prototype and measurement of its energy resolution for 55 MeV photons* IEEE International Conference on Dielectric Liquids, ICDL2005 Coimbra, June 26-July 1 2005 337 - 340
- [89] Hajime Nishiguchi, *An Innovative Positron Spectrometer to Search for the Lepton Flavour Violating Muon Decay with a Sensitivity of 10^{-13}* PhD Thesis, unpublished, available at <http://meg.web.psi.ch/docs/theses/>
- [90] *A real-time glance at the Lepton Flavor Violating decay $\mu \rightarrow e\gamma$ in the MEG experiment* PhD Thesis, unpublished, available at <http://meg.web.psi.ch/docs/theses/>
- [91] Y. Kuno and Y. Okada, Rev. Mod. Phys. 73 (2001), p. 151.
- [92] G.J. Feldman and R.D. Cousins, Phys. Rev. D 57 (1998), p. 3873